Atomic vapours filled hollow core photonic crystal fibre for magneto-optical spectroscopy

Bradley, Thomas

Award date:
2014

Awarding institution:
University of Bath

Atomic vapours filled hollow core photonic crystal fibre for magneto-optical spectroscopy

Thomas David Bradley

A thesis submitted for the degree of Doctor of Philosophy

University of Bath
Department of Physics

September 2013

Abstract

This thesis describes developments in atomic vapour loading in hollow core photonic crystal fibre (HC-PCF) for fabrication of atomic vapour loaded photonic microcells (PMC). These developments have been targeted at addressing some of the issues associated with loading atomic vapours in confined waveguiding geometries such as increased dephasing and physio-chemical wall absorptions.

Atomic vapour loaded HC-PCF and PMC's have applications in laser metrology, coherent optics and magneto optical spectroscopy. State of the art HC-PCF have been fabricated for loading with atomic vapour including both photonic bandgap (PBG) guiding and inhibited coupling (IC) hypocycloidal core shape Kagome HC-PCF. Record loss of 70 dB/km has been achieved in IC hypocycloid core shape Kagome HC-PCF in the spectral region centred at 800 nm. This fibre retains excellent single mode propagation combined with large core and increased optical bandwidth in comparison with specialist PBG HC-PCF optimised for operation around 800 nm.

Aluminosilicate sol-gel coatings have been developed and successfully applied to the inner core wall of HC-PCF's to reduce the atomic vapour surface interaction. Confining atomic vapours in micron scaled HC-PCF results in increased dephasing rates because of the frequent atom wall collisions. Anti relaxation coating materials have been applied to the inner core wall and the longitudinal relaxation time has been measured in coated and uncoated fibres utilising a magneto optical technique. Additionally sub Doppler transparencies are investigated in anti relaxation coated and uncoated HC-PCF.

Preface

Atomic vapours have diverse applications from investigations of novel physical phenomena, laser frequency stabilisation, laser cooling, magneto optical spectroscopy and frequency standards. Miniaturisation of the host structure for atomic vapours would be beneficial for industry and science around the world by bringing atomic precision to these environments. To date several confined dielectric structures have been realised based upon a range of fabrication techniques. Hollow core waveguiding geometries offer significant advantages for confined light matter interactions as such have been investigated.

Chapter 1 introduces the background physics behind optical coherences because of their extensive use within this thesis. A discussion of existing confined atomic vapour dielectric photonic geometries is presented with a discussion of the advantages and disadvantages of each platform are discussed. Finally the advantages and disadvantages of HC-PCF for confined atomic vapour interactions are discussed.

In chapter 2 the physics underlining the guidance mechanism of both photonic bandgap (PBG) guiding and inhibited coupling (IC) Kagome hollow core photonic crystal fibre (HC-PCF) are introduced. The photonic tight binding model which describes the formation of PBG is introduced and its application to double photonic bandgap (DPBG) is discussed.

Chapter 3 presents development of state of the art HC-PCF. This includes the development of low loss PBG guiding HC-PCF for operation around 780 nm with optical attenuation which is approximately halve that of commercially available PBG HC-PCF. Double photonic bandgap HC-PCF is presented where for the first time the guidance bands have been shifted to shorter wavelengths.

Chapter 4 introduces enhanced inhibited coupling guidance in Hypocycloid core shape Kagome HC-PCF. Hypocycloid core shape IC Kagome HC-PCF is developed with state of the art optical attenuation at 780 nm, excellent optical mode quality, large core diameter and increased optical bandwidth. Additionally numerical simulations and experimental investigation on developments of the hypocycloidal core shape Kagome HC-PCF are presented.

Chapter 5 introduces the dynamics of atomic vapour loading in confined geometries such as HC-PCF under the regimes of molecular free flow. The post processing techniques which are a necessity for atomic vapour applications are detailed, including the three stage coating process for applications of antirelaxation and aluminosilicate sol-gel coatings. Finally post processing of the HC-PCF including tapering and novel “sleeve” splicing are presented for the development of atomic vapour photonic microcells (PMC).

Chapter 6 presents experimental evidence whereby the rate of reaction between atomic vapour confined in HC-PCF is reduced by application of a novel

aluminosilicate sol-gel coating to the inner core wall of HC-PCF. Elongated vapour lifetime up to 500 hours are observed in sol-gel coated HC-PCF. Additionally the vapour is preserved even in the absence of an ambient vapour surrounding the sol-gel coated HC-PCF.

In chapter 7 the increased dephasing rates associated with confining atomic vapours in micron scaled HC-PCF is presented. A magneto optical rotation technique is presented which allows the dephasing from atom wall collisions to be probed independently from the transit time broadening. Additionally the impact of antirelaxation coatings on the coherence of atoms in investigated by studying electromagnetically induced transparency features in coated and uncoated HC-PCF.

Chapter 8 presents novel sub Doppler transparency features which are generated through only a single beam which both pumps and probe the atomic ensemble loaded in the HC-PCF. The behaviour of sub Doppler transparencies are characterised against applied magnetic field, pump beam power and polarisation. Finally reflection spectrum are obtained to characterise the behaviour of the sub Doppler transparencies and to gain physical insight behind the generation mechanism.

Acknowledgements

To start I would like to thank Fetah Benabid my supervisor for giving me the opportunity to study for my PhD. I would also like to thank the past and present members of the Gas Phase Photonics Group and the Gas Phase Photonics and Microwave Materials Group. Specific mention should go Meshaal Alharbi whom I have worked with closely over the last few years and has suffered my many annoying habits over the last two years in Limoges. I would like to thank Natalie Wheeler for having patience with a first year PhD student and teaching me the basics about my experiment. I would also like to acknowledge Brian Mangan for making me into the fibre fabricator I am today, I won't claim it was fun but thank you Brian. Additionally I would like to thank Yingying Wang, Francois Couny, Benoit Beaudou, Benoit Debord, Fred Gerome, Florian Vial, Damien Arreister and the rest of the Limoges lab crew.

I would also like to thank the wider Centre for Photonics and Photonic Materials Group and the Xlim research institute for being great places to work.

I would like to thank the Bath technicians Steve Renshaw, Paul Reddish, Harry Bone and Wendy Lambson for their help and expertise. In Limoges I would like to thanks Seb Rougier for his help with fibre drawing.

Finally but my no means least I would like to thanks my family and friends for your support during the last 4 years.

Table of Contents

Journal Publications

B Debord, M Alharbi, T D Bradley, C Fourcade-Dutin, YY Wang, L Vincetti, F Gerome & F Benabid, "Hypocycloid shaped hollow core photonic crystal fiber Part I: Cusps curvature effect on confinement loss", Submitted Optics Express (2013)

YY Wang, M Alharbi, T D Bradley, C Fourcade-Dutin, B Debord, B Beaudou, F Gerome & F Benabid, "Hollow-core photonic crystal fibre for high power laser beam delivery", High Power Laser Science & Engineering, 1 (1), 2013

T D Bradley, YY Wang, M Alharbi, B Debord, C Fourcade-Dutin, B Beaudou, F Gerome & F Benabid, "Optical Properties of Low Loss (70dB/km) Hypocycloid-Core Kagome Hollow Core Photonic Crystal Fiber for Rb and Cs Based Optical Applications", JLWT, 31 (16), 2013

C Wang, N V Wheeler, C Fourcade-Dutin, M Grogan, T D Bradley, B Washburn, F Benabid & K Corwin, "Acetylene frequency references in gas-filled hollow optical fiber and photonic microcells", Applied Optics, 53 (22), 2013

YY Wang, X Peng, M Alharbi, C Fourcade-Dutin, T D Bradley, F Gerome, M Mielke, T Booth & F Benabid, "Design and fabrication of hollow-core photonic crystal fibers for high-power ultrashort pulse transportation and pulse compression", Optics Letters, 37 (15), 2012

A V Vasudevan Nampoothiri, A M Jones, C Fourcade-Dutin,C Mao, N Dadashzadeh, B Baumgart,YY Wang, M Alharbi, T Bradley, N Campbell, F Benabid, B R Washburn, K L Corwin & W Rudolph, "Hollow-core Optical Fiber Gas Lasers (HOFGLAS): a review [Invited]", Optical Materials Express, 2 (7), 2012

B Beaudou, F Gerome, YY Wang, M Alharbi, T D Bradley, G Humbert, JL Auguste, JM Blondy & F Benabid, "Millijoule laser pulse delivery for spark ignition through kagome hollow-core fiber", Optics Letters, 37 (9), 2012

N V Wheeler, M D W Grogan, T D Bradley, F Couny, T A Birks & F Benabid, "Multipass Hollow Core-PCF Microcell Using a Tapered Micromirror", JLWT, 29 (9), 2011

Conference Publications

T D Bradley, JJ McFerran, J Jouin, P Thomas, E Illinova & F Benabid, "Atomic polarization relaxation time measurement of Rb filled hypocycloidal core shape Kagome HC-PCF", CLEO 2013, CM3I.8

T D Bradley, JJ McFerran, J Jouin, P Thomas & F Benabid "Long rubidium vapor lifetime in aluminosilicate sol-gel coated hypocycloidal core shape Kagome HC-PCF", CLEO 2013, CM3I.2

B Debord, M Alharbi, T Bradley, C Fourcade-Dutin, D Ghosh, L Vincetti, F Gerome & F Benabid, "Cups curvature effect on confinement loss in hypocycloid-core Kagome HC-PCF", CLEO 2013, CTu2K.7

M Alharbi, T Bradley, B Debord, C Fourcade-Dutin, D Ghosh, L Vincetti, F Gerome & F Benabid, "Cladding effect on confinement and bend losses in hypocycloid-core Kagome HC-PCF", CLEO 2013, CTu2K.7

C Wang, T D Bradley, YY Wang, K Corwin, F Gerome & F Benabid, "Angle splice of large-core Kagome hollow-core photonic crystal fiber for gas-filled microcells", CLEO 2013, CM3I.1

T D Bradley, JJ McFerran, J Jouin, P Thomas & F Benabid, "Progress towards atomic vapor photonic microcells: Coherence and polarization relaxation measurements in coated and uncoated HC-PCF", Proc. SPIE 8636, Advances in Slow and Fast Light VI, Photonics West 2013

T D Bradley, M Alharbi, YY Wang, C Fourcade-Dutin & F Benabid, "Optical properties of low loss (70dB/km) Kagome hollow core photonic crystal fiber for Rb and Cs based optical applications", CLEO 2012, CM3N.1

B Beaudou, F Gerome, YY Wang, M Alharbi, T Bradley, G Humbert, JL Auguste, JM Blondy & F Benabid, "Milli-Joule laser pulse delivery for spark ignition through kagome fiber", CLEO 2012, CM3N.4

T D Bradley, YY Wang, M Alharbi, B J Mangan, C Fourcade-Dutin, N V Wheeler & F Benabid, "Progress in hollow core photonic crystal fiber for atomic vapour based coherent optics", Proc. SPIE 8273, Advances in Slow and Fast Light V, 82730 Photonics West 2012

YY Wang, X Peng, M Alharbi, C Fourcade-Dutin, T D Bradley, M Mielke, T Booth & F Benabid, "Design and fabrication of hollow-core photonic crystal fibers for high power fast laser beam transportation and pulse compression", Proc. of SPIE Vol. 8269 , Photonic and Phononic Properties of Engineered Nanostructures II, Photonics West 2012

N V Wheeler, M D W Grogan, T D Bradley, F Couny, T A Birks & F Benabid, "Ultra-High Reflectivity Hollow Core PCF Microcell using a Tapered Micro-Mirror", CLEO 2010, CThB3

Chapter 1

Coherent optical phenomena within gas confined in dielectric photonic structures

In this chapter, I introduce prior work on coherent optical phenomena in molecular or atomic gases confined in dielectric photonic structures. In particular, I discuss the merits and drawbacks of each of the schemes adopted to confine atomic gases and how they contrast with the scheme adopted in the present thesis.

The physical mechanisms of coherent optical phenomena are briefly reviewed due to their extensive use within this thesis and prior work dealing with atomic and molecular gases confined in dielectric photonic structures.

1.1 Introduction

Atomic and molecular transitions have a diverse range of applications in physical research firstly because of the fundamental nature of these transitions and secondly because such transitions are easily probed with narrow linewidth lasers. Applications include molecular and atomic frequency standards, and quantum sensing applications such as magnetometers to mention a few. Atomic transitions are the system of choice for atomic microwave (1–3) and optical clocks (4,5), laser cooling (6–8), laser stabilisation (9,10), quantum sensors and study of novel quantum phenomena (11,12). While demonstrating elegant results these systems are extremely cumbersome. It would be beneficial from both a technological and scientific stand point to be able to deliver these outstanding laboratory performances in

stable compact devices for use in industry and the world outside specialised laboratories. To realise such an aim the size of the host structure containing atomic and molecular gases needs to be minimised. While this sounds straight forward, reducing the dimensions of the gas host structure reduces the signal to noise ratio (SNR) of any probed transitions by reducing the interaction length with the medium. Secondly smaller gas host systems result in increased level of interactions with the walls of the container, and subsequently undesired broadening and shifting atomic and molecular transitions spectral lines, or physio-chemical reaction with the wall surface.

Atomic and molecular transitions have an intrinsic fundamental linewidth set by the Heisenberg uncertainty principle. Typically the intrinsic linewidth is Doppler broadened to hundreds of megahertz by the Maxwell-Boltzmann velocity distribution of the atoms or molecules. Experimental techniques for generating sub Doppler transparency features in atomic and molecular ensembles exist and are widely employed in current applications such as atomic clocks. Examples of these techniques are saturable absorption spectroscopy (SAS) (13), electromagnetically induced transparency (EIT) (14,15), coherent population trapping (CPT) (16) and Ramsey interference (17,18). Such techniques can be used to generate extremely narrow sub Doppler transparency features for laser frequency stabilisation, atomic clocks and quantum sensors.

A brief overview of the basic physics underlining these techniques will be presented in the chapter because of their relevance to the work presented later. In the following part of this chapter a review of the work to date on reducing the physical dimensions of the gas host container will be presented. Different methods have been utilised for reducing the physical dimensions of the gas host, varying from micro-electronic-mechanical systems (MEMS) technology to dielectric waveguide technologies. The use of dielectric waveguiding geometries such as hollow core photonic crystal fibres (HC-PCF) for hosting gas phase atomic and/or molecular media offers several benefits. The benefits offered by HC-PCF include very long interaction length which is possible due to low loss propagation in the waveguide, tight transverse mode confinement and easy integration with existing fibre optic systems. These features mitigate some of the problems involved with reducing the transverse dimensions of the gas host container such as increased atom wall collisions. Miniaturisation of the gas host has become a pressing need to deliver the outstanding performance of atomic vapours to industry and the world outside the laboratory. However

this miniaturisation would make sense only if the dephasing of the excited state atomic coherences is adequately addressed. In the two upcoming sections the physics and the different generation mechanisms of atomic coherence are reviewed. Additionally the routes taken so far in developing miniaturised devices are presented.

1.2 Coherent Optical Phenomena

A state of a quantum mechanical system (e.g. an atom) can exist in either a set of well defined eigenstates (also known as bare eigenstates) or in a superposition of these eigenstates. In practice this superposition state is often generated by coupling two or more bare states by one or more laser fields. We say then that coherence exists between the individual bare eigenstates. In other words, by coherence, we mean the phase relationship between the field-induced coupled-states. The simplest possible system in which coherence can be observed is an atom consisting of two energy levels E_1 and E_2 (figure 1-1a) where transitions are dipole allowed which in turn are coupled by a laser field frequency, ω (19). In such a two level system the population can be coherently driven to completely deplete the ground state. The steady state of such an excitation is an oscillation of the population between the ground and excited state, and at a rate that depends on the oscillator strength of the transition between the two energy levels (e.g. dipole moment), the intensity of the laser field and its detuning from the atomic resonance. This process is known as Rabi oscillations and is portrayed in the red curve of figure (1-1) b) (20,21), and the oscillation frequency, called the Rabi frequency is given by

$$\Omega_R = \sqrt{\Omega_0^2 + \Delta^2}\ , \tag{1-1}$$

where Δ is the laser field detuning from atomic resonance and

$$\Omega_0 = \frac{\boldsymbol{\mu} \cdot \boldsymbol{E_0}}{\hbar}, \tag{1-2}$$

where E_0 is the electric field, μ is the electric dipole moment of the transition in question and $\hbar$ is the reduced Planck constant. The Rabi frequency Ω_0 describes the on resonance light matter coupling because it takes into account the oscillator strength and the light field hence fully characterising the light matter interaction.

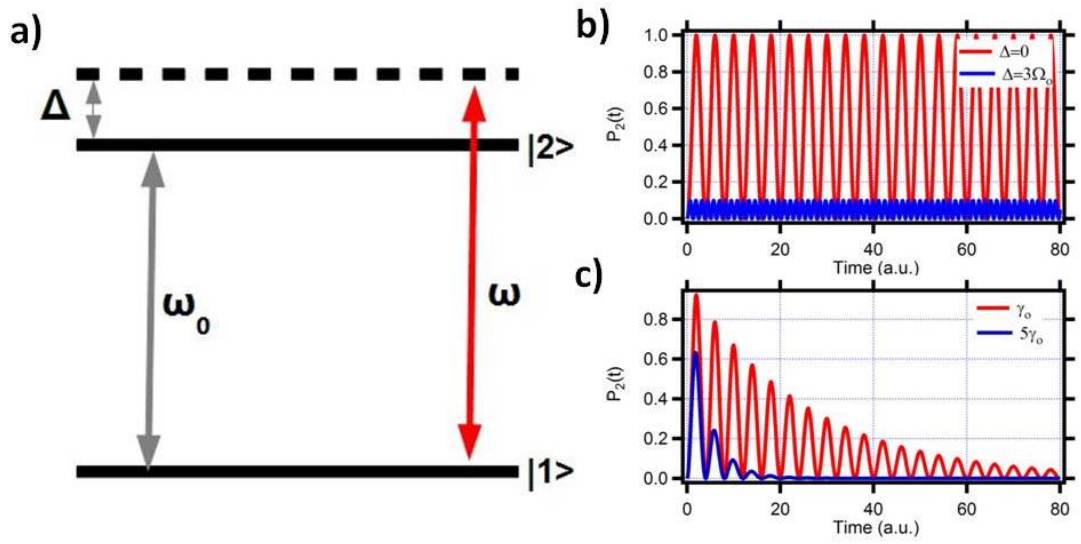

Figure (1-1) (a) Two level atomic system resonant frequency ω_0 irradiated by laser field frequency ω. (b) Rabi oscillations of the excited state of a two level atom for different detuning form resonance of the irradiating laser field, $\Delta=0$ (red line), $\Delta=3\Omega_0$ (blue line), c) Rabi oscillations of the excited state of a two level atom for including dephasing. Dephasing rate = γ_o (red line) and $5\gamma_o$ (blue line).

Rabi oscillations for the excited state of the two level system are shown in figure (1-1) b) for two different detuning from resonance, $\Delta = 0, 3\Omega_0$ (red and blue curves respectively). In reality, an infinitely long oscillation (coherence) is unrealistic. Even for a closed system the population in higher energy level has limited life time and decays at a rate given by spontaneous emission γ_{sp}. Furthermore, such a decay rate is exacerbated by several other physical mechanisms, which further attenuate strongly such an oscillation (coherence) via dephasing mechanisms. These dephasing mechanisms could be of different origin from the fundamental limited lifetime of any excited state (spontaneous emission) to other such as collisional dephasing. If we limit these mechanism to those of collisional origin, then the coherence decay takes the following form given by $\frac{\gamma_{sp}}{2} + \gamma_{coll}$. Here, γ_{coll} is the collision induced coherence decay. Figure (1-1) c) shows Rabi oscillations with different dephasing rates (γ_o-red curve and $5\gamma_o$-blue curve) resulting in damping of the oscillation as the relative phase relation between the levels is disrupted. Given that often the dephasing rate is always greater than the spontaneous emission limit engineering coherence is extremely challenging and any resulting coherence is fragile and sensitive to perturbations. The absorption line shape is typically broadened by several processes, including Doppler, collisional, power and

transit time. These mechanisms can be broken down into two categories, homogeneous (22,23), acting on all the atoms in the same manner and inhomogeneous (22–24), a perturbation that depends on the energy state of each atom (e.g. atom velocity). Power and collisional broadening are examples of homogeneous broadening while transit time and Doppler broadening are examples of inhomogeneous broadening because of the dependence on the individual atomic velocities.

Saturable absorption spectroscopy (SAS) (25), coherent population trapping (CPT) (26), electromagnetically induced transparency (EIT) (14,15,27) and Ramsey interference (17,18) are all examples of techniques to generate narrow sub Doppler linewidth features. The physical mechanism generating the sub Doppler feature varies from SAS which relies upon saturating the atomic population of a particular velocity class to destructive interference between the coherent state excitation pathways in EIT. With the exception of SAS, the other techniques are coherent techniques requiring precise engineering of the coherent atomic state. In general atomic coherences are engineered in 3 level systems (Fig (1-2)). In such a three level system it is possible to observe interference because of the fixed phase relationship between the different excitation pathways.

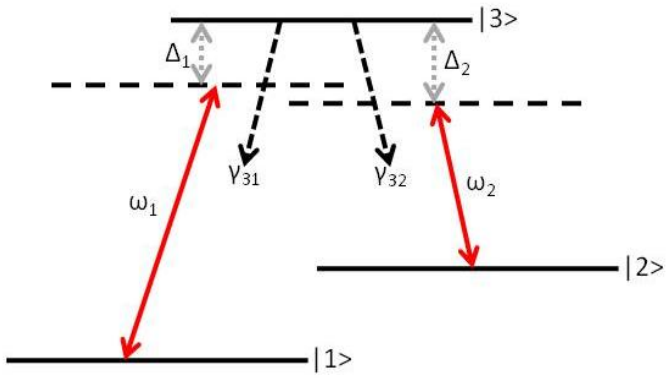

Figure (1-2) Schematic of three level system. Where the exact detuning from resonance of each laser field is $\Delta_1=\omega_{12}-\omega_p$ and $\Delta_2=\omega_{23}-\omega_c$ respectively and $\gamma_{31/32}$ are the decay rates from the excited state to the two ground states.

Two and three level systems can be used in a range of applications from Ramsey interference, EIT and saturable absorption for laser metrology, to laser cooling and fundamental investigation of EIT phenomena and slow/superluminal light (28,29). One of the most important feature of an atomic transitions is its capability to act as a frequency

standard, which in turn can be characterised by the fractional frequency stability (30,31) of the emitted or exciting electromagnetic radiation,

$$\frac{\Delta f}{f} \propto \frac{1}{Q}\ , \tag{1-3}$$

where $Q = \omega_0/\Delta\omega$, is the quality of factor of the resonator, here ω_0 is the frequency of the atomic transition and $\Delta\omega$ is the linewidth of the transition. The Q factor is a measure of the oscillation strength of the atomic coherence for sub Doppler transparencies with respect to its resonance frequency. Extremely high Q factors have now been achieved by either cooling the atoms (32) ($Q \sim 9.8 \times 10^9$) or by using metastable optical transitions ($Q \sim 1.6 \times 10^{13}$) (4). These ground breaking results include the first observation of EIT (15), slow light (29) and atomic fountain clocks (1). Compact host structures for atomic and molecular gas phase media have a range of potential applications, such as hand held GPS devices. The current trend in research toward fabricating compact integrated platforms for gas laser interactions is being driven by the desire to deliver the same, or at least comparable, outstanding performance observed in laboratory setups in compact portable devices. Compact hosts for atomic vapours are not intended to replace primary frequency standards because the high Q factor necessary for these applications will not be achievable in such confined geometries due to the dephasing problems. However if reasonable Q factors with high signal to noise ratio (SNR) can be achieved then there are many real world devices such as handheld GPS which could benefit from such miniaturised devices.

1.3 Compact host for coherent optical phenomena

The challenges in miniaturising the atomic host structure for coherent related optical phenomena are two-fold. Firstly can the dephasing (mainly due atom wall collisions) be sufficiently minimised. Such effects are detrimental to the performance of a compact host for coherent optical phenomena in gas phase media. Hence there is a desire to minimise the impact of these effects while maintaining relatively compact systems. In bulk atomic vapour cells both over pressurisation with buffer gases (e.g. Ne, He) (33) and antirelaxation wall coatings (34) have been successfully demonstrated to minimise dephasing due to atom-wall

collisions. The deposition of coating materials in HC-PCF will be discussed in chapter 5 and their performance characterised in chapter 7.

Secondly such a miniaturisation is a real challenge technologically as it entails devising a photonic structure that could harbour light and the atomic gas together in a robust and efficient manner. Among the challenges we count the physio-chemical reactions between the atomic vapour and the host container and the loading process of atomic vapours in geometries whose dimensions are orders of magnitude smaller than the atomic mean free path. For compact atomic vapour devices to become viable the loading and maintaining of highly reactive atomic vapours in confined environments free from bulk vacuum equipment needs to be addressed. Compact atomic vapour devices based on a range of technologies have recently been developed by several research groups. Fabricating confined geometries for gas media laser interactions have advanced in several directions, two of which are micro-electrical-mechanical systems (MEMS) manufacture and dielectric photonic waveguide geometries. Dielectric photonic waveguide geometries consist of hollow core photonic crystal fibres (HC-PCF), anti resonant reflecting optical waveguides (ARROW's) and tapered optical fibres. A review of these different platforms is presented below and the advantages and disadvantages of the various platforms are outlined.

1.3.1 Microchip Atomic Clock

A micro fabricated atomic clock was reported by Knappe *et al*. in 2004 (35). Micro-electro-mechanical systems (MEMS) techniques which are compatible with mass production were utilised to fabricate this chip scale device. The final fabricated device has a volume of 9.5 mm^3. Caesium atomic vapour resides at the core of this package where a CPT feature with linewidth of 7.1 kHz (35), is generated by current modulating a vertical cavity surface emitting laser (VCSEL) at 4.6 GHz (sidebands are generated separated by 9.192 GHz which are resonant with the ground state hyperfine splitting of Cs), providing a frequency reference. Measuring the frequency stability of such a narrow CPT feature gives an estimated stability of 2.5×10^{-10} at 1 s integration time, while requiring less than 75 mW of power to operate.

This device fulfils many of the requirements for a compact frequency standard such as reasonable short term stability, compact size and low power consumption. However the device requires external temperature and current control which adds to the size. Also the interaction length with the Cs vapour is extremely short because of the compact size as such the contrast of the frequency reference is extremely small, 0.91% of the total absorption line strength. Finally, while the design is fully integrated it relies upon traditional free space propagation scaled down to the device size opposed to the following devices which are all waveguiding based designs, hence do not suffer from misalignment of optics.

1.3.2 Tapered Single Mode Fibre Evanescent Field Interactions with Rubidium Vapour

A tapered optical nanofibre (TNF) surrounded with hot rubidium vapour provides evanescent light field atomic vapour interactions at low optical powers (36). Due to the nature of the evanescent field interaction, this system provides an extremely small optical mode area (~ 0.18 μm^2) interacting with the Rubidium (Rb) vapour with saturation power of 4 nW. The unique properties of the TNF hot Rubidium vapour system are used to demonstrate nonlinear absorption and electromagnetically induced transparency.

This system does not fulfil the requirements of a compact host for light matter interactions because while the optical mode area is highly confined, the Rb vapour is confined in a bulk apparatus connected to a vapour source and vacuum equipment. Low power level optical interactions have been demonstrated in the TNF hot Rb vapour system with EIT features being observed at nW power levels. This is possible due to the highly confined nature of the optical mode interacting with the Rb vapour. However the confined nature of the optical field which provides such benefits in terms of optical saturation power severely restricts the narrowest observable linewidth of sub Doppler features. The linewidth is significantly time of flight broadened (37) due to the highly confined optical mode area (~ 0.18 μm^2) compared to what can be observed in bulk reference cells and even compared to other confined dielectric structures such as HC-PCF (~ 30-100 μm^2) and ARROW (~ 8.8 μm^2) waveguides. Hence such a system is unsuitable for compact frequency reference as the linewidths of such features determine the long term stability of such a frequency standard.

Additional studies have been made utilising the TNF hot Rb vapour system for two photon absorption studies and control of nonlinear transmission through TNF (38,39).

1.3.3 Rubidium filled Hollow Core Anti Resonant Reflecting Optical Waveguide (ARROW)

On chip integrated solid and hollow core anti resonant reflecting optical waveguides (ARROWs) (40) loaded with Rb vapour were the first demonstration of an integrated dielectric waveguiding platform for light atomic vapour interactions. The fabricated Rb vapour cells have a small physical volume, demonstrating a 10^7 reduction when compared with macroscopic vapour cells. These ARROW Rb vapour cells harness the micron scale mode area of the waveguide to achieve extreme optical intensities. Characterisation of these ARROW vapour cells was carried out by measuring in-situ optical depth (OD) > 2 and demonstrating SAS with a full width at half maximum (FWHM) ~ 34 ± 2 MHz.

In follow up work, the same research group presented integrated hollow core ARROWs with a monolayer octadecyldimethylmethoxysilane (ODMS) coating to reduce decoherence from atom wall collisions (41). An EIT feature is generated in the atomic vapour confined in the hollow ARROW vapour cell using a pump beam of 18.2 mW and probe beam of 3.6 mW. A transparency feature of FWHM ~ 50 MHz and height of 44% was demonstrated. Analysis of the observed dephasing rates are substantially less than expected when considering atom wall collisions arising from the shortest transverse dimensions of the hollow core ARROW, thus demonstrating the effectiveness of ODMS coating. Transit time broadening is estimated at ~ 52 MHz based on the analysis in ref (40), which places a lower limit on the minimum achievable sub Doppler linewidth.

This work demonstrates for the first time a fully integrated compact Rb vapour waveguiding cell with an attached Rb vapour source and no connection to bulk vacuum equipment. The Rb ARROW vapour cells are characterised in terms of the Rb vapour contrast in comparison to a bulk reference cell in terms of absorption line contrast and atomic density. While this device is completely integrated and compatible with complementary metal oxide semiconductor (CMOS) technology, it still has disadvantages in terms of limited interaction

length and no characterisation of the Rb loss to the hollow waveguide walls is made. Light is coupled into the integrated ARROW vapour cell using tapered optical fibres. Finally no analysis of the reflection at the interface between the solid and hollow ARROWs is presented.

1.3.4 Rubidium filled Photonic Bandgap Hollow Core Photonic Crystal Fibre

The first report of Rb vapour confined within the hollow core of a photonic bandgap (PBG) fibre was in 2006 by Ghosh *et al.* (42). In this work several technical feats are reported for the first time including the deposition of organosilane compounds on the inner core wall and the use of light induced atomic desorption (LIAD) to generate on demand Rb vapour in the hollow core. The combination of these developments allows for an optical depth > 2000 to be achieved in the fibre hollow core. As a final proof of concept an EIT feature with linewidth of ~ 60 MHz is generated at ultra-low pump power of 10 nW and probe power of 100 pW.

This work demonstrates the inherent advantages of confining atomic vapours within hollow core waveguiding geometries such as strong low light level atomic vapour interactions, this system is however not self contained requiring connection to a sophisticated vacuum system to operate successfully. Secondly the atomic vapour loading is extremely time consuming. Following on from this pioneering work demonstrating loading of Rb vapour into hollow core PBG fibres, a large body of work using hollow core PBG fibres has been demonstrated. Examples of such work includes spectroscopy of Rb atoms loaded in hollow core PBG fibres characterising the Stark and power shifts of Rb atoms confined within the hollow core (43). Other work has involved loading cold trapped atoms either from magneto optical traps or Bose-Einstein condensates into the core of PBG fibres(44,45). Additionally the optical guidance of Rb atoms through a hollow core PBG fibre (46,47) has been demonstrated for potential applications in matter wave interferometry.

1.3.5 Rubidium filled Kagome Hollow Core Photonic Crystal Fibre

Rubidium loaded Kagome lattice HC-PCF coated with polydimethylsiloxane (PDMS) was reported shortly after the first reported demonstrations of Rb loaded photonic bandgap (PBG) fibre (48). Both optical pumping and EIT were demonstrated in the Rb vapour confined to the hollow core with a linewidth of 6 MHz, which is below that of an uncoated fibre. Analysis of the broadening mechanisms of the EIT linewidth indicates that optical power broadening is dominate.

This work shows an order of magnitude improvement of the EIT linewidth over that reported by Ghosh *et al.*(42) and analysis of the contributions to the linewidth broadening demonstrates the benefits of a PDMS coating. However this device is still connected to a vacuum system to maintain the ambient pressure at the open fibre ends at the 10^{-7} mbar level. In addition the loading time of such a fibre is still long even though the core diameter is larger than that reported by Ghosh *et al* (42).

1.3.6 Comparison of atomic vapour confined in dielectric host structures

The key parameters of each system discussed above are summarised in Table (1-1) for straight forward comparison. It can be seen that each system has advantages and disadvantages. The first consideration on the performance of the different platforms is the operating power required to observe sub Doppler transparencies. PBG HC-PCF and TNF both operate at nW power levels, followed by Kagome HC-PCF and MEMS based device operating at μW levels and finally ARROW's operating in the mW regime. The ability to operate at such low power levels is provided by the extremely confined nature of the optical mode in these devices. The MEMS based device is a non waveguiding structure hence it is inappropriate to compare the mode area with those of the waveguiding device. In the waveguiding structures the largest mode area is 95 μm^2 in the Kagome HC-PCF and the smallest mode area is 0.18 μm^2 in the TNF. The mode area and the operating power are intrinsically linked because small mode area allows for high optical intensity even at very low optical powers. One could speculate that the drastic increase in laser power required for observation of EIT in ARROW's is due to the inefficient coupling of light in the waveguides

and potentially high waveguides losses (49). However for atomic vapour applications small mode area have two drawbacks, firstly the atomic vapour loading in extremely small mode area devices is tedious and secondly extreme transit time broadening will be observed. The interaction length in the device will contribute to the SNR, in practice long interaction lengths will give higher SNR. Hence low propagation losses are desirable. PBG and Kagome HC-PCF offer the longest interaction length to date by an order of magnitude.

Table (1-1) Comparison of performance parameters of the different dielectric platforms

Platform	Operating Power	Integrated	Mode Area (μm)	Interaction Length (mm)	Linewidth (MHz)
MEMs	μW	Y	4.9×10^{4}	1	7.1×10^{-3}
ARROW	mW	Y	8.8	50	~50
PBG HC-PCF	nW	N	28	250	60
Kagome HC-PCF	μW	N	95	300	6
Tapered Fibre	nW	N	0.18	3	110

The minimum achievable linewidth for sub Doppler transparency features is linked to the mode area. Hence highly confined geometries such as the TNF have large linewidths on the order of 100 MHz. One final consideration is whether the system is integrated, of the devices reported to date only two are completely self contained. However those based on HC-PCF have potential integration with existing fibre optic networks. It is apparent that each system has potential but the advantages offered by HC-PCF especially Kagome HC-PCF seem numerous, such as small mode area combined with long interaction length and possible integration with existing fibre optic networks. The current drawback for systems wishing to utilise HC-PCF's appears to be that to date these platforms require being connected to a bulky vacuum system and as such are not compact. This problem could easily be solved by splicing the atomic vapour filled HC-PCF to standard SMF creating a photonic microcell (PMC) (50,51).

1.4 Coherent Optics in Gas filled HC-PCF

1.4.1 Advantages and Disadvantages of Gas filled HC-PCF

HC-PCF offers tight transverse optical mode confinement with a gaseous medium of choice on the micron scale. In addition extremely long interaction lengths are achievable in comparison to free space propagation due to the low propagation losses. These two attributes can be combined to define a figure of merit (f_{om}) for gas laser interactions in HC-PCF (52,53),

$$f_{om} = \frac{L_{\text{int}}\lambda}{A_{\text{int}}}, \tag{1-4}$$

where L_{int} is the length of uniform interaction, λ is the wavelength and A_{int} is the effective interaction area. This figure of merit (Eq 1-4) is plotted in Fig (1-3) a) for 2 HC-PCF's with different optical attenuations and compared with free space propagation, and capillary guidance. In addition the dephasing rates from atom wall collision and the transit time for a HC-PCF are plotted in Fig (1-3) b).

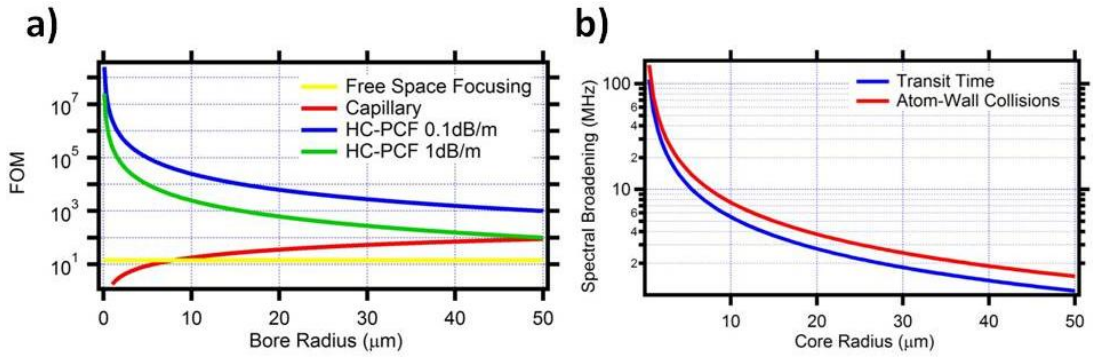

Figure (1-3) a) Figure of merit for two HC-PCF with different optical attenuations, a capillary waveguide and free space propagation for different bore radii at wavelength of 780 nm. (54) **b) Spectral broadening in HC-PCF from transit time (blue) and atom-wall collisions (red).**

An enhancement of gas laser interactions of ~ 10^6 times can be achieved for HC-PCF with small core diameters and optical attenuation of ~ 0.1 dB/m. However for atomic vapour applications the performance is quantified by the fractional frequency stability (Eq (1-3)). Hence it is also important to take into account the Q factor of the atomic resonance in the HC-PCF (Fig (1-3) b). The Q factor is inversely related to the dephasing rates, which in a

HC-PCF are limited by the transit time and the atom wall collisions which both exhibit R^{-1} dependence. In a HC-PCF the SNR is intrinsically given by the f_{om} (Fig (1-3) a) as such small core diameters give ~ 10^6 enhancement of the SNR. However such small core HC-PCF (diameter < 5 μm) give very large additional dephasing > 10 MHz, hence a reduced Q factor. For atomic vapours loaded in HC-PCF it is no longer possible to take these two quantities separately. A balance between SNR and dephasing rate (Q factor) needs to be achieved when selecting the HC-PCF with a specific core diameter. Due to the delicate choice between dephasing and SNR, atomic vapour loaded HC-PCF will never replace primary frequency standards. However applications such as handheld GPS devices requiring reasonable stability but in a compact design will be benefit from such developments.

An additional benefit of utilising HC-PCF as a platform for gas laser interactions is the ease of integration with traditional single mode fibre (SMF) to form photonic microcells (PMC). A PMC is a length of HC-PCF which has been filled with a desired gaseous medium and hermetically spliced to traditional solid fibres forming a compact integrated gas cell. HC-PCF's filled with a range of gaseous mediums from acetylene to hydrogen with diverse applications from slow light generation to stimulated Raman scattering (SRS) have been reported in the literature (48,55–60). However to date none has reported on the Rb vapour loaded PMC.

1.4.2 Progress in Gas Filled HC-PCF

The inherent advantages associated with using HC-PCF for light matter interactions were elucidated in the previous section. Since the pioneering demonstration by Benabid and co-workers of SRS in HC-PCF in 2002 (54) the research of confined dielectric waveguide geometries being used for light matter interactions has expanded. In previous sections discussion is dedicated to the recent developments in confining atomic vapours in hollow dielectric structures. This is an expanding area of research with many attempting to benefit from the strong light matter interactions that confined waveguiding geometries offer over traditional experimental setups. The flexibility afforded by both HC-PCF in terms of tailoring the guidance properties and the filling medium, (i.e. different gases) gives a dynamic range of experimental possibilities. To date Hydrogen (H_2) has been loaded into HC-PCF generating a broadband frequency comb via SRS with potential application for

waveform synthesis (61). Other gas materials such as acetylene for slow and superluminal light have been confined in HC-PCF (62). High harmonic generation (63) and ionised gases (64) based upon Xenon (^{54}Xe) and Argon (^{18}Ar) filled Kagome HC-PCF have been reported in recent years.

1.5 Summary

In this chapter the underlying physics of coherent optical techniques are introduced because these techniques are used in the experimental work presented later in this thesis. In addition a comprehensive review of atom photon interactions in confined dielectric structures is presented. There is a body of work dedicated towards creating and optimising confined atomic vapour dielectric structure geometries utilising several different approaches. These approaches range from MEMS fabrication to hollow core waveguides based on ARROW's and HC-PCF.

In the work presented in this thesis Kagome HC-PCF's are utilised as the host medium for strong light atomic vapour interactions because of the inherent advantages of these fibres such as long interaction lengths, tight transverse mode confinement and easy integration with existing fibre optic networks. Development of Kagome HC-PCF's are presented along with post processing of HC-PCF such as the application of coating materials to the inner core wall. These developments address the challenges associated with atomic vapour confined in micro structured geometries such as HC-PCF. These developments pave the way for the fabrication of atomic vapour PMC's. Experimental demonstrations of EIT, magneto optical spectroscopy, study of novel coating materials and investigation of sub Doppler transparency features in Rb vapour loaded Kagome HC-PCF are presented.

1.6 Thesis Outline

This thesis is comprised of two parts, the first part consists of four chapters detailing the guidance mechanisms of HC-PCF and the contributions made to the development this technology by the author. Chapter 2 introduces both PBG and inhibited coupling guidance mechanisms which allow propagation of light in a hollow core. Chapter 3 presents state of

the art fabrication of PBG HC-PCF for guidance at 780 nm, this includes reporting record losses which have been achieved at this wavelength. Additionally double PBG HC-PCF is reported where the guidance bands have been optimised for guidance at 780 nm and 1.0 μm. Chapter 4 presents the development of enhanced inhibited coupling Kagome HC-PCF whereby the losses of this class of fibre are now comparable with PBG HC-PCF. State of the art losses are reported for hypocycloid core shape Kagome HC-PCF with guidance bands optimised for 780 nm. Additionally numerical and experimental investigation of the cladding effect and the impact of the hypocycloid core curvature on the confinement losses of Kagome HC-PCF are presented. Chapter 5 presents post processing techniques which have been developed and optimised for atomic vapour loaded Kagome HC-PCF. This includes details on the deposition of coating materials to the inner core wall, tapering and sleeve splicing for photonic microcell fabrication.

Part two of this thesis consists of three chapters reporting on experiments loading Rb vapour in Kagome HC-PCF's to study and mitigate some of the inherent drawbacks associated with micron scale confinement of atomic vapours. One of the inherent disadvantages of utilising a HC-PCF or any confined waveguiding geometry is the large surface to volume ratio which enhances the atom surface interaction. The enhanced atom surface interactions leads to a large degree of physio-chemical reactions between the atoms and the surface resulting in a loss of atomic vapour from the hollow core. In chapter 6 aluminosilicate sol-gel is deposited for the first time as a coating material on the inner core wall to reduce the rate of atom surface reactions. Additionally the increased atom surface interaction increases the number of dephasing atom wall collisions. Chapter 7 characterises the performance of antirelaxation coatings in HC-PCF independently from the transit time broadening utilising for the first time a magneto-optical technique (modified Franzen technique). In addition the impact of the hypocycloid geometry of the hollow core fibre on the relaxation time of Rb vapour is investigated. Sub Doppler transparencies such as CPT, EIT and SAS features can be generated in atomic vapours for a range of applications. In chapter 8 the generation of sub Doppler saturable absorption features is presented through a novel technique using only a single laser beam. The physical mechanism behind the formation of these features is characterised experimentally and theoretically discussed.

References

1. Wynands R, Weyers S. Atomic fountain clocks. Metrologia [Internet]. 2005 Jun 7 [cited 2013 Jun 13];42(3):S64–S79. Available from:

http://stacks.iop.org/0026-1394/42/i=3/a=S08?key=crossref.73cd3d68326b49d8f212d76e5079625d

2. Jefferts SR, Shirley J, Parker TE, Heavner TP, Meekhof DM, Nelson C, et al. Accuracy evaluation of NIST-F1. Metrologia [Internet]. 2002 Aug 1;39(4):321–36. Available from: http://stacks.iop.org/0026-1394/39/i=4/a=1?key=crossref.19a7aee8f7486e26152c728d2f73df6e

3. Lombardi MA, Heavner TP, Jefferts SR. NIST Primary Frequency Standards and the Realization of the SI Second. The Journal of Measurement Science. 2007;2(4).

4. Takamoto M, Hong F-L, Higashi R, Katori H. An optical lattice clock. Nature [Internet]. 2005 May 19 [cited 2013 Feb 1];435(7040):321–4. Available from: http://www.ncbi.nlm.nih.gov/pubmed/15902252

5. Le Targat R, Lorini L, Le Coq Y, Zawada M, Guéna J, Abgrall M, et al. Experimental realization of an optical second with strontium lattice clocks. Nature Communications [Internet]. 2013 Jul 9 [cited 2013 Jul 10];4. Available from: http://www.nature.com/doifinder/10.1038/ncomms3109

6. Ensher JR, Matthews MR, Wieman CE, Cornell EA. Observation of Bose-Einstein Condensation in a Dilute Atomic Vapor. 1(ii):4–7.

7. Phillips WD. Laser cooling and trapping of neutral atoms *. Reviews of Modern Physics. 1998;70(3):721–41.

8. Grimm R, Ovchinnikov YB. Optical dipole traps for neutral atoms. Advances In Atomic, Molecular and Optical Physicss. 1987;42(2000):95–170.

9. Corwin KL, Lu ZT, Hand CF, Epstein RJ, Wieman CE. Frequency-stabilized diode laser with the Zeeman shift in an atomic vapor. Applied optics [Internet]. 1998 May 20;37(15):3295–8. Available from: http://www.ncbi.nlm.nih.gov/pubmed/18273286

10. Mcferran JJ, Magalhães D V, Mandache C, Millo J, Zhang W. 199 Hg 1 S − 3 P clock transition with Laser locking to p the. 2012;37(17):3477–9.

11. Sheng D, Li S, Dural N, Romalis M V. Subfemtotesla Scalar Atomic Magnetometry Using Multipass Cells. 2013;160802(April):1–5.

12. Budker D, Kimball D, Rochester S, Yashchuk V, Zolotorev M. Sensitive magnetometry based on nonlinear magneto-optical rotation. Physical Review A [Internet]. 2000 Sep;62(4):043403. Available from: http://link.aps.org/doi/10.1103/PhysRevA.62.043403

13. Akulshin AM, Sautenkov VA, Velichansky VL, Zibrov AS. POWER BROADENING OF SATURATION A B S O R P T I O N R E S O N A N C E ON THE D2 LINE OF RUBIDIUM. Optics Communications. 1990;77(4):30–3.

14. Harris SE. Lasers without Inversion: Interference of Lifetime-Broadened Resonances. Physical Review Letters. 1989;62(9):1033–6.

15. Boller KJ, Imamoglu A, Harris SE. Observation of Electromagnetically Induced Transparency. Physical Review Letters. 1991;66(20):2593–6.

16. Arimondo E. Coherent Population Trapping in Laser Spectroscopy.

17. Ramsey NF. A Molecular Beam Resonance Method with Seperated Oscillating Fields. Physical Review. 1950;78(6):695–7.

18. Ramsey N. EXPERIMENTS WITH SEPARATED OSCILLA- TORY FIELDS AND HYDROGEN MASERS. Nobel Lecture. 1989;

19. Scully, M O and Zubairy MS. Quantum Optics. Cambridge University Press; 1997.

20. Fleischhauer M, Marangos JP. Electromagnetically induced transparency : Optics in coherent media. Reviews of Modern Physics. 2005;77(April):633–73.

21. Marangos JP, Optics L, Group S. Topical review Electromagnetically induced transparency. Journal of Modern Optics. 1998;45(3):471–503.

22. Demtroder W. 3 . Widths and Profiles of Spectral Lines. Laser Spectroscopy: Volume 1 Basic Principles. 2008. p. 61–98.

23. Shimoda K. 2 . Line Broadening and Narrowing Effects. High Resolution Laser Spectroscopy. New York: Springer-Verlag; 1964. p. 11–49.

24. Rautian SG, Sobel'man II. THE EFFECT OF COLLISIONS ON THE DOPPLER BROADENING OF SPECTRAL LINES. Soviet Physics Uspekhi. 1967;9(5):701–16.

25. Labachelerie M De, Nakagawa K, Ohtsu M. Ultranarrow 13 C2H2 saturated-absorption lines at 1.5um. Optics Letters. 1994;19(11):840–2.

26. Alzetta G, Gozzii AI, Moi L. An Experimental Method for the Observation of R . F . Transitions and Laser Beat Resonances in Oriented Na Vapour . Il Nuovo Cimento. 1976;36(1).

27. Kocharovskaya OA, Khanin YI. Coherent amplification of an ultrashort pulse in a 3-level medium without a population-inversion. JETP Letters. 1988;48(11):630–4.

28. Harris SE, Field JE, Kasapi A. Dispersive properties of electromagnetically induced transparency. Physical Review A. 1992;46(1):29–32.

29. Hau LV, Harris SE, Dutton Z, Behroozi CH. Light speed reduction to 17 metres per second in an ultracold atomic gas. 1999;397(February):594–8.

30. Allan DW. Statistics of atomic frequency standards. Proceedings of the IEEE [Internet]. 1966;54(2):221–30. Available from: http://ieeexplore.ieee.org/lpdocs/epic03/wrapper.htm?arnumber=1446564

31. Cutler LS, L SC. Some Aspects of the Theorv and Measurement of Frequency Fluctuations in Frequency Standards. Proceedings of the IEEE. 1966;54(2):136–54.

32. Hall J. Nobel Lecture: Defining and measuring optical frequencies. Reviews of Modern Physics [Internet]. 2006 Nov [cited 2013 May 26];78(4):1279–95. Available from: http://link.aps.org/doi/10.1103/RevModPhys.78.1279

33. Happer W. Optical Pumping. Reviews of Modern Physics. 1972;44(2):169–222.

34. Budker D, Fizyki I, Smoluchowskiego M, Jagiellon U, Weis A. Resonant nonlinear magneto-optical effects in atoms *. Reviews of Modern Physics. 2002;74(October).

35. Knappe S, Shah V, Schwindt PDD, Hollberg L, Kitching J, Liew L-A, et al. A microfabricated atomic clock. Applied Physics Letters [Internet]. 2004 [cited 2013 Feb 13];85(9):1460. Available from: http://link.aip.org/link/APPLAB/v85/i9/p1460/s1&Agg=doi

36. Spillane S, Pati G, Salit K, Hall M, Kumar P, Beausoleil R, et al. Observation of Nonlinear Optical Interactions of Ultralow Levels of Light in a Tapered Optical Nanofiber Embedded in a Hot Rubidium Vapor. Physical Review Letters [Internet]. 2008 Jun [cited 2013 Feb 13];100(23):233602. Available from: http://link.aps.org/doi/10.1103/PhysRevLett.100.233602

37. Demtroder W. Laser Spectroscopy Vol. 2: Experimental Techniques. Fourth. New York: Springer; 2008.

38. Hendrickson SM, Lai MM, Pittman TB, Franson JD. Observation of Two-Photon Absorption at Low Power Levels Using Tapered Optical Fibers in Rubidium Vapor. Physical Review Letters [Internet]. 2010 Oct [cited 2013 Mar 1];105(17):173602. Available from: http://link.aps.org/doi/10.1103/PhysRevLett.105.173602

39. Hendrickson SM, Pittman TB, Franson JD. Nonlinear transmission through a tapered fiber in rubidium vapor. Journal of the Optical Society of America B [Internet]. 2009 Jan 22;26(2):267. Available from: http://www.opticsinfobase.org/abstract.cfm?URI=josab-26-2-267

40. Yang W, Conkey DB, Wu B, Yin D, Hawkins AR, Schmidt H. Atomic spectroscopy on a chip. Nature Photonics [Internet]. 2007 Jun [cited 2013 Feb 13];1(6):331–5. Available from: http://www.nature.com/doifinder/10.1038/nphoton.2007.74

41. Wu B, Hulbert JF, Lunt EJ, Hurd K, Hawkins AR, Schmidt H. Slow light on a chip via atomic quantum state control. Nature Publishing Group; 2010;4(November):5–8. Available from: http://dx.doi.org/10.1038/nphoton.2010.211

42. Ghosh S, Bhagwat A, Renshaw C, Goh S, Gaeta A, Kirby B. Low-Light-Level Optical Interactions with Rubidium Vapor in a Photonic Band-Gap Fiber. Physical Review Letters [Internet]. 2006 Jul [cited 2013 Feb 13];97(2):023603. Available from: http://link.aps.org/doi/10.1103/PhysRevLett.97.023603

43. Slepkov AD, Bhagwat AR, Venkataraman V, Londero P, Gaeta AL. Spectroscopy of Rb atoms in hollow-core fibers. Physical Review A [Internet]. 2010 May [cited 2013 Feb 25];81(5):053825. Available from: http://link.aps.org/doi/10.1103/PhysRevA.81.053825

44. Bajcsy M, Hofferberth S, Peyronel T, Balic V, Liang Q, Zibrov AS, et al. Laser-cooled atoms inside a hollow-core photonic-crystal fiber. 2011;1–10.

45. Christensen C, Will S, Saba M, Jo G-B, Shin Y-I, Ketterle W, et al. Trapping of ultracold atoms in a hollow-core photonic crystal fiber. Physical Review A [Internet]. 2008 Sep [cited 2013 Feb 7];78(3):033429. Available from: http://link.aps.org/doi/10.1103/PhysRevA.78.033429

46. Takekoshi T, Knize R. Optical Guiding of Atoms through a Hollow-Core Photonic Band-Gap Fiber. Physical Review Letters [Internet]. 2007 May [cited 2013 Feb 14];98(21):210404. Available from: http://link.aps.org/doi/10.1103/PhysRevLett.98.210404

47. Vorrath S, Möller S a, Windpassinger P, Bongs K, Sengstock K. Efficient guiding of cold atoms through a photonic band gap fiber. New Journal of Physics [Internet]. 2010 Dec 9 [cited 2013 Feb 14];12(12):123015. Available from: http://stacks.iop.org/1367-2630/12/i=12/a=123015?key=crossref.fef11793f31fc43564898ca281f561d8

48. Light PS, Benabid F, Couny F, Maric M, Luiten a N. Electromagnetically induced transparency in Rb-filled coated hollow-core photonic crystal fiber. Optics letters [Internet]. 2007 May 15;32(10):1323–5. Available from: http://www.ncbi.nlm.nih.gov/pubmed/17440575

49. Wu B, Hulbert JF, Hawkins AR, Member S. Planar Hollow-Core Waveguide Technology for Atomic Spectroscopy and Quantum Interference in Alkali Vapors. 2008;26(23):3727–33.

50. Benabid F, Couny F, Knight JC, Birks T a, Russell PSJ. Compact, stable and efficient all-fibre gas cells using hollow-core photonic crystal fibres. Nature [Internet]. 2005 Mar 24;434(7032):488–91. Available from: http://www.ncbi.nlm.nih.gov/pubmed/15791251

51. Benabid F, Roberts PJ, Couny F, Light PS. Light and gas confinement in hollow-core photonic crystal fibre based photonic microcells. Journal of the European Optical Society: Rapid Publications [Internet]. 2009 Jan 21 [cited 2013 Feb 21];4(c):09004. Available from: https://www.jeos.org/index.php/jeos_rp/article/view/09004

52. Benabid F, Knight JC, Antonopoulos G, Russell PSJ. Stimulated Raman scattering in hydrogen-filled hollow-core photonic crystal fiber. Science (New York, N.Y.) [Internet]. 2002 Oct 11 [cited 2013 May 22];298(5592):399–402. Available from: http://www.ncbi.nlm.nih.gov/pubmed/12376698

53. Benabid F. Hollow-core photonic bandgap fibre: new light guidance for new science and technology. Philosophical transactions. Series A, Mathematical, physical, and engineering sciences [Internet]. 2006 Dec 15 [cited 2013 Jan 29];364(1849):3439–62. Available from: http://www.ncbi.nlm.nih.gov/pubmed/17090469

54. Benabid F, Knight JC, Antonopoulos G, Russell PSJ. Stimulated Raman scattering in hydrogen-filled hollow-core photonic crystal fiber. Science (New York, N.Y.) [Internet]. 2002 Oct 11 [cited 2013 Feb 8];298(5592):399–402. Available from: http://www.ncbi.nlm.nih.gov/pubmed/12376698

55. Lurie A, Baynes FN, Anstie JD, Light PS, Benabid F, Stace TM, et al. High-performance iodine fiber frequency standard. Optics letters [Internet]. 2011 Dec 15;36(24):4776–8. Available from: http://www.ncbi.nlm.nih.gov/pubmed/22179880

56. Cubillas AM, Hald J, Petersen JC. High resolution spectroscopy of ammonia in a hollow-core fiber. Optics express [Internet]. 2008 Mar 17;16(6):3976–85. Available from: http://www.ncbi.nlm.nih.gov/pubmed/18542495

57. Henningsen J, Hald J, Peterson JC. Saturated absorption in acetylene and hydrogen cyanide in hollow-core photonic bandgap fibers. Optics express [Internet]. 2005 Dec 26;13(26):10475–82. Available from: http://www.ncbi.nlm.nih.gov/pubmed/19503263

58. Lynch-Klarup KE, Mondloch ED, Raymer MG, Arrestier D, Gerome F, Benabid F. Supercritical xenon-filled hollow-core photonic bandgap fiber. Optics Express [Internet]. 2013 May 31 [cited 2013 Jun 3];21(11):13726. Available from: http://www.opticsinfobase.org/abstract.cfm?URI=oe-21-11-13726

59. Wang Y, Couny F, Light PS, Mangan BJ, Benabid F. Compact and portable multiline UV and visible Raman lasers in hydrogen-filled HC-PCF. Optics Letters [Internet]. Optical Society of America; 2010;35(8):1127–9. Available from: http://ieeexplore.ieee.org/search/srchabstract.jsp?navigation=no&arnumber=5500475

60. Sprague MR, England DG, Abdolvand A, Nunn J, Jin X-M, Steven Kolthammer W, et al. Efficient optical pumping and high optical depth in a hollow-core photonic-crystal fibre for a broadband quantum memory. New Journal of

Physics [Internet]. 2013 May 20 [cited 2013 Jun 20];15(5):055013. Available from: http://stacks.iop.org/1367-2630/15/i=5/a=055013?key=crossref.7e045d0599a8d13687edf614674d873c

61. Couny F, Benabid F, Roberts PJ, Light PS, Raymer MG. Generation and photonic guidance of multi-octave optical-frequency combs. Science [Internet]. 2007;318(5853):1118–21. Available from: http://opus.bath.ac.uk/8665/

62. Wheeler N V, Light PS, Couny F, Benabid F. Slow and Superluminal Light Pulses Via EIT in a. Journal of Lightwave Technology. 2010;28(6):870–5.

63. Heckl OH, Baer CRE, Kränkel C, Marchese S V., Schapper F, Holler M, et al. High harmonic generation in a gas-filled hollow-core photonic crystal fiber. Applied Physics B [Internet]. 2009 Oct 14 [cited 2013 Aug 8];97(2):369–73. Available from: http://link.springer.com/10.1007/s00340-009-3771-x

64. Debord B, Gérôme F, Jamier R, Boisse-Laporte C, Leprince P, Leroy O, et al. First Ignition of an UV Microwave Microplasma in Ar-filled Hollow-Core Photonic Crystal Fibers. 37th European Conference and Exposition on Optical Communications [Internet]. Washington, D.C.: Osa; 2011. p. Mo.2.LeCervin.5. Available from: http://www.opticsinfobase.org/abstract.cfm?URI=ECOC-2011-Mo.2.LeCervin.5

Part I

Hollow core photonic crystal fibre (HC-PCF) is a maturing technology whereby researchers are now targeting the fabrication of HC-PCF with specific properties for unique applications. In parallel with the development of HC-PCF has been the vast under taking of loading gaseous media in HC-PCF for nonlinear optics and frequency metrology. Probably the most challenging gas media to load are atomic vapours. However because of their diverse application such as frequency standards, magneto optical spectroscopy, laser cooling and single particle interactions it is a worthwhile pursuit to load atomic vapours in HC-PCF. The breadth of optical phenomena which are possible in atomic vapours requires an equally diverse range of HC-PCF to host the light atomic vapour interaction.

Part one of this thesis consists of four individual chapters which introduce prior knowledge of HC-PCF and work which has been performed by the author on developing and characterising HC-PCF for atomic vapour applications. Chapter 2 is the first chapter in part one and introduces the physical mechanism behind the guidance of light in a hollow core photonic crystal fibre. This first chapter introduces both photonic bandgap and inhibited coupling guidance which are the two distinct mechanisms whereby light can be guided in a low index core region with low propagation losses. The photonic tight binding model is introduced which intuitively describes the formation of a photonic bandgap based upon the bringing together of individual optical resonators akin to the electronic tight binding model. Chapter 3 introduces photonic bandgap HC-PCF which have been fabricated by the author for low loss transmission centred at 780 nm for Rb vapour atomic transitions. This includes two single photonic bandgap HC-PCF, one 7 cell and one 19 cell core defect fibres. Additionally a double photonic bandgap HC-PCF with optimised guidance bands is reported for atomic vapour applications. Chapter 4 introduces enhanced inhibited coupling guidance in hypocycloid core shape Kagome HC-PCF by engineering of the core cladding interface from a traditional circular core shape to a hypocycloid core shape with negative curvature. A 7 cell core defect Kagome HC-PCF is reported which has been engineered for extremely low loss around the atomic

transitions of Rb. This Kagome HC-PCF has been used to investigate the bending loss mechanism in inhibited coupling Kagome HC-PCF. Additionally experimental and theoretical studies have been carried out on the impact of the cladding structure and the hypocycloid curvature on the inhibited coupling guidance mechanism. In the final chapter of part one the post processing techniques which are routinely used in this thesis for the preparation of atomic vapour loaded HC-PCF are presented. These post processing techniques include the application of coating materials to the inner wall of the core cladding interface and the physical processing of fibres themselves such as tapering and splicing. Application of coating materials is directed at combating loss of atomic vapour by physio-chemical absorption and dephasing collisions due to the extremely confined geometry of the hollow core. Physical post processing of the fibre structure is directed towards the future fabrication of an atomic vapour photonic microcell.

Chapter 2

Prior Knowledge: Hollow Core Photonic Crystal Fibre Guidance Theory

In this chapter, two classes of hollow core photonic crystal fibres (HC-PCF) are introduced. The first guides using a cladding designed to exhibit a photonic bandgap (PBG) and the second through inhibited coupling between modes supported in the core and cladding regions.

2.1 Introduction

Two classes of hollow core photonic crystal fibre (HC-PCF) are presented which can be readily identified into two distinct categories as photonic bandgap (PBG) and inhibited coupling (IC) guiding. The salient differences in the guidance mechanism and optical properties of PBG and IC HC-PCF are discussed in the upcoming sections. The first report of light guidance in an air core utilising a two dimensional out of plane photonic bandgap (PBG) was given by Cregan *et al.* in 1999 (1).

2.2 Photonic Bandgap guiding HC-PCF

By far the most studied PBG HC-PCF is the one whose cladding structure consists of a regular triangular lattice of air holes separated by a periodic web of thin silica struts. In a triangular lattice of air holes cladding structure, the periodic silica web air hole structure provides the two dimensional out of plane photonic bandgap (2). Propagation of light with specific spectral ranges, and specific effective indices is forbidden through this photonic structure. However propagation is only forbidden in this spectral frequency region for a relatively smaller number of optical modes with

propagation constant, $\beta = n_{eff}k$ close to the air line, where n_{eff} is the mode effective refractive index and k is the free space propagation constant.

Unlike in-plane configuration (3) , out of plane PBG formation is possible because the important index step is no longer just the ratio of the material indices n_{silica}/n_{air} = 1.46 but rather the transverse effective index step, $n_{gl,\perp}/n_{air,\perp} = k_{gl,\perp}/k_{air,\perp}$ (4). Figure (2-1) is an illustrative plot of the density of photonic states (DOPS) for a given periodic silica/air structure (4).

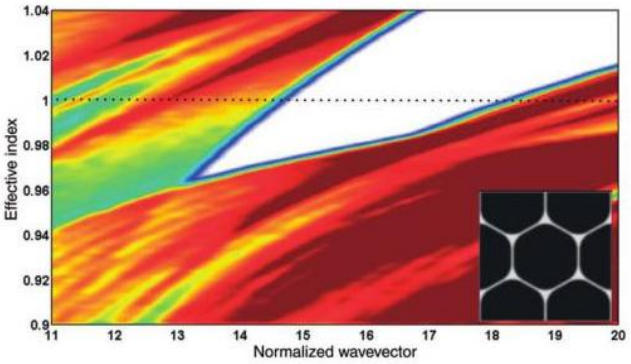

Figure (2-1) Density of photonic states (DOPS) of photonic bandgap for a given silica/air structure shown in inset(4)**.**

In Fig (2-1) the DOPS is plotted for the cladding structure shown in the inset, this is an example of the solutions which can be obtained by solving the Maxwell-Helmholtz equation by planewave analysis or finite element method. The coloured regions (Fig (2-1)) represent states supported by the photonic crystal cladding while the white region indicates an absence of supported modes, i.e. a PBG. The graduated colour scale depicts the number of modes at a specific n_{eff} and normalised frequency, the darker red indicates the maximum number of modes present while white indicates a complete absence of modes. The absence of any states below the air line (effective index = 1) allows for a select number of optical modes with specific propagation constant (β) to be guided in a hollow defect. The number of modes is determined by the size and shape of the hollow defect. While solving the Maxwell Helmholtz equation provides a powerful tool for mapping out the full dispersion relations (β, k) (e.g. Fig (2-1)) of all the modes of the particular cladding structure, it does not provide an intuitive picture about the bandgap formation or the modal spectrum of the cladding photonic structure. An intuitive depiction of bandgap

formation in a photonic crystal fibre is given in the next section based on the photonic tight binding model developed by Benabid and co-workers (4,5).

2.3 Photonic Tight Binding Model

The photonic tight binding model (PTBM), akin to the solid state electronic tight binding model, depicts the formation of a photonic bandgap. Prior to the development of the PTBM, other models were developed depicting an intuitive picture of cladding DOPS including the "cellular method" presented by Birks *et al.* (6) and the anti resonant reflective optical waveguide (ARROW) model (7,8). The ARROW model describes the formation of cladding pass bands based upon the thickness of the high index cladding regions while assuming the separation of these features is significantly greater than the operation wavelength, ($\Lambda > \lambda$) (7). The "cellular method" is a semi-analytical approach which unlike the ARROW model includes the dimensions of the low index separation between the high index resonators. The cellular model provides more detail on the width of the cladding pass bands for low index contrast structures such as all solid PBG PCF. However, none of these models give an account on how PBG's are formed and the role of the different structural cladding features such as the ones found in the complicated cladding geometry of HC-PCF.

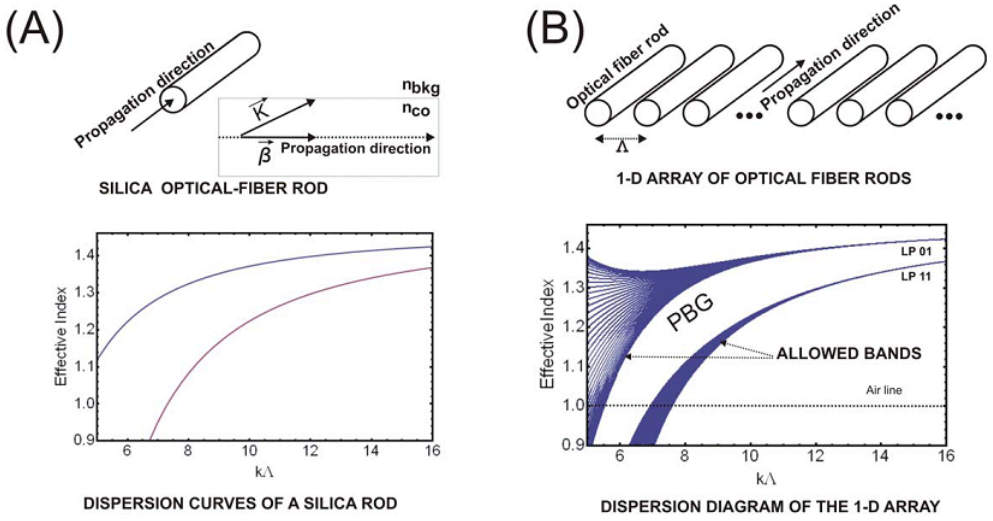

Figure(2-3)a) Single optical resonators dispersion curves, b) Multiple optical resonators in close proximity and associated dispersion curves, (4,5)

The PTBM is a development in the understanding of PBG formation in HC-PCF it builds upon prior work. In the electronic tight binding model individual atoms have distinct wave functions and discrete energy levels (4,5). When the individual atoms are brought into close proximity as in a crystal lattice the wave functions overlap and hybridise, leading to the formation of distinct allowed energy bands and bandgaps. In the photonic tight binding model the atoms are replaced by individual photonic sites (e.g. silica rods) which act as optical resonators. The principles of the model are outlined above (Fig (2-3)), in a) the dispersion curves of a single silica rod (optical resonator akin to an isolated atom) are presented, the distinct optical modes that the individual rod supports can be observed. In the second panel (Fig (2-3) b) the dispersion curves for an array of optical rods spaced by Λ (akin to atoms in a crystal lattice) is presented and allowed bands and bandgaps have clearly developed akin to the solid state electronic tight binding model.

The PTBM has been applied with great success to PBG guiding HC-PCF (Fig (2-4) a) & b). Here the density of photonic states (DOPS) (Fig (2-4) c) is plotted for the structure shown in Fig (2-4) a) where the bandgap is the black region with no supported optical modes surrounded by regions of optical states supported in the cladding structure. In this model the individual photonic resonators which support the optical modes defining the allowed photonic bands are identified (9).

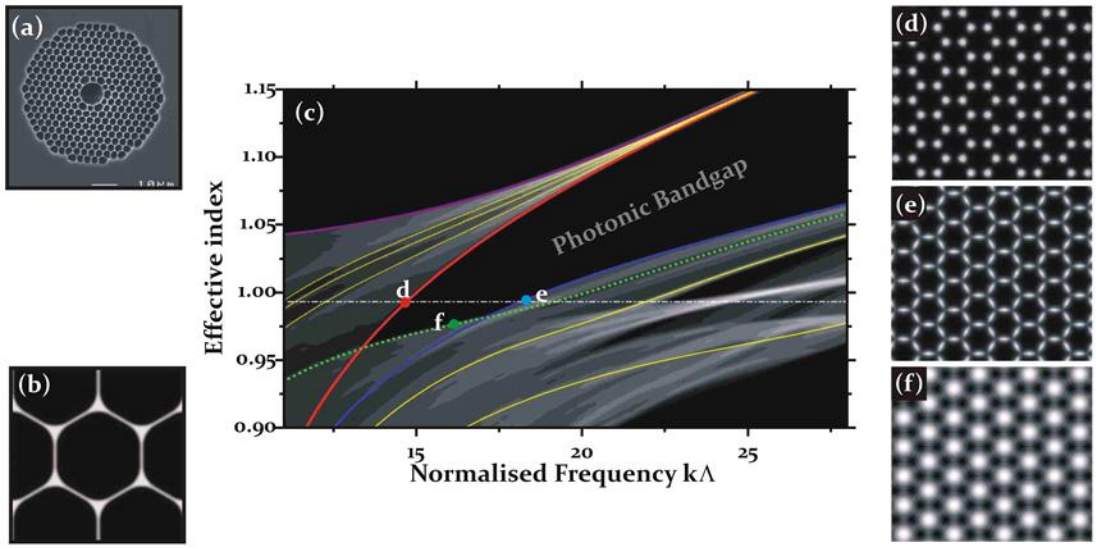

Figure (2-4) a) SEM HC-PCF, b) SEM HC-PCF cladding structure, c)DOPS for fibre in a), d) silica apex mode, e) silica strut mode, f) cladding air hole mode (4,5)

The optical mode which bounds the low frequency edge of the PBG are defined by the silica apex mode (Fig (2-4) d) corresponding to point d in the DOPS plot (Fig (2-4) c). The high frequency edge of the PBG is defined by a hybridisation of two optical resonators provided here by the optical modes supported in the silica struts of the photonic crystal cladding (Fig (2-4) e) and the modes supported in the air hole of the photonic crystal cladding Fig (2-4) f). These modes are located at e) and f) respectively in the DOPS plot (Fig (2-4) c). The modes identified in this theoretical model have been observed experimentally by Couny *et al.* (9) using scanning near field optical microscopy (SNOM) on a short length of PBG HC-PCF.

2.4 Double Photonic Bandgap HC-PCF

The development of the PTBM allowed the identification of the individual resonators which lead to the formation of a photonic bandgap in periodic triangular lattice of air holes separated by thin silica struts. This development allowed the exploitation of the exact size and diameter of the different resonators leading to the opening of a secondary bandgap below the air line at higher normalised frequency. Prior work reported by Light *et al.* (10) allowed for guidance of 1550 nm Erbium doped fibre lasers with those of Nd:YAG or Ytterbium fibre lasers at 1 μm in a single hollow core fibre. To date there has been no report of shifting these two PBGs to shorter wavelengths such as 800 nm and 1 μm.

Engineering the photonic crystal cladding structure by adjusting the aspect ratio of the photonic resonators identified using the PTBM allows secondary bandgap at higher normalised frequency to be opened. In Fig (2-5) the density of photonic states (DOPS) of the inset photonic crystal structure are plotted for different struts thicknesses and apex diameters. In the left hand column of Fig (2-5) the strut thickness is maintained constant and the apex radius is increased from top to bottom. The primary bandgap widens and deepens as the apex radius increases while the secondary bandgap closes. In the right hand column of Fig (2-5) the strut thickness is increased from top to bottom and the apex radius is fixed. Here the second bandgap gets deeper as the spectral width of the primary bandgap decreases. The optimised strut thickness and apex diameter is found in the middle panel of the right hand column. Following the identification of the ideal photonic crystal cladding

structure using the PTBM it became possible to design a HC-PCF with a secondary bandgap at higher normalised frequency (10). In such a structure it was shown that a secondary bandgap opened up at higher normalised frequency as predicted by the PTBM. The fabrication of such a structure requires achieving a high air filling fraction (> 97%) HC-PCF but when combined with tailoring the cladding pitch for shorter wavelength operation this presents a significant fabrication challenge requiring exact control of all the draw parameters.

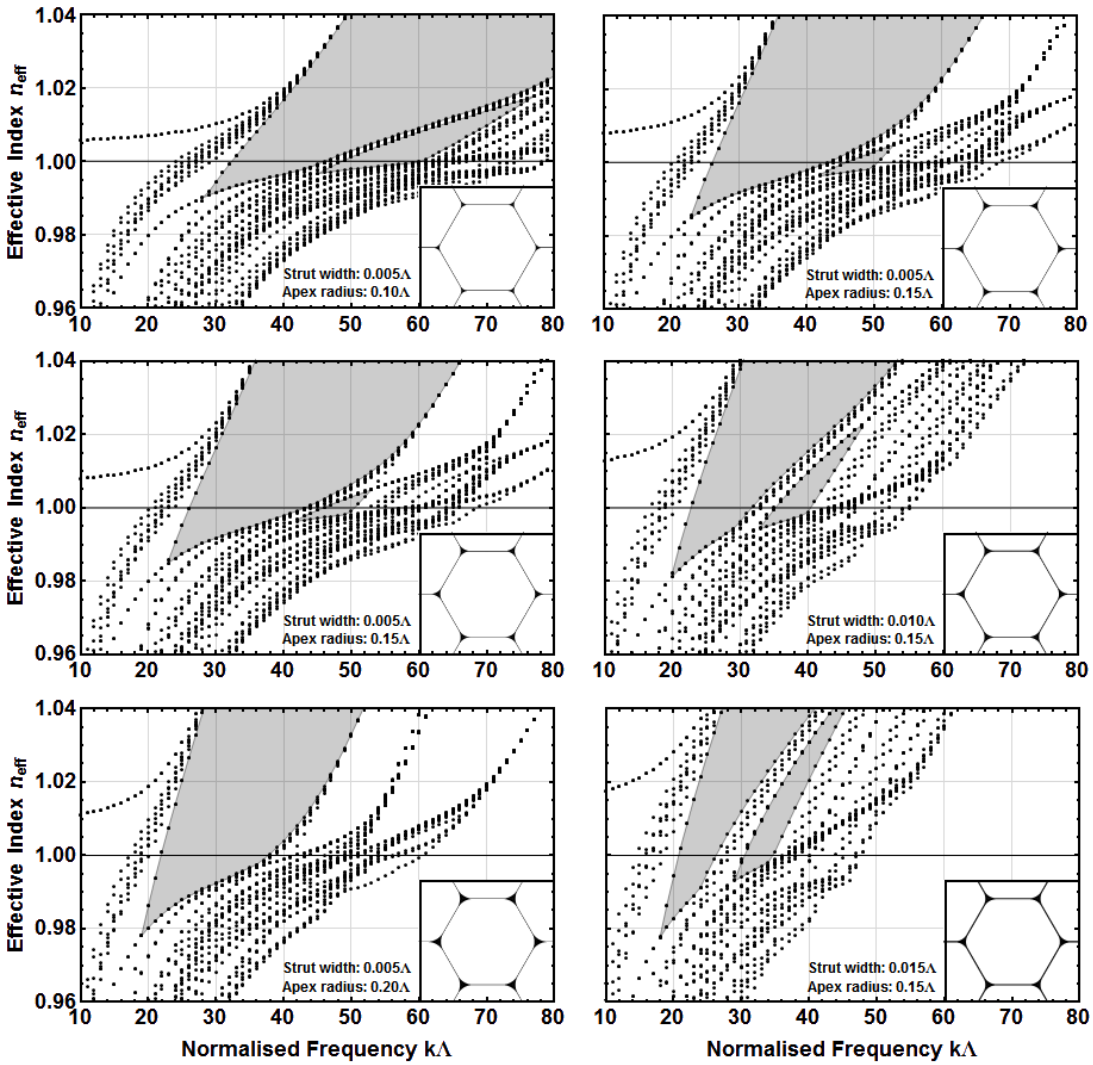

Figure (2-5) Left Hand Column: DOPS plots for HC-PCF with fixed strut width and varying apex radius from 0.1Λ – 0.2Λ, Right Hand Column: DOPS plots for HC-PCF with fixed apex radius and varying strut width from 0.005Λ – 0.015Λ (10)

2.5 Inhibited Coupling Kagome lattice HC-PCF

Large pitch Kagome HC-PCF's first reported in 2002 by Benabid *et al.* (11) are intrinsically different from PBG HC-PCF in both their optical properties and guidance mechanism. In a triangular lattice HC-PCF (Fig (2-6) a) the photonic crystal cladding gives rise to a 2 dimensional out of plane photonic bandgap whereby introduction of a core defect in the perfectly periodic cladding structure allows a few modes to propagate with extremely low optical losses. However in comparison a Kagome lattice HC-PCF does not possess a photonic bandgap as can be seen in DOPS plot of Fig (2-6) b). In the DOPS plot there are two regions of low density of states separated by a region of high density states which correspond to the experimentally observed high loss regions of the core guided mode (5,12).

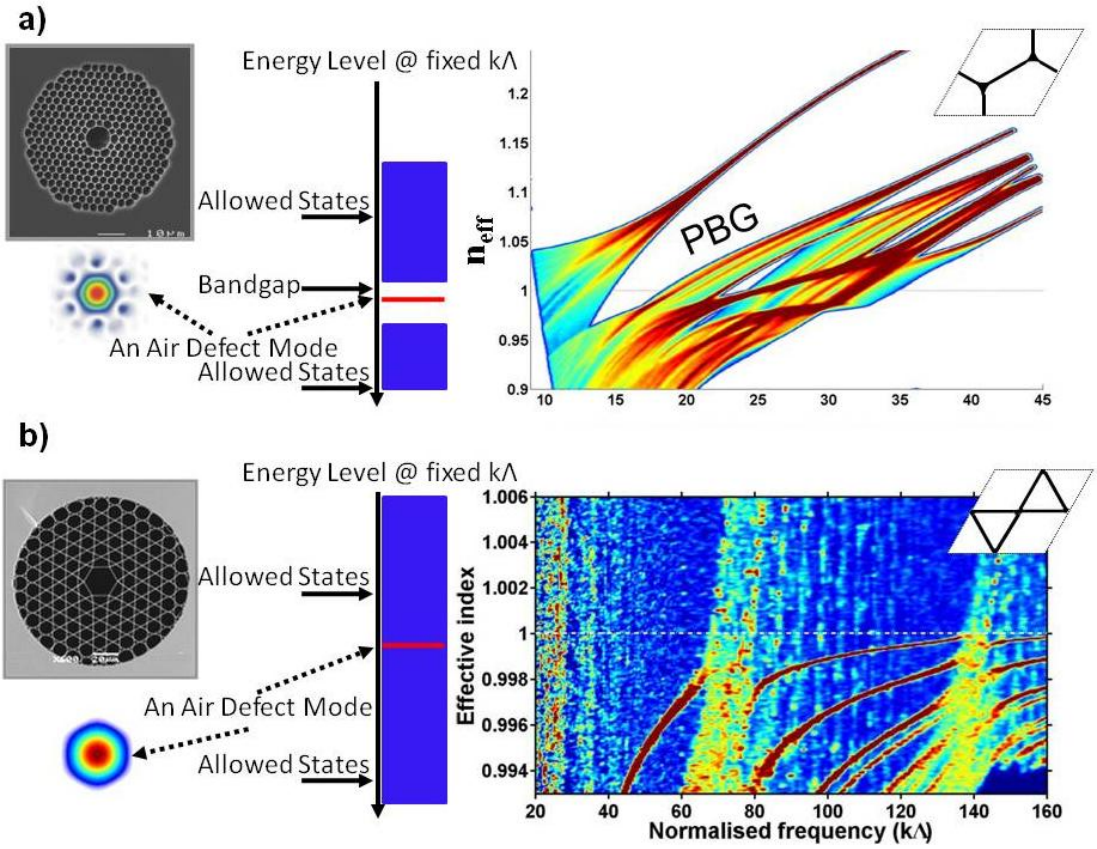

Figure (2-6) a) DOPS of a PBG HC-PCF, b) DOPS of a Large pitch Kagome HC-PCF (5)

Such a Kagome structure has experimentally been shown to support a quasi Gaussian core mode (13). For a number of years the guidance mechanism of Kagome HC-PCF was not completely understood, the answer was provided by Couny *et al.* in 2007 (14). In the work of Couny *et al.* (13,14) the mechanism

proposed for the guidance of a core mode within a continuum of cladding modes was akin to a Von Neumann Wigner electronic state in quantum mechanics. It was proposed that the poor transverse spatial overlap and phase mismatch between the slowly varying core guided mode and the fast oscillating continuum cladding modes provided an inhibited coupling guidance mechanism (5,12).

The slowly varying core mode (Fig (2-7) a) has very low spatial overlap with the silica core surround where less than 0.05% of the maximum intensity resides in the silica, hence very little light interacts with the fast oscillating cladding modes (Fig (2-7) b) which are primarily localised in the silica struts. This plus the rapid oscillation of the transverse wave-vector of the cladding modes results in an inhibition of the interaction between the two modes classes (central panel Fig (2-7)) (5).

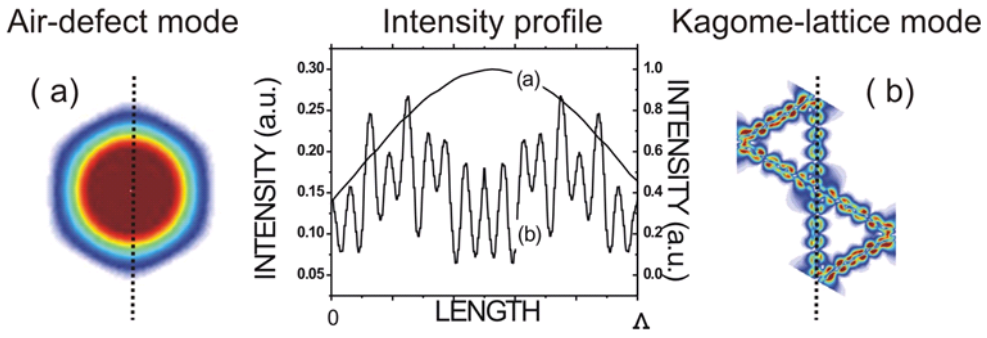

Figure (2-7) a) Core defect mode of Kagome HC-PCF, b) Intensity plot of (a) Core mode and (b) fast oscillating cladding mode, c) Fast oscillating cladding mode of Kagome HC-PCF (5)

In the DOPS (Fig (2-6) b) there exist regions of high density of states which correspond to resonance with the cladding structure where the optical losses of the fibre are high. These resonance wavelengths, λ can be predicted by Eq (2-1) (12). These regions of high attenuation can be observed experimentally separating the spectral guidance bands of the Kagome fibres and predicted by,

$$\lambda = \frac{2t}{j}\left(n_g^2 - n_{air}^2\right)^{1/2}, \qquad (2\text{-}1)$$

where n_g is the refractive index of the silica glass, n_{air} is the index of the air, j is the mode order and t is the thickness of the silica struts composing the Star of David Kagome lattice structure.

2.6 Stack and Draw

HC-PCF's are fabricated through a traditional stack and draw process (15). Thin wall low OH content fused silica tubes (Heraeus F300) with wall thickness ~ 1 mm and outer diameter ~ 20 mm are drawn down to capillaries with outer diameters in the range typically between 1 – 2 mm. These capillaries are stacked in a hexagonal arrangement and inserted in a jacketing tube to form a stack. This stack is drawn down to canes which are an intermediate stage before fibre fabrication with outer diameter typically between 3 – 6 mm. In a typical stack draw between 20 - 30 1.1 m canes can be drawn. Canes can then be drawn as required to fibre with outer diameter typically in the region 110 – 350 μm. Hundreds of metres of fibre can typically be drawn from a single cane depending on the final outer diameter of the fibre and the specific draw parameters used. In the fibre drawing stage the final fibre structure is tailored by independent pressurisation of the core and cladding, and precise control of the draw parameters such as furnace temperature. All the HC-PCF reported in this thesis were fabricated by the stack and draw method.

2.7 Atomic vapour applications of PBG and IC Kagome HC-PCF

In this chapter and expanded on in the following two chapters, two unique classes of HC-PCF with very different optical and physical properties have been introduced. These two classes have both been fabricated and developed for atomic vapour based applications. Given the unique properties of both PBG guiding and inhibited coupling Kagome HC-PCF both types of fibres have applications for specific atomic vapour loading applications. One of the potential applications are single particle interactions which require small mode volumes such as are achievable in optical cavities (16,17). When the small core diameters of PBG HC-PCF are taken together with low propagation losses and excellent single mode properties it seems readily apparent that this class of fibres are an excellent candidate for single particle interactions in atomic vapours (18). On the other hand IC Kagome HC-PCF with their large core diameters, increased optical bandwidth compared to PBG guiding HC-PCF and excellent modal properties are ideal for applications requiring fast atomic vapour loading or extended coherence lifetimes (19) compared to PBG HC-PCF. HC-PCF based frequency standards (20,21) or slow light (22) applications will

benefit from larger diameter Kagome HC-PCF because of the reduced dephasing collisions with the wall.

2.8 Summary

The development of PBG guiding HC-PCF is introduced and the guidance mechanism elucidated. The PTBM akin to the electronic tight binding model from solid state physics is introduced to describe the formation of a PBG. DPBG HC-PCF was developed utilising the PTBM and previous experimental results demonstrating robust guidance in two spectral regions separated by > 70 THz are reported. Finally inhibited coupling guidance in Kagome lattice HC-PCF is introduced and the guidance mechanism explained. The physical and optical properties of the two classes of HC-PCF can be tailored towards specific atomic vapour applications as such both classes have been fabricated by the author and are discussed in the two upcoming chapters. Development of low loss PBG HC-PCF with specific optical and physical properties is presented in detail in chapter 3. Experimental and theoretical developments of hypocycloid core shape Kagome HC-PCF are presented in chapter 4.

References

1. Cregan RF, Mangan BJ, Knight JC, Birks TA, Russell PSJ, Roberts PJ, et al. Single-Mode Photonic Band Gap Guidance of Light in Air. Science [Internet]. 1999 Sep 3 [cited 2013 Feb 18];285(5433):1537–9. Available from: http://www.sciencemag.org/cgi/doi/10.1126/science.285.5433.1537

2. Birks TA, Roberts PJ, Russell PSJ, Atkin DM, Shepherd TJ. Full 2-D photonic bandgaps in silica/air structures. Electronics Letters. 1995;31(22):1941–3.

3. Joannopoulos JD, Johnson SG, Meade RD, Winn JN. Photonic Crsytals: Molding the flow of light. Second. Princeton University Press; 2008. p. 302.

4. Benabid F, Roberts PJ. Linear and nonlinear optical properties of hollow core photonic crystal fiber. Journal of Modern Optics. 2011;58(2):87–124.

5. Benabid F, Roberts PJ, Couny F, Light PS. Light and gas confinement in hollow-core photonic crystal fibre based photonic microcells. Journal of the European Optical Society: Rapid Publications [Internet]. 2009 Jan 21 [cited 2013 Feb 21];4(c):09004. Available from: https://www.jeos.org/index.php/jeos_rp/article/view/09004

6. Birks T a, Pearce GJ, Bird DM. Approximate band structure calculation for photonic bandgap fibres. Optics express [Internet]. 2006 Oct 2;14(20):9483–90. Available from: http://www.ncbi.nlm.nih.gov/pubmed/19529335

7. Litchinitser NM, Abeeluck a K, Headley C, Eggleton BJ. Antiresonant reflecting photonic crystal optical waveguides. Optics letters [Internet]. 2002 Sep 15;27(18):1592–4. Available from: http://www.ncbi.nlm.nih.gov/pubmed/18026511

8. White TP, McPhedran RC, Martijnde Sterke C, Litchinitser NM, Eggleton BJ. Resonance and scattering in microstructured optical fibers. Optics letters [Internet]. 2002 Nov 15;27(22):1977–9. Available from: http://www.ncbi.nlm.nih.gov/pubmed/18033417

9. Couny F, Benabid F, Roberts PJ, Burnett MT, Maier S a. Identification of Bloch-modes in hollow-core photonic crystal fiber cladding. Optics express [Internet]. 2007 Jan 22;15(2):325–38. Available from: http://www.ncbi.nlm.nih.gov/pubmed/19532248

10. Light PS, Couny F, Wang YY, Wheeler N V, Roberts PJ, Benabid F. Double photonic bandgap hollow-core photonic crystal fiber. Optics express [Internet]. 2009 Aug 31;17(18):16238–43. Available from: http://www.ncbi.nlm.nih.gov/pubmed/19724623

11. Benabid F, Knight JC, Antonopoulos G, Russell PSJ. Stimulated Raman scattering in hydrogen-filled hollow-core photonic crystal fiber. Science (New York, N.Y.) [Internet]. 2002 Oct 11 [cited 2013 Feb 8];298(5592):399–402. Available from: http://www.ncbi.nlm.nih.gov/pubmed/12376698

12. Couny F, Benabid F, Roberts PJ, Light PS, Raymer MG. Generation and photonic guidance of multi-octave optical-frequency combs. Science (New York, N.Y.) [Internet]. 2007 Nov 16 [cited 2013 Feb 11];318(5853):1118–21. Available from: http://www.ncbi.nlm.nih.gov/pubmed/18006741

13. Couny F, Benabid F, Light PS. Large-pitch kagome-structured hollow-core photonic crystal fiber. Optics Letters [Internet]. Optical Society of America; 2006;31(24):3574–6. Available from: http://opus.bath.ac.uk/8787/

14. Couny F, Benabid F, Roberts PJ, Light PS, Raymer MG. Generation and photonic guidance of multi-octave optical-frequency combs. Science [Internet]. 2007;318(5853):1118–21. Available from: http://opus.bath.ac.uk/8665/

15. Benabid F. Hollow-core photonic bandgap fibre: new light guidance for new science and technology. Philosophical transactions. Series A, Mathematical, physical, and engineering sciences [Internet]. 2006 Dec 15 [cited 2013 Jan 29];364(1849):3439–62. Available from: http://www.ncbi.nlm.nih.gov/pubmed/17090469

16. Vahala KJ. Optical microcavities. Nature [Internet]. 2003 Aug 14;424(6950):839–46. Available from:

http://www.pubmedcentral.nih.gov/articlerender.fcgi?artid=3076881&tool=pmcentrez&rendertype=abstract

17. Monroe C. Quantum information processing with atoms and photons. Nature [Internet]. 2002 Mar 14;416(6877):238–46. Available from: http://www.ncbi.nlm.nih.gov/pubmed/11894108

18. Venkataraman V, Saha K, Londero P, Gaeta AL. Few-Photon All-Optical Modulation in a Photonic Band-Gap Fiber. Physical Review Letters [Internet]. 2011 Nov [cited 2013 Feb 19];107(19):193902. Available from: http://link.aps.org/doi/10.1103/PhysRevLett.107.193902

19. Light PS, Benabid F, Couny F, Maric M, Luiten a N. Electromagnetically induced transparency in Rb-filled coated hollow-core photonic crystal fiber. Optics letters [Internet]. 2007 May 15;32(10):1323–5. Available from: http://www.ncbi.nlm.nih.gov/pubmed/17440575

20. Knabe K, Wu S, Lim J, Tillman K a, Light PS, Couny F, et al. 10 kHz accuracy of an optical frequency reference based on (12)C2H2-filled large-core kagome photonic crystal fibers. Optics express [Internet]. 2009 Aug 31;17(18):16017–26. Available from: http://www.ncbi.nlm.nih.gov/pubmed/19724600

21. Wang C, Wheeler N V, Fourcade-dutin C, Grogan M, Bradley TD, Washburn BR, et al. Acetylene frequency references in gas-filled hollow optical fiber and photonic microcells. Applied optics. 2013;52(22):5430–9.

22. Wheeler N V, Light PS, Couny F, Benabid F. Slow and Superluminal Light Pulses Via EIT in a. Journal of Lightwave Technology. 2010;28(6):870–5.

Chapter 3

Photonic Bandgap Hollow Core Photonic Crystal Fibre Fabrication and Characterisation

In this chapter state of the art development of photonic bandgap guiding hollow core photonic crystal fibres (HC-PCF) for atomic vapour loading applications are presented, where record losses have been achieved.

These results include the development of 7 and 19 cell core defect photonic bandgap HC-PCF for guidance at 780 nm. Double photonic bandgap HC-PCF is reported whereby for the first time both bandgaps have been shifted to 800 nm and 1 µm respectively.

3.1 Introduction

The idea of single particle light matter interactions (1–4) was briefly touched on in chapter 2, whereby the interaction strength is increased by decreasing the modal volume. Photonic bandgap (PBG) guiding HC-PCF offers a potential platform for single particle interactions in an all fibre system because of the small transverse diameter and long interaction lengths which are achievable (5). To date commercially available PBG HC-PCF has been used for Rb vapour loading applications at low power levels (6–8). In this chapter, three different PBG guiding HC-PCF's which have been fabricated by the author are presented which include low loss 7 and 19 cell core defect PBG HC-PCF where small core diameters (small modal volume), low optical attenuation and single mode guidance have been achieved. In the final section developments in DPBG HC-PCF are presented where the fibre structure has been engineered to exhibit two bandgaps with central

wavelengths at 800 nm and 1064 nm respectively, which is desired for applications where red detuned lasers are required (9).

3.2 Low Loss 7 cell core defect Photonic Bandgap (PBG) HC-PCF for Rubidium Loading

A PBG HC-PCF with a 7 cell core defect is shown in the optical micrograph (upper panel Fig (3-1) a) which has a hollow core diameter ~ 5 µm and a five ring cladding structure with a pitch ~ 1.7 µm. The reconstructed near-field mode profile (lower panel Fig (3-1) a) is recorded at 780.24 nm when an external cavity diode laser (ECDL) with narrow linewidth (~ 1 MHz) is coupled through a 10 m length sample of the HC-PCF. The mode profile (Fig (3-1) a) recorded using a 60× microscope objective is Gaussian like but additional light can be observed in the cladding structure surrounding the hollow core. It is possible to define the beam quality at the fibre output through the M squared parameter, where M squared is a measure of the fibre output mode relative to that of an idealised TEM_{00} mode with a perfect Gaussian distribution (10) (i.e. $M^2 \geq 1$). The M squared of the output mode is measured at ~ 1.8 using a wavefront sensor to measure the near-field intensity and phase profiles simultaneously. For a fibre such as a HC-PCF which can support more than a single mode a more rigorous measurement of the beam quality is an S squared measurement (11). An S squared measurement identifies both the relative power of the different propagating modes relative to the fundamental and the spatial mode field distribution, giving a more comprehensive description of the output fibre beam quality. The PBG transmission and optical attenuation are measured by cutback method using a 50 W tungsten bulb white light source and optical spectrum analyser. The transmission through 20 m and 10 m sections are shown in Fig (3-1) b), the presence of surface modes (12–14) within the bandgap can be observed at the long wavelength edge of the PBG. The corresponding optical loss (Fig (3-1) c) reaches a low value ~ 230 dB/km at 780 nm.

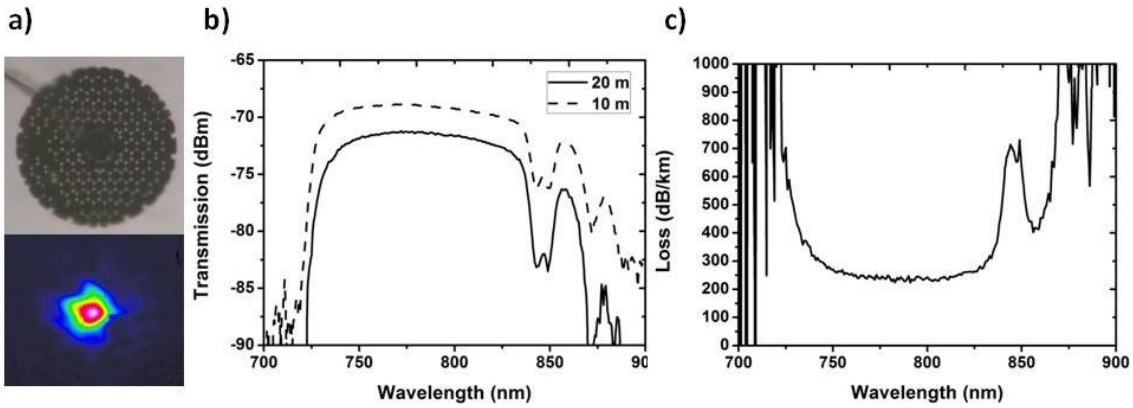

Figure (3-1) a) Optical micrograph of 7 cell PBG HC-PCF (Top) and near-field optical mode profile (lower), b) Transmission spectra of 7 cell PBG HC-PCF through 20 m and 10 m respectively, c) Transmission loss of 7 cell PBG HC-PCF measured by optical cutback technique.

The level of attenuation achieved in this HC-PCF does not represent a state of the art development but is comparable with previous PBG HC-PCF fabricated for guidance around 800 nm (15,16). In addition the small mode area and single mode operation make this HC-PCF a possible platform for single particle interactions.

3.3 Low Loss 19 cell core defect Photonic Bandgap (PBG) HC-PCF for Rubidium Loading

In addition to the 7 cell core defect PBG HC-PCF reported in section 3.2 here a 19 cell core defect PBG HC-PCF (upper panel Fig (3-2) a) is reported. The fabrication of this fibre is under taken because the ultimate attenuation in HC-PCF to date (17,18) has been reported in 19 cell core defect HC-PCF because of the decreased impact of the surface capillary wave roughness (18) of the fibre core surround. The fabricated HC-PCF structure shown in the optical micrograph (Fig (3-2) a) has a 19 cell core defect with diameter ~ 7.5 µm (19). The photonic crystal cladding structure comprises 5 rings with a cladding pitch ~ 1.7 µm. The reconstructed near-field is recorded (lower panel Fig (3-2) a) using a 60× microscope objective and a CCD array when a narrow linewidth (~ 1 MHz) ECDL is coupled through a 10 m sample of the HC-PCF. The output near-field appears close to single mode (Fig (3-2) a) but there is obvious residual light residing in the silica cladding interface (i.e. a surface

mode). The M squared value of the output mode is measured at ~ 1.7.

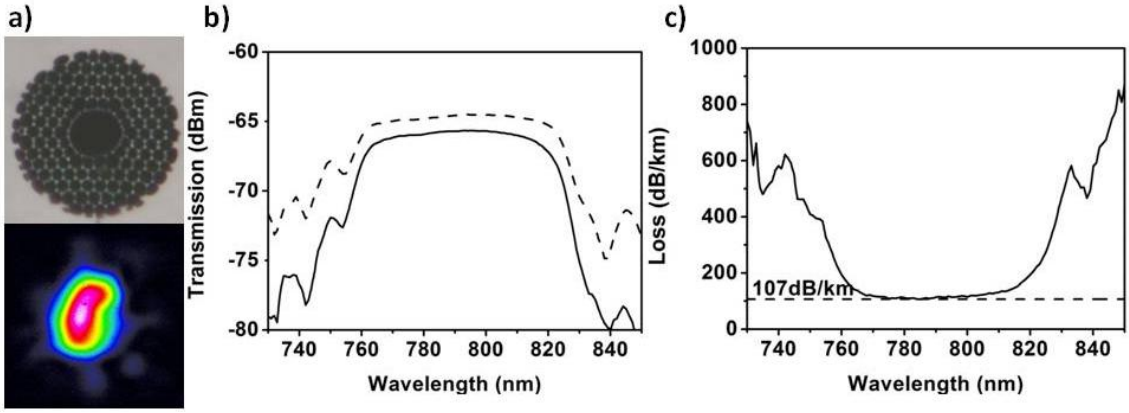

Figure (3-2) a) Optical micrograph and reconstructed near-field mode profile of PBG HC-PCF fabricated for guidance at 780nm, b) Optical transmission through 20m (black solid) and 10m (black dashed) of HC-PCF, c) Loss of HC-PCF as measured by optical cut back method

The optical transmission (Fig (3-2) b) and attenuation (Fig (3-2) c) were measured via cutback technique in a 20 m length of fibre (cutback to 10 m for the attenuation measurement). The HC-PCF transmission (Fig (3-2) b) appears uniform in the centre of the bandgap region with surface modes appearing at both short and long wavelength edges. However the near-field optical mode profile (Fig (3-2) a) shows residual light in the core cladding interface which does not appear in the transmission spectrum. The optical bandwidth in the central uniform region of the PBG is only 38 THz which is extremely narrow, this does not allow for atomic manipulation using a far off red detuned laser source such as in ref (9). However despite the limited optical bandwidth of this fibre the optical attenuation (Fig (3-2) c) in the central PBG region reaches an extremely low ~ 107 dB/km at 785 nm. Remarkably this loss level extends across nearly the full 38 THz of the uniform PBG region. This low loss is typically half of what has been achieved in commercially available PBG HC-PCF and is to the best of my knowledge the lowest optical attenuation reported at this wavelength in any PBG HC-PCF. Prior results for low loss PBG HC-PCF have been reported for Ti:Sapphire laser pulse delivery with a range of attenuations achieved from 125 dB/km to 270 dB/km at 800 nm (15,16,20). Comparison with the 7 cell core defect from section 3.2 shows remarkable reduction in attenuation due to the reduced impact of frozen surface capillary waves which causes surface roughness at the core cladding interface and act as a source of loss (18). However there is a reduction of optical bandwidth when compared with the 7 cell core defect fibre, however as the target wavelength of choice for the atomic D1

and D2 (780 nm & 795 nm respectively) transitions of $^{87/85}$Rb are centrally located this reduction is inconsequential.

This 19 cell core defect PBG HC-PCF has potential applications for single particle interactions despite its slightly increased core diameter compared to the 7 cell core defect of section 3.2. This potential stems from the relatively small core diameter ~ 7.5 µm for small modal volume but with single mode operation and extremely low optical attenuation, ~ 107 dB/km. The reduced optical loss stems from the 19 cell core defect design which is larger than those obtained with 7-cell PBG HC-PCF.

3.4 Double photonic bandgap (DPBG) HC-PCF for Rubidium Loading

Double photonic bandgap (DPBG) HC-PCF reported previously by Light *et al.* (21) was a proof of principle demonstration that engineering the photonic crystal cladding structure would allow a secondary bandgap to be opened at higher normalised frequency. However in ref (21) the primary and secondary bandgaps are located at 1550 nm and 1064 nm respectively, which are not coincident with atomic transitions (e.g. Rb at 780 nm, Cs at 852 nm). As such both bandgaps must be shifted to shorter wavelength pairs such as 1064 nm and 800 nm. This would allow for on resonant probing of atomic transitions combined with off resonant red detuned laser loading (9), and potentially cooling and trapping (22). This shift in PBG wavelength requires a simple scaling of the cladding pitch to smaller values than in ref (21), however this becomes challenging when working with a high air filling fraction structure such as DPBG HC-PCF where the air filling fraction is typically > 97%.

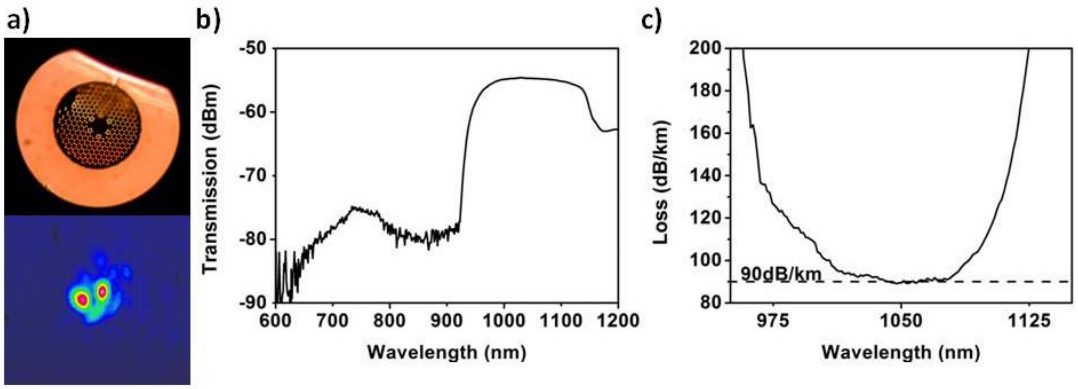

Figure (3-3) a) Optical micrograph and near-field mode profile at 780 nm of DPBG HC-PCF, b) Optical Transmission through 5m of HC-PCF, c) Optical loss of DPBG HC-PCF

An example of a DPBG HC-PCF for operation at 780 nm and 1064 nm is shown in the optical micrograph (Fig (3-4) a). This DPBG HC-PCF has a core diameter which is larger than the 19 cell core defect HC-PCF in section 3.3 with a core diameter ~ 11.3 µm. The photonic crystal cladding structure consists of six rings but with high air filling fraction and cladding pitch ~ 3.4 µm. The cladding pitch has slight variation across the entire structure from ~ 3.3 µm to ~ 3.6 µm. The optical transmission of the DPBG HC-PCF are measured by cutback method using a 50 W tungsten bulb white light source and an OSA on a 25 m sample cutback to 5 m. Transmission through a 5 m sample of the DPBG HC-PCF can be seen in Fig (3-4) b) where strong transmission can be observed in the primary bandgap centred at 1050 nm. However the secondary bandgap located at ~ 750 nm is 30 dBm weaker than the primary bandgap as such only trace evidence of the second bandgap can be observed. The primary PBG located at 1050 nm has a minimum attenuation ~ 90 dB/km (Fig (3-4) c) which is comparable to what can be routinely achieved in a traditional PBG HC-PCF at 1 µm (18,23). The optical attenuation in the secondary bandgap is ~ 2 dB/m at 780 nm which is much greater than the attenuation of the PBG fibres reported earlier in this chapter. The weak guidance of the secondary bandgap primarily results from the reduced air filling fraction of the fabricated fibre compared to what was achieved in (21). The slight non uniformity of the photonic crystal cladding stems from the lack of suitable pressurisation during the fabrication process. Study of the near-field mode profile when a narrow linewidth (~ 1 MHz) ECDL operating at 780 nm is coupled through a 1 m sample of DPBG HC-PCF reveals that the secondary bandgap guides a high order mode (lower panel Fig (3-4) a). The M squared of the near-field mode profile (lower panel Fig (3-4) a) is estimated to be ~ 3.2. Future direction will focus on achieving a higher air filling fraction than has been achieved to date by utilising a greater independent pressurisation in the cladding region. This should allow the secondary bandgap to be opened up fully and hence guide a fundamental air core mode at 780 nm.

The characteristic properties such as optical loss, M squared, optical bandwidth and mode field diameter of the three different PBG HC-PCF reported in this chapter are summarised in table (3-1). Table (3-1) allows direct comparison of the crucial optical parameters when selecting a PBG fibre for a particular application. The immediate conclusion from table (3-1) is that DPBG HC-PCF requires serious

optimisation of the second guidance band centred at 780 nm if it is ever to compete as a viable option with the traditional PBG HC-PCF.

Table (3-1) Comparison of relative HC-PCF parameters for the HC-PCF reported in chapter 3. *All M Squared measurements are taken using a Phasics SID4 wavefront sensor when a narrow linewidth (~1 MHz) ECDL is coupled through the HC-PCF under test.

HC-PCF Type	Loss (dB/km)	M Squared	Bandwidth (nm)	MFD (μm)
7 cell PBG	230	1.8	~100	3.9
19 cell PBG	107	1.7	~60	5.9
DPBG	~2000 @ 780 nm 90 @ 1064 nm	3.2	~50 @ 780 nm ~100 @ 1050 nm	8.9

3.5 Summary

The small core diameter of PBG HC-PCF (i.e. tightly confined modal volume) could find potential application in single particle interactions. This potential requires that small core diameter PBG HC-PCF with guidance bands operating around atomic transitions such as those of Rb or Cs be fabricated. In this chapter both a 7 and 19 cell core defect PBG HC-PCF with guidance bands optimised for 780 nm have been fabricated and characterised. The 7 cell core defect PBG HC-PCF has an extremely small core diameter and single mode guidance. However the transmission loss is ~ 230 dB/km at 780 nm. In addition the fibre supports a reasonable fraction of light in the core cladding interface at 780 nm which is undesirable as this acts as a source of loss and undesirable nonlinear effects. The 19 cell core defect reported here has record low loss of ~ 107 dB/km at 785 nm which to the best of my knowledge is the lowest optical attenuation reported at this wavelength in any PBG HC-PCF. The PBG HC-PCF has an extremely flat uniform transmission spectrum with single mode guidance at the expense of slightly large core diameter compared to the 7 cell core defect PBG HC-PCF. Finally DPBG HC-PCF is reported where the guidance bands have been shifted compared to that previously reported. This DPBG HC-PCF has potential as it would allow off resonance manipulation of atoms and on resonance probing of atomic transitions in a single fibre with small core dimensions. The DPBG HC-PCF reported here demonstrates two bandgaps in the desired spectral regions, however while the first bandgap demonstrates optical attenuation of ~ 90 dB/km at 1050 nm the secondary bandgap has not been fully opened. As such this PBG only guides a high order mode because a high enough air filling fraction was not achieved during the fabrication process. This will be rectified in future work

by optimising the draw parameters to obtain a suitable air filling fraction and open the second PBG fully to guide a fundamental core mode at 780 nm.

Future development of PBG HC-PCF will focus on achieving lower losses in both 7 and 19 cell core defect design HC-PCF. Additionally the optical bandwidth could be optimised and the presence of surface modes within the bandgap could be addressed by implementing schemes such as those in (13). Finally the existing fibres will be utilised in Rb vapour loading experiments for low light power optical interactions, where the extremely small core diameter will be beneficial.

References

1. Vahala KJ. Optical microcavities. Nature [Internet]. 2003 Aug 14;424(6950):839–46. Available from: http://www.pubmedcentral.nih.gov/articlerender.fcgi?artid=3076881&tool=pmcentrez&rendertype=abstract

2. Monroe C. Quantum information processing with atoms and photons. Nature [Internet]. 2002 Mar 14;416(6877):238–46. Available from: http://www.ncbi.nlm.nih.gov/pubmed/11894108

3. Mabuchi H, Doherty a C. Cavity quantum electrodynamics: coherence in context. Science (New York, N.Y.) [Internet]. 2002 Nov 15 [cited 2013 Aug 16];298(5597):1372–7. Available from: http://www.ncbi.nlm.nih.gov/pubmed/12434052

4. Walther H, Varcoe BTH, Englert B-G, Becker T. Cavity quantum electrodynamics. IOP Publishing: Reports on Progress in Physics [Internet]. 2006 May 1 [cited 2013 Aug 8];69(5):1325–82. Available from: http://stacks.iop.org/0034-4885/69/i=5/a=R02?key=crossref.2e5c0e61d04e1066e39543161ec7a7c4

5. Benabid F, Knight JC, Antonopoulos G, Russell PSJ. Stimulated Raman scattering in hydrogen-filled hollow-core photonic crystal fiber. Science (New York, N.Y.) [Internet]. 2002 Oct 11 [cited 2013 May 22];298(5592):399–402. Available from: http://www.ncbi.nlm.nih.gov/pubmed/12376698

6. Ghosh S, Bhagwat A, Renshaw C, Goh S, Gaeta A, Kirby B. Low-Light-Level Optical Interactions with Rubidium Vapor in a Photonic Band-Gap Fiber. Physical Review Letters [Internet]. 2006 Jul [cited 2013 Feb 13];97(2):023603. Available from: http://link.aps.org/doi/10.1103/PhysRevLett.97.023603

7. Venkataraman V, Saha K, Londero P, Gaeta AL. Few-Photon All-Optical Modulation in a Photonic Band-Gap Fiber. Physical Review Letters [Internet]. 2011 Nov [cited 2013 Feb 19];107(19):193902. Available from: http://link.aps.org/doi/10.1103/PhysRevLett.107.193902

8. Londero P, Venkataraman V, Bhagwat A, Slepkov A, Gaeta A. Ultralow-Power Four-Wave Mixing with Rb in a Hollow-Core Photonic Band-Gap Fiber. Physical Review Letters [Internet]. 2009 Jul [cited 2013 Feb 25];103(4):043602. Available from: http://link.aps.org/doi/10.1103/PhysRevLett.103.043602

9. Vorrath S, Möller S a, Windpassinger P, Bongs K, Sengstock K. Efficient guiding of cold atoms through a photonic band gap fiber. New Journal of Physics [Internet]. 2010 Dec 9 [cited 2013 Feb 14];12(12):123015. Available from: http://stacks.iop.org/1367-2630/12/i=12/a=123015?key=crossref.fef11793f31fc43564898ca281f561d8

10. Siegman AE. Defining, measuring, and optimizing laser beam quality. SPIE Vol 1868. 1993. p. 1– 12.

11. Nicholson JW, Yablon a D, Ramachandran S, Ghalmi S. Spatially and spectrally resolved imaging of modal content in large-mode-area fibers. Optics express [Internet]. 2008 May 12;16(10):7233–43. Available from: http://www.ncbi.nlm.nih.gov/pubmed/18545428

12. West J, Smith C, Borrelli N, Allan D, Koch K. Surface modes in air-core photonic band-gap fibers. Optics express [Internet]. 2004 Apr 19;12(8):1485–96. Available from: http://www.ncbi.nlm.nih.gov/pubmed/19474974

13. Amezcua-Correa R, Broderick NG, Petrovich MN, Poletti F, Richardson DJ. Optimizing the usable bandwidth and loss through core design in realistic hollow-core photonic bandgap fibers. Optics express [Internet]. 2006 Aug 21;14(17):7974–85. Available from: http://www.ncbi.nlm.nih.gov/pubmed/19551052

14. Amezcua-Correa R, Gèrôme F, Leon-Saval SG, Broderick NGR, Birks T a, Knight JC. Control of surface modes in low loss hollow-core photonic bandgap fibers. Optics express [Internet]. 2008 Jan 21;16(2):1142–9. Available from: http://www.ncbi.nlm.nih.gov/pubmed/18542188

15. Luan F, Knight JC, Russell PSJ. Femtosecond soliton pulse delivery at 800nm wavelength in hollow-core photonic bandgap fibers. 2004;12(5):4–9.

16. Bouwmans G, Luan F, Knight J, St J Russell P, Farr L, Mangan B, et al. Properties of a hollow-core photonic bandgap fiber at 850 nm wavelength. Optics express [Internet]. 2003 Jul 14;11(14):1613–20. Available from: http://www.ncbi.nlm.nih.gov/pubmed/19466039

17. Mangan BJ, Farr L, Langford A, Roberts PJ, Williams DP, Couny F, et al. Low loss (1 . 7 dB / km) hollow core photonic bandgap fiber. 2004;19–21.

18. Roberts P, Couny F, Sabert H, Mangan B, Williams D, Farr L, et al. Ultimate low loss of hollow-core photonic crystal fibres. Optics express [Internet]. 2005 Jan 10;13(1):236–44. Available from: http://www.ncbi.nlm.nih.gov/pubmed/19488348

19. Bradley TD, Wang YY, M A, Fourcade Dutin C, Mangan BJ, Wheeler N V, et al. Progress in hollow core photonic crystal fiber for atomic vapour based coherent optics. Proc. SPIE 8273, Advances in Slow and Fast Light V, 82730. 2012.

20. Welch MG, Cook K, Correa RA, Gérôme F, Wadsworth WJ, Gorbach A V, et al. Solitons in Hollow Core Photonic Crystal Fiber : Engineering Nonlinearity and Compressing Pulses. 2009;27(11):1644–52.

21. Light PS, Couny F, Wang YY, Wheeler N V, Roberts PJ, Benabid F. Double photonic bandgap hollow-core photonic crystal fiber. Optics express [Internet]. 2009 Aug 31;17(18):16238–43. Available from: http://www.ncbi.nlm.nih.gov/pubmed/19724623

22. Miller, J D Cline, R A and Heinzen DJ. Far-off-resonance optical trapping of atoms. Physical Review A. 1993;47(6).

23. Humbert G, Knight J, Bouwmans G, Russell P, Williams D, Roberts P, et al. Hollow core photonic crystal fibers for beam delivery. Optics express [Internet]. 2004 Apr 19;12(8):1477–84. Available from: http://www.ncbi.nlm.nih.gov/pubmed/19474973

Chapter 4

Enhanced Inhibited Coupling Kagome Hollow Core Photonic Crystal Fibre

In this chapter state of the art development of Kagome lattice inhibited coupling (IC) hollow core photonic crystal fibre (HC-PCF) is presented where record loss has been achieved. The low loss Kagome HC-PCF is used to investigate the IC guidance mechanism, specifically the bending loss mechanism in IC guiding Kagome HC-PCF is investigated. The effect of the number of cladding rings upon the confinement and bending loss is investigated experimentally and supported with theoretical modelling. Finally optimisation of the hypocycloidal core shape and its effect upon the confinement loss in IC guidance Kagome HC-PCF is presented.

4.1 Enhanced Inhibited Coupling in Hypocycloid core shape Kagome HC-PCF[1]

The guidance mechanism of inhibited coupling relies upon low spatial overlap and strong transverse phase mismatch between the core mode (zero order Bessel function) and fast oscillating cladding modes associated with high azimuthal number (red circles overlapping the core contour in Fig (4-1) a) & b) as discussed in chapter 2 and depicted in Fig (4-1) a) (1). Recent developments of hypocycloid core shape Kagome HC-PCF (2–4) have recorded extremely low losses in the infrared telecommunications band. The intuitive differences between the traditional circular core shape Kagome HC-PCF and hypocycloid core shape (i.e. negative curvature) Kagome HC-PCF are highlighted in Fig (4-1) a) and b).

[1] This work is reported in T D Bradley *et al.* JLWT, 31 (16), 2013, (12)

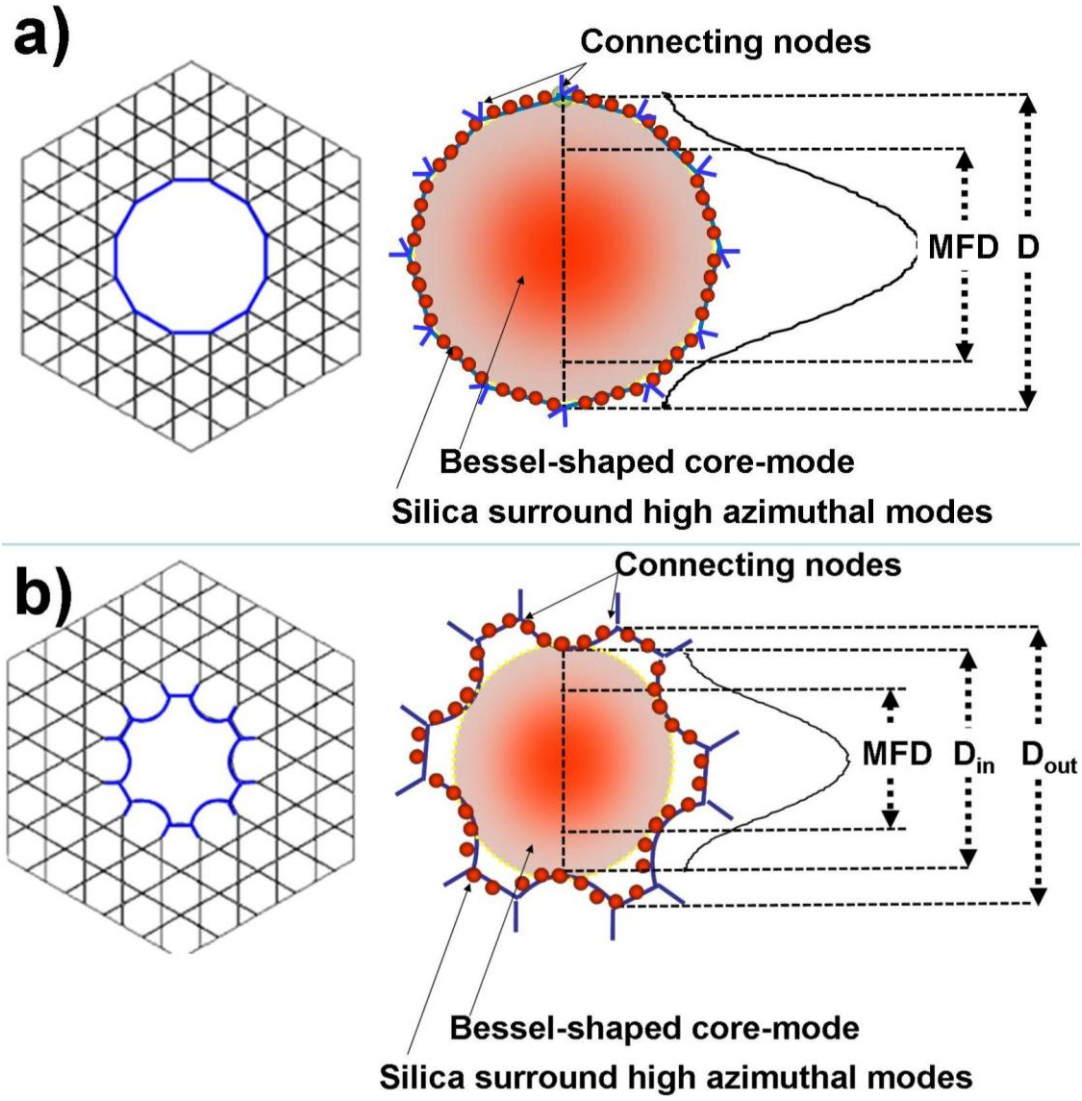

Figure (4-1) a) (from left to right) Idealised Kagome structure of traditional Kagome HC-PCF, Optical mode of core and overlap with low azimuthal number cladding modes, and 2D profile distribution of core mode showing mode field diameter relative to core boundary, b) Idealised Kagome structure of Hypocycloidal Kagome HC-PCF, Optical mode of core and overlap with low azimuthal number cladding modes, and 2D profile distribution of core mode showing mode field diameter relative to core boundary.

In a traditional circular core shape Kagome HC-PCF (Fig (4-1) a) the core mode field (zero order Bessel function) interacts with the entirety of the silica core surround where the mode field diameter is related to the physical core size by the approximate relationship $R_{MFD} \sim (\pi/4)R_{core}$, where R_{core} is the physical radius of the hollow core. However in hypocycloid core shape (Fig (4-1) b) the mode field (whose diameter is related to the physical core size by $R_{MFD} \sim (\pi/4)R_{ID}$, where R_{ID} is the small circle which is tangential to the inner most cusps) only intersects the tangential section of the inner most cusps, thus reducing the spatial overlap between the core and cladding modes. Additionally in the hypocycloid core contour design (Fig (4-1)

b) the silica nodes which connect the core to the cladding structure and support low azimuthal number cladding modes (i.e. enhanced coupling with the core mode and increased optical loss) are spatially located further from the core mode thus drastically reducing the spatial overlap and hence the loss. This rationale has been corroborated by other works following the seminal results of Wang *et al.*(2), and whereby they have demonstrated that low losses can be achieved using a hypocycloid core curvature in simplified fibre designs (5–8). The extensive development of hypocycloidal core shape Kagome HC-PCF's in recent years has lead to the definition of the dimensionless parameter b which is used to define the degree of curvature of the hypocycloidal core shape, and which shows in a quantitative manner the impact of the negative curvature on the confinement loss of the fibre (9). The parameter b is defined as $b = d/r$ where d and r are defined in the schematic (Fig (4-2)). Here, we show the development of hypocycloid core Kagome HC-PCF for Rb related application along with reporting the systematic experimental and theoretical study[2] in developing state-of-the-art IC guiding HC-PCF along with understanding the impact of both the negative curvature and the cladding ring number of the transmission performance of this type of HC-PCF (10,11).

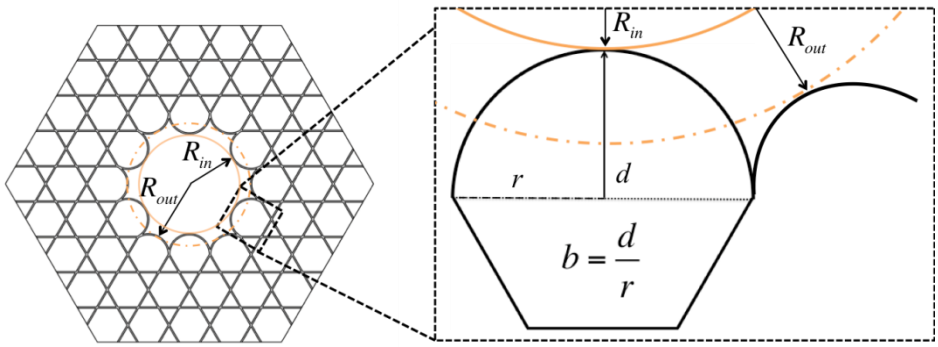

Figure (4-2) Schematic of hypocycloidal core shape Kagome HC-PCF showing how the dimensionless curvature parameter b is defined (10)**.**

[2] The study consists of an extensive campaign of design and fabrication of several HC-PCF and numerical simulations. The author was part of the GPPMM team involved in this study. In particular, the author participated in the fibre fabrication and characterisation which started in 2011.

4.2 Low Loss Enhanced IC Kagome HC-PCF for Rubidium Loading

A hypocycloid core shape Kagome HC-PCF has been fabricated for Rb vapour based applications as shown in the SEM inset of Fig (4-3) b). The core has a hypocycloid core shape with an inner diameter of ~ 33 µm, an outer diameter of ~ 40 µm and a hypocycloid arc curvature parameter, b ~ 0.64. The cladding structure consists of three rings with a cladding pitch of ~ 14 µm and a silica strut thickness, t ~ 320 nm. This fibre was drawn especially to have guidance bands operating in the near infrared and visible guidance regions necessitating a thinner strut thickness and smaller cladding pitch size than those reported previously for infrared guidance (telecommunication band) in (2,3) which typically have cladding pitch sizes of ~ 18 – 20 µm. The scaling of the cladding pitch and strut thickness for operation in the near infrared requires precise control of the fibre draw parameters so as to maintain a balance between the silica surface tension and the viscio-elasticity of the HC-PCF structure and particularly the core cusp curvature which are paramount for strong IC guidance.

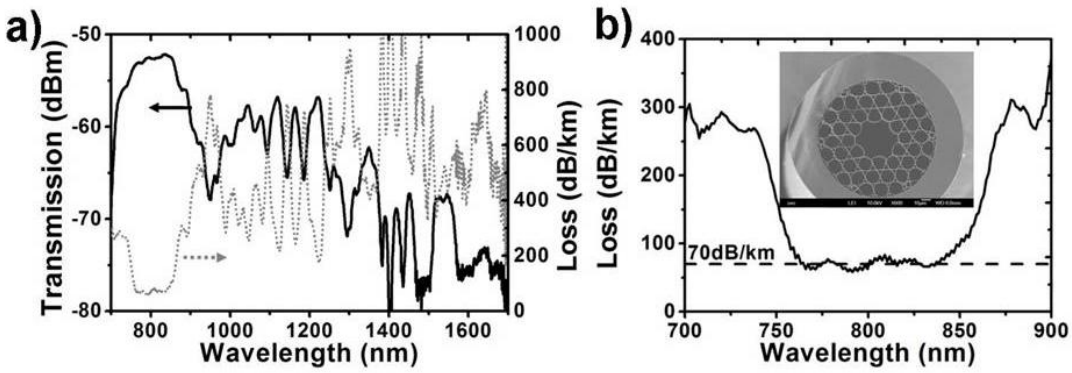

Figure (4-3) a) Transmission (solid black) through 20m of Kagome HC-PCF developed for guidance at 780nm and associated fibre loss (dotted grey) measured by optical cut back method, b) Optical loss of fibre centred at 800nm (Inset: SEM of Kagome HC-PCF) (12).

The optical transmission and attenuation were measured through 20 m of the Kagome HC-PCF (cut back to 10 m for the attenuation measurement shown in Fig (4-3) a) using a 50W tungsten bulb white light source and optical spectrum analyser (OSA). Care was taken to both minimise the impact of the fibre end face cleave and couple light only into the hollow core by aligning using a camera. As expected from a Kagome HC-PCF (1,13) the fabricated Kagome HC-PCF has broadband guidance (solid black curve in Fig (4-3) a) extending from 700 – 1750 nm with a corresponding average optical loss ~ 300 dB/km (dotted grey curve in Fig (4-3) a).

In the spectral region from 750 – 850 nm (Fig (4-3) b) the optical loss reaches a low 70 dB/km in this spectral window which is highly suited for Rb and Cs vapour applications. This is to the best of my knowledge the lowest optical attenuation reported at this wavelength in any HC-PCF and has even lower loss than the 19 cell photonic bandgap (PBG) HC-PCF reported in chapter 3. Remarkably this Kagome HC-PCF has low loss while having 2× larger hollow core than the fibre used in (14) and 8× larger than used in (15) while still retaining single mode operation. This exceptionally low loss is situated exactly around the D1 and D2 absorption line of $^{87/85}$Rb and so makes this fibre extremely desirable for coherent optics in Rb vapour. The broadband guidance allows optically assisted loading of Rb atoms using a far off red detuned laser such as 1064 nm (16). The optical loss of 300 dB/km around 1064 nm is a significant reduction when compared with traditional Kagome HC-PCF losses ~ 1 dB/m (13). While prior work has demonstrated low optical loss of 30 - 40 dB/km at 1550 nm (2,3), < 50 dB/km at 3.39 μm (8) and 34 dB/km in the 3.4 μm range (5), no work has yet been reported of shifting these loss values to the near infra red wavelengths, as reported here.

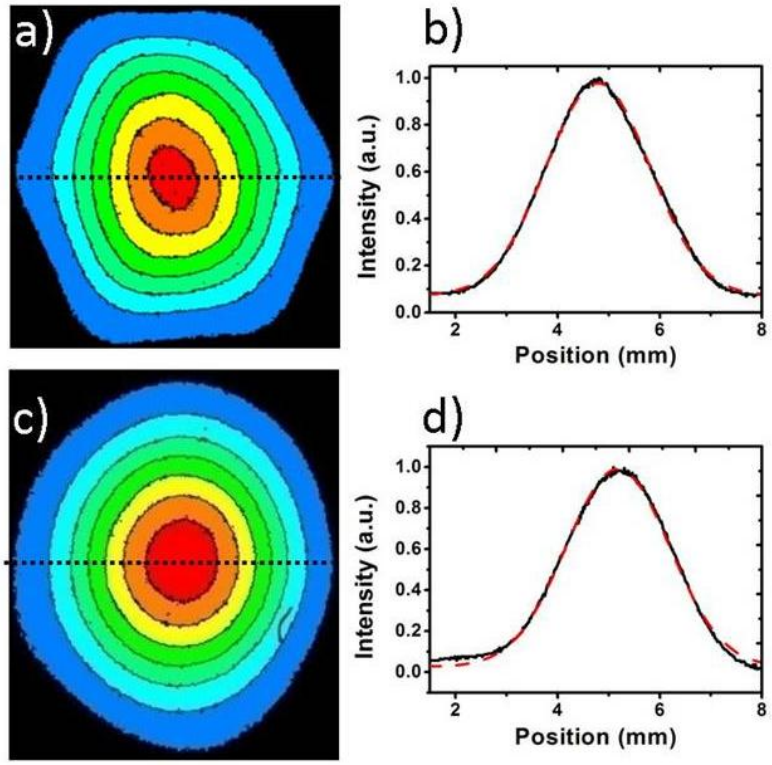

Figure (4-4)a) Reconstructed nearfield of Kagome HC-PCF, b) Slice through nearfield (black) fitted with Gaussian curve (red), c) Optical farfield of Kagome lattice HC-PCF, d) Slice through Optical farfield (black) fitted with Gaussian curve (red) (12)**.**

While the core is significantly larger than the PBG HC-PCF's reported in the previous chapter (chapter 3) the Kagome HC-PCF still demonstrates excellent single mode properties, the reasons for which will be discussed later in the chapter. The near and far field mode profiles are recorded by coupling a narrow linewidth (~ 1 MHz) external cavity diode laser (ECDL) with greater than 90 % coupling efficiency through a 5 m length of the hypocycloid core shape Kagome HC-PCF using a 40× magnification microscope objective and CCD camera. The reconstructed near-field is shown in Fig (4-4) a) and its profile over the dashed line respectively (Fig (4-4) b), which has been fitted to a Gaussian distribution. Likewise the imaged far-field (Fig (4-4) c) and its profile (Fig (4-4) d) show remarkable single mode content. Imaging the near and far-fields at several different positions from the fibre end allows an estimate the M^2 value of the output beam quality. Over the short axis of the hollow core (i.e. chord connecting the two inward most tangential cusps) the $M^2 < 1.1$ while over the hollow core long axis (i.e. chord connecting the two outward most tangential cusps) the $M^2 \sim 1.4$. Hence this Kagome HC-PCF has excellent beam quality at the fibre output.

Following the demonstration of the excellent linear transmission properties of the IC Kagome HC-PCF the bending losses and the bend loss mechanism in IC guiding HC-PCF were investigated using this fibre. Fig (4-5) a) demonstrates the evolution of the bending losses as a function of bend radii as the radius is increased from 5 - 17.5 mm. The HC-PCF demonstrates a 3 dB bend radius of ~ 5 mm which makes this fibre particularly suited to applications such as atomic vapour based compact frequency standard or magnetometer.

Furthermore the bend loss mechanism is investigated and resonant coupling to modes supported in the air holes of the photonic crystal cladding are observed (Fig (4-6) b). In Fig (4-6) the power in the core guided mode is increased above the saturation intensity of the CCD camera so as to observe the coupling to the air hole modes due to the limited dynamic range of the camera. In Fig (4-6) coupling to air hole modes is observed as the bend radius is decreased below ~ 17.5 mm, it is noteworthy that little coupling is observed to the silica strut modes. This is an indication of the "non interaction" between the core mode and fast oscillating cladding modes which demonstrates the strength of the inhibited guidance mechanism.

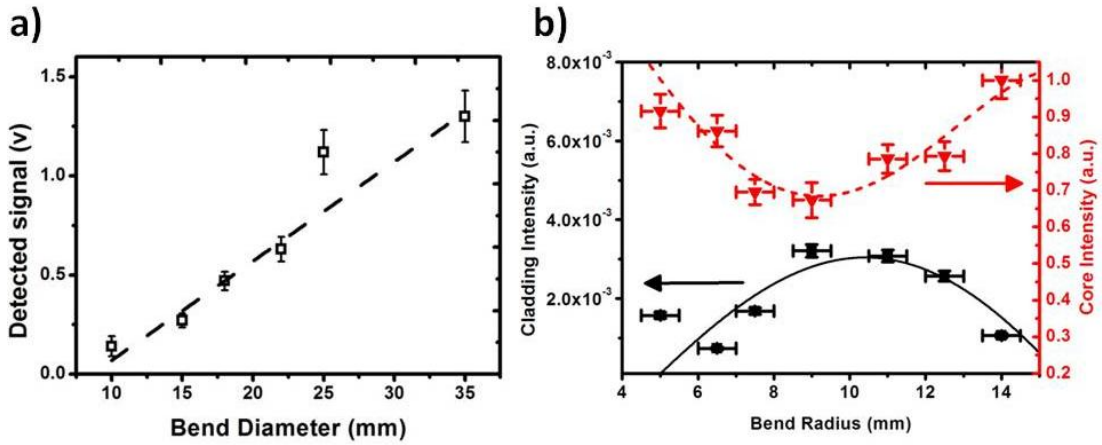

Figure (4-5) a), Detected output power from 5 m Kagome HC-PCF as a function of bending radii, b) Core and cladding air hole mode power fluctuations for different bending radii (12)**.**

The interaction between the core guided mode and the air hole mode can be described through a coupled wave approximation whereby the core and the cladding modes are approximated to those of hollow capillaries (17) with diameters of 17.5 µm and 7 µm respectively. The phase mismatch between the guided modes can then be described by $\Delta\beta = a + b/R_{Bend}^2$, where R_{Bend} is the bend radius, $a = \Delta\beta_o$ is the phase mismatch for straight capillaries and $b = -\frac{1}{6}\left(1-\frac{15}{4u}\right)\left(\frac{n_0 k_0}{u}\right)^2\left(r_{core}^4 - r_{clad}^4\right)$ (18). For the diameters of the core and air hole capillary (17.5 µm and 7 µm respectively) used here the phase matching conditions occurs at a bending radii ~ 8 mm. In Fig (4-5) the power fluctuations in the core and a single cladding air hole are plotted as a function of the bend radii. Maximum power transfer is observed for ~ 9 mm bend radius which is qualitative agreement with the above theoretical model.

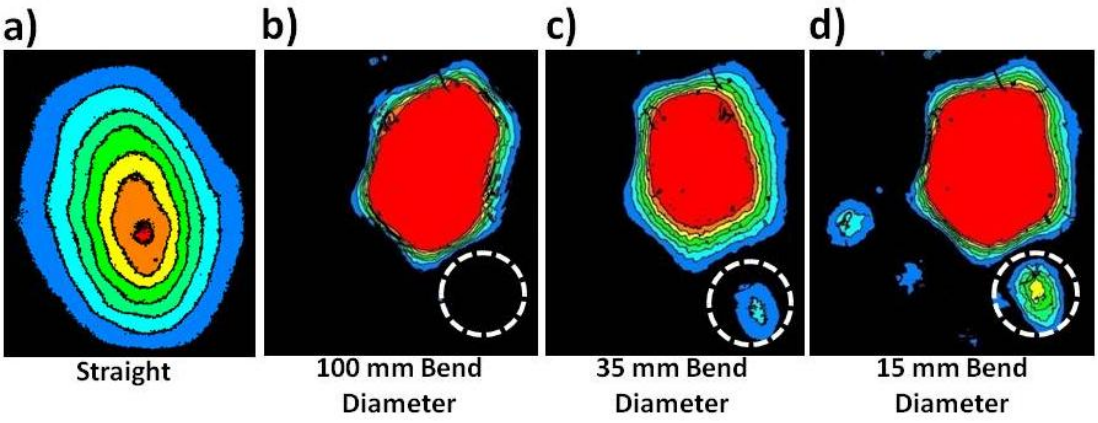

Figure (4-6) (from left to right) Optical mode in the fibre core as at different bending diameters (12)**.**

Figure (4-7) plots the loss of commercially available PBG guiding HC-PCF (red circles) showing ~$1/\lambda^3$ dependence of the attenuation as reported by Roberts *et al.* (19). For comparison the Kagome HC-PCF reported by Wang *et al.* (2) (blue triangle) is plotted, hypocycloid-core shape Kagome fibres now have optical losses comparable to PBG guiding HC-PCF. The PBG guiding and Kagome HC-PCF's fabricated for operation at 780 nm and reported earlier in this chapter and the previous chapter are shown by the red crosses, pink rhombus, green and blue diamond's respectively. It can clearly be observed that these fibres have significantly lower losses than commercially available PBG guiding HC-PCF's. Even more surprising is that the Kagome HC-PCF has lower loss than speciality PBG guiding HC-PCF despite having greater optical bandwidth and 5 times larger hollow core while still retaining single mode operation.

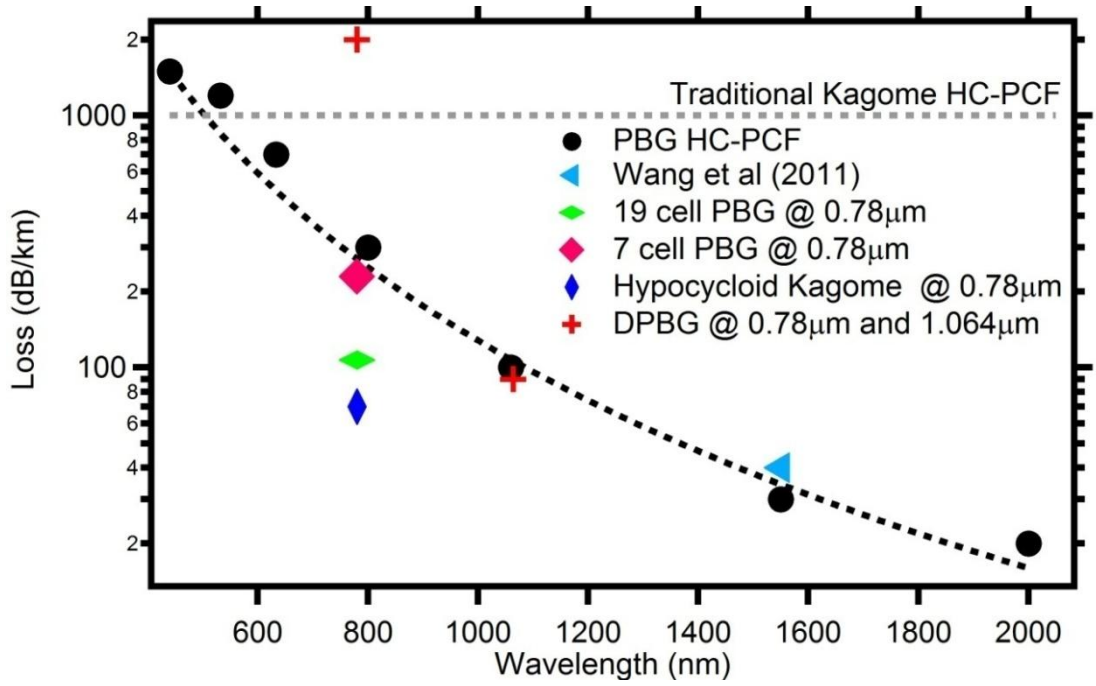

Figure (4-7) Optical loss of PBG (black circles) HC-PCF fitted with $1/\lambda^3$ fit (dashed black line) and traditional Kagome (dashed grey) HC-PCF as a function of wavelength. For comparison the HC-PCF's reported in chapters 3 and 4 are plotted for comparison with what has been previously reported. Low loss hypocycloid Kagome HC-PCF (light blue triangle) reported in (26), low loss of 19 cell (green diamond) and 7 cell (pink rhombus) PBG HC-PCF reported in chapter 3, DPBG HC-PCF (red crosses) from chapter 3 and low loss Kagome HC-PCF (blue diamond)reported here (12)**.**

4.3 Impact of Hypocycloidal Core Shape Curvature on Inhibited Coupling

With the development of hypocycloidal core shape Kagome HC-PCF's and the corresponding reduction in optical attenuation that these fibres present it has now

become necessary to investigate fully the role that the core shape plays in the enhanced IC guidance mechanism. The role of the hypocycloidal curvature, b defined earlier in section 4.1 is investigated both through numerical simulations (all numerical results are finite element method simulations[3]) and experiment (9,10). Numerical simulations of the confinement loss with increasing curvature b are presented in Fig (4-8) a) where the loss drops from ~1000 dB/km for b = 0 to below 1 dB/km for b = 1.5 in the mid infrared spectral region (20). This would mean that Kagome HC-PCF's could become comparable with or better than the lowest loss PBG HC-PCF's.

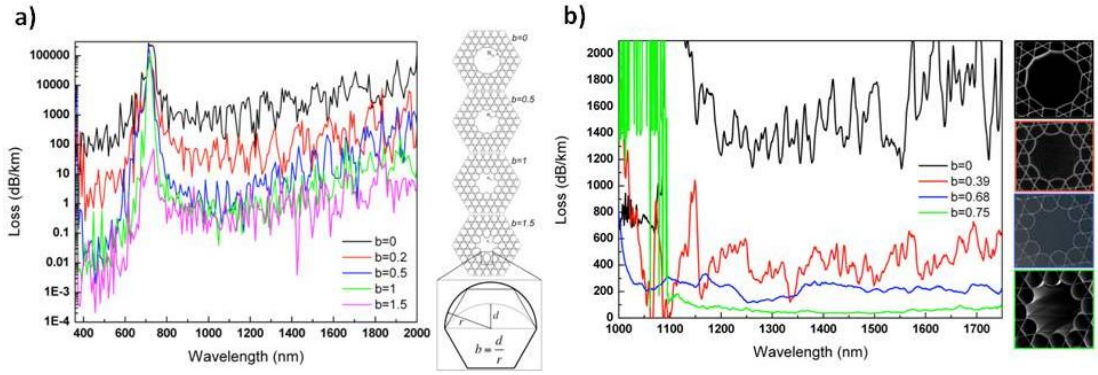

Figure (4-8) a) Numerical simulation of confinement loss spectrum with increasing hypocycloidal curvature, b) Experimental confinement loss spectrum with increasing hypocycloidal curvature (9)

Further more in the visible guidance band the numerical simulations predict that for large hypocycloidal curvatures, b > 1 the confinement loss could be reduced further, to ~ 0.1 dB/km approaching the fundamental attenuation limits of silica single mode fibre (SMF). Such a development would be exciting because hollow core fibres could potentially replace SMF in telecommunications industry because of the lower nonlinearity and dispersion properties. To corroborate this behaviour experimentally several fibres were fabricated with approximately similar pitch ~ 21 µm, strut thickness ~ 350 nm and core diameter ~ 60 µm but with b values ranging from 0 – 0.75 as shown in Fig (4-8) b). Confinement losses reduce from ~1300 dB/km for b = 0 to ~ 40 dB/km for b = 0.75 thus confirming the predicted theoretical trend from the numerical simulations. While 40 dB/km is a dramatic improvement of the loss figure compared with traditional circular Kagome HC-PCF, it was not possible to improve the core curvature above b = 0.75 using this fibre design. This is due to the

[3] The numerical simulations were undertaken in collaboration with the university of Modena (Luca Vincetti group)

rheological difficulties associated with drawing hypocycloidal core shape fibres with large b curvature values and strut thickness ~ 350 nm without adversely altering the photonic crystal cladding structure.

In order to increase the hypocycloidal curvature, b to values closer to 1 a different fibre design was implemented where thicker capillary tubes were used in the stacking process. Numerical simulations (Fig (4-9) a) show that for thicker struts of ~ 1400 nm but with b = 1, the confinement loss can be reduced below 10 dB/km in the spectral region around 1 µm. However simulations (Fig (4-9) a) predict that thinner struts here 800 nm and 350nm with the same curvature value can have lower confinements losses in the 1 µm spectral region. From the numerical simulations several Kagome HC-PCF's with different strut thicknesses of 800 nm and 1400 nm were fabricated with large curvature values of ~ 0.9 and ~ 1 respectively as seen in Fig (4-9) b) and c). Confinement losses have been reduced to 80 dB/km in the first high order transmission band in the Kagome HC-PCF with t ~ 800nm (Fig (4-9) b). The confinement losses have reached a low value of 40 dB/km in the second high order transmission band with a strut thickness ~ 1400 nm (Fig (4-9) c). Currently work is on going to fabricate a Kagome HC-PCF with large curvature. As a preliminary results, it is noteworthy that curvature of, b ~ 1 was achieved and where the optical attenuation has been reduced to ~ 17 dB/km level for guidance around the 1 µm spectral region (10).

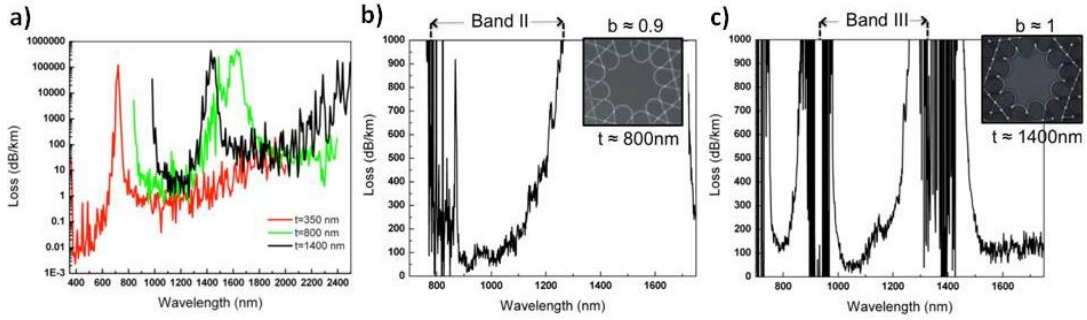

Figure (4-9) a) Numerical simulation of confinement loss spectrum evolution for same curvature but different strut thickness, b) Experimental confinement loss spectrum for Kagome with strut thickness ~800 nm, c) Experimental confinement loss spectrum for Kagome with Kagome with strut thickness ~1400 nm (9)

In addition to the desirable reduction in confinement loss that results from the hypocycloidal geometry, from numerical simulations there are two readily apparent benefits. The first of these is the suppression of high order modes (HOM) as the curvature parameter b is increased above 0.5 (Fig (4-10) a).

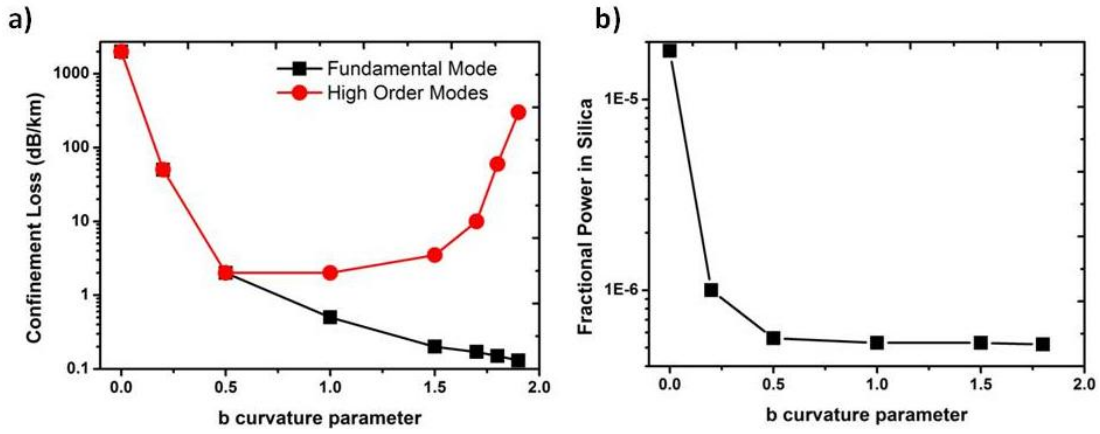

Figure (4-10) a) Evolution of the confinement loss for the fundamental (black squares) and high order modes (red circles) with hypocycloid curvature, b) Evolution of fractional power residing in silica core cladding interface with hypocycloidal curvature. (Simulations performed by Luca Vincetti) (21)

Numerical simulations show rapid reduction in the confinement losses of the fundamental mode (HE11) as b > 0.5 however HOMs experience increasing confinement losses as b > 0.5. Hence the mode quality of high curvature parameter hypocycloid Kagome HC-PCF is improved with increasing curvature. Large core Kagome HC-PCF can now have extremely low loss and excellent mode quality as shown experimentally in section 4.3. Thus creating exciting opportunities for atomic vapour loading applications where all these features are desirable.

The second desirable feature shown by simulations is the reduction in the fractional power overlapping the silica core cladding interface as the b curvature parameter is increased. This reduction increases the power handling abilities of the fibre (21) and reduces any nonlinear effects from the light in the silica core surround. The dramatic reduction in the fractional power in silica with increasing curvature can be simply explained as the optical mode only interacts with the inward most cusps of the hypocycloid. Greater curvature reduces this interaction length hence reducing the overlap integral.

4.4 Cladding Ring Effect on Loss of IC Kagome HC-PCF

In addition to the study of hypocycloidal core curvature and its effect on reducing the confinement loss of Kagome HC-PCF an additional complimentary investigation has been undertaken into the effect of the photonic crystal cladding on the IC guidance mechanism (11,22). A numerical and experimental investigation into the effect of the number of cladding rings was under taken to investigate the effects on the confinement and bending losses.

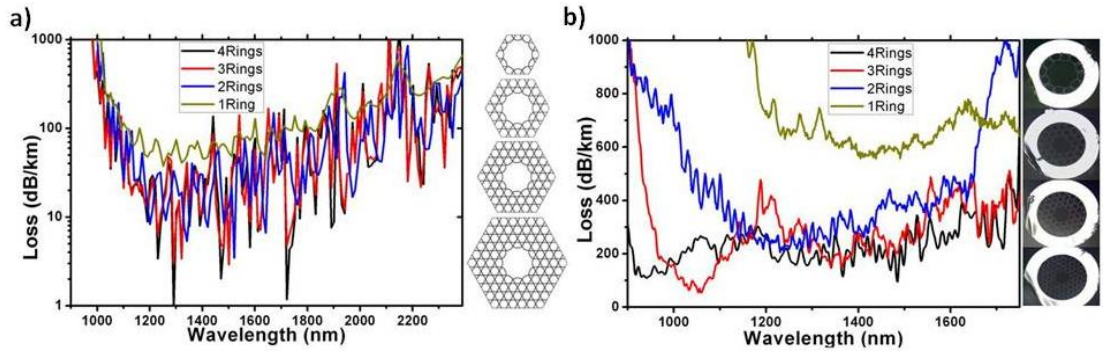

Figure (4-11) a) Numerical simulation of confinement loss evolution with increasing number of cladding rings, b) Experimental spectrum of confinement loss evolution with increasing number of cladding rings (22)**.**

The confinement loss is investigated numerically (Fig (4-11) a) as a function of the number of cladding rings. Decreased confinement loss can be observed for 2-4 ring cladding fibres compared to a single ring cladding structure. This is confirmed experimentally by fabricating four different fibres with different numbers of cladding rings but with approximately the same cladding pitch ~ 20 µm, core diameter ~ 60 µm and hypocycloidal core curvature, b ~ 0.6. Confinement losses (Fig (4-11) b) of ~ 600 dB/km are observed in a single cladding ring structure where as the losses of ~ 200 dB/km are observed for fibres with greater than 2 cladding rings. For fibre structures with greater than a single layer of cladding structure little variation is observed both numerically and experimentally in the confinement loss.

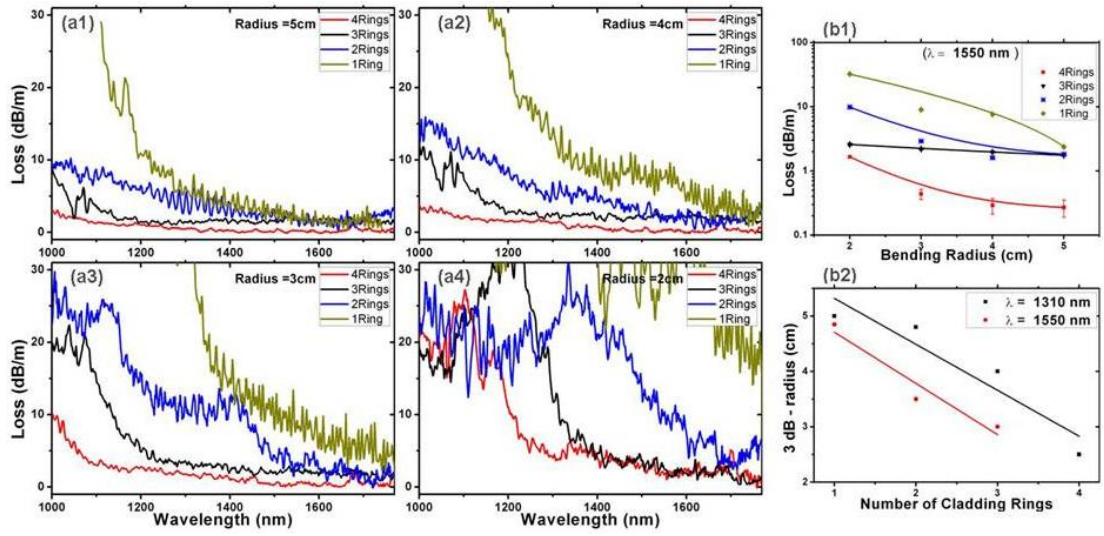

Figure (4-12) a1-a4) Bend loss spectrum for different number of cladding rings with decreasing bend radii, b1) Bend loss evolution for different numbers of cladding rings, b2) 3dB Bend radius evolution versus number of cladding rings (22)**.**

The bend loss is investigated in different number of cladding rings fibres. The bend loss evolution for different number of cladding ring fibres were investigated for

bending radii varying from 5 – 2 cm shown in Fig (4-12) a1) to a4). Bending induced losses are clearly greater for Kagome HC-PCF's with fewer cladding rings at all bending radii as summarised in Fig (4-12) b1) at 1550 nm. The 3 dB bend radius for different numbers of cladding rings is shown in Fig (4-12) b2) for two wavelengths. It can clearly be seen that the 3 dB bend radius linearly decreases as the number of cladding rings increases.

When the number of cladding rings is increased above 2 the decrease of the confinement loss is minimal. However for applications where Kagome HC-PCF may have to undergo significant bending then larger number of cladding rings dramatically reduces the amount of bend induced loss which is observed.

4.5 Comparison of PBG and IC HC-PCF

In this section, the four different HC-PCF's reported in chapter 3 and 4 are summarised and compared. Table (4-1) summarises the properties of the 3 PBG HC-PCF's from the previous chapter and the enhanced inhibited coupling Kagome HC-PCF from this chapter. Four key characteristics of HC-PCF performance are presented in table (4-1) these are optical loss, M squared, optical bandwidth and mode field diameter (MFD). Depending on the specific atomic vapour performance that is being targeted then it is necessary to carefully select the correct HC-PCF for the application. Several HC-PCF with extremely low optical attenuations are now available for Rb vapour based applications with a MFD varying from ~ 4 µm to ~ 24 µm. Depending on the specific application a wide variety of optical bandwidths are available ranging from ~ 60 nm in a low loss PBG HC-PCF to over 1000 nm in a low loss IC hypocycloid core shape Kagome HC-PCF.

Table (4-2) Comparison of relative HC-PCF parameters for the HC-PCF reported in chapter 3 & 4. *All M Squared measurements are taken using a Phasics SID4 wavefront sensor when a narrow linewidth (~1 MHz) ECDL is coupled through the HC-PCF under test.

HC-PCF Type	Loss (dB/km)	M Squared*	Bandwidth (nm)	MFD (µm)
7 cell PBG	230	1.8	~ 100	3.9
19 cell PBG	107	1.7	~ 60	5.9
DPBG	~ 2000 @ 780 nm 90 @ 1050 nm	3.2	~50 @ 780 nm ~ 100 @ 1050 nm	8.9
IC HC-PCF	70	< 1.1	~ 1050	23.6

A range of HC-PCF have been fabricated to address the different regimes which may be accessed in atomic vapour applications stemming from single particle interactions which require small modal volume to coherent applications such as electromagnetically induced transparency. Potentially all these different applications can now be addressed in a HC-PCF by selecting the correct fibre from table (4-1).

4.6 Summary

State of the art development of hypocycloidal core shape Kagome HC-PCF for guidance in the 780 nm region is reported with an unprecedentedly low loss of 70 dB/km in the spectral range 750 - 850 nm. In addition this fibre has excellent single mode properties and has been used to investigate the mechanism of bend induced loss in Kagome lattice HC-PCF. Bend induced loss in Kagome HC-PCF is primarily dominated by coupling from the core mode to air hole modes of the photonic crystal cladding, despite the large difference in propagation constant. This indicates the robustness of the inhibited coupling guidance mechanism.

The effect of the hypocycloid core shape on the confinement losses in Kagome HC-PCF is investigated numerically and experimentally in a systematic manner. Optimisation of the curvature parameter b to values ~ 1 shows a dramatic reduction in confinement losses in Kagome HC-PCF. This is confirmed experimentally using a fibre design with thick silica struts ~ 1400 nm where greater control of the curvature parameter can be achieved during fabrication. The effect of cladding structure on the confinement and bending losses of Kagome HC-PCF is investigated. Increasing the number of cladding rings above 2 has minimal effect on the confinement losses in Kagome HC-PCF. However increasing numbers of cladding rings dramatically reduce the bending losses. The 3 dB bend radius can be reduced from ~ 5 cm to ~ 2.5 cm at 1310 nm when the number of cladding rings is increased from 1 to 4.

From the numerical simulations of the effect of the hypocycloid core shape on the confinement losses in Kagome HC-PCF it is predicted that confinement losses can be reduced below the 10 dB/km level for guidance at 1.064 μm. Future works will focus on optimising the fibre fabrication parameters to achieve this level of optical attenuation. Additional fabrication will continue to target reducing HC-PCF losses

at all wavelengths especially those for $^{85/87}$Rb and ^{133}Cs based applications. Polarisation control and optimising the bandwidth of hypocycloid core shape Kagome HC-PCF warrant future investigation.

References

1. Couny F, Benabid F, Roberts PJ, Light PS, Raymer MG. Generation and photonic guidance of multi-octave optical-frequency combs. Science (New York, N.Y.) [Internet]. 2007 Nov 16 [cited 2013 Feb 11];318(5853):1118–21. Available from: http://www.ncbi.nlm.nih.gov/pubmed/18006741

2. Wang YY, Wheeler N V, Couny F, Roberts PJ, Benabid F. Low loss broadband transmission in hypocycloid-core Kagome hollow-core photonic crystal fiber. Optics Letters [Internet]. Optical Society of America; 2011;36(5):669–71. Available from: http://dx.doi.org/10.1364/OL.36.000669

3. Wang YY, Peng X, Alharbi M, Dutin CF, Bradley TD, Gérôme F, et al. Design and fabrication of hollow-core photonic crystal fibers for high-power ultrashort pulse transportation and pulse compression. Optics letters [Internet]. 2012 Aug 1;37(15):3111–3. Available from: http://www.ncbi.nlm.nih.gov/pubmed/22859102

4. Nampoothiri a. VV, Jones AM, Fourcade-Dutin C, Mao C, Dadashzadeh N, Baumgart B, et al. Hollow-core Optical Fiber Gas Lasers (HOFGLAS): a review [Invited]. Optical Materials Express [Internet]. 2012 Jun 20;2(7):948. Available from: http://www.opticsinfobase.org/abstract.cfm?URI=ome-2-7-948

5. Yu F, Wadsworth WJ, Knight JC. Low loss silica hollow core fibers for 3-4 μm spectral region. Optics express [Internet]. 2012 May 7;20(10):11153–8. Available from: http://www.ncbi.nlm.nih.gov/pubmed/22565738

6. Yu F, Knight JC. Spectral attenuation limits of silica hollow core negative curvature fiber. Optics Express [Internet]. 2013 Sep 5 [cited 2013 Sep 6];21(18):21466. Available from: http://www.opticsinfobase.org/abstract.cfm?URI=oe-21-18-21466

7. Pryamikov AD, Biriukov AS, Kosolapov AF, Plotnichenko VG, Semjonov SL, Dianov EM. Demonstration of a waveguide regime for a silica hollow - core microstructured optical fiber with a negative curvature of the core boundary in the spectral region > 3 . 5 μm. Optics express. 2011;19(2):1441–8.

8. Kolyadin AN, Kosolapov AF, Pryamikov AD, Biriukov AS, Plotnichenko VG, Dianov EM. Light transmission in negative curvature hollow core fiber in extremely high material loss region. Optics Express [Internet]. 2013 Apr 10 [cited 2013 Apr 29];21(8):9514. Available from: http://www.opticsinfobase.org/abstract.cfm?URI=oe-21-8-9514

9. Debord B, Alharbi M, Bradley T, Fourcade-Dutin C, Wang Y, Vincetti L, et al. Cups curvature effect on confinement loss in hypocycloid-core Kagome HC-PCF. Cleo: 2013 [Internet]. Washington, D.C.: Osa; 2013;CTu2K.4. Available from: http://www.opticsinfobase.org/abstract.cfm?URI=CLEO_SI-2013-CTu2K.4

10. Debord B, Alharbi M, Bradley T, Fourcade-Dutin C, Wang YY, Vincetti L, et al. Hypocycloid-shaped hollow-core photonic crystal fiber Part I: Arc curvature effect on confinement loss. Optics Express [Internet]. 2013 Nov 13 [cited 2013 Nov 13];21(23):28597. Available from: http://www.opticsinfobase.org/abstract.cfm?URI=oe-21-23-28597

11. Alharbi M, Bradley T, Debord B, Fourcade-Dutin C, Ghosh D, Vincetti L, et al. Hypocycloid-shaped hollow-core photonic crystal fiber Part II: Cladding effect on confinement and bend loss. Optics Express [Internet]. 2013 Nov 13 [cited 2013 Nov 13];21(23):28609. Available from: http://www.opticsinfobase.org/abstract.cfm?URI=oe-21-23-28609

12. Bradley TD, Wang YY, Alharbi M, Debord B. Hypocycloid-core Kagome hollow core photonic crystal fiber for Rb and Cs based optical applications. Journal of Lightwave Technology. 2013;31(16):1–4.

13. Couny F, Benabid F, Light PS. Large-pitch kagome-structured hollow-core photonic crystal fiber. Optics Letters [Internet]. Optical Society of America; 2006;31(24):3574–6. Available from: http://opus.bath.ac.uk/8787/

14. Light PS, Benabid F, Couny F, Maric M, Luiten a N. Electromagnetically induced transparency in Rb-filled coated hollow-core photonic crystal fiber. Optics letters [Internet]. 2007 May 15;32(10):1323–5. Available from: http://www.ncbi.nlm.nih.gov/pubmed/17440575

15. Ghosh S, Bhagwat A, Renshaw C, Goh S, Gaeta A, Kirby B. Low-Light-Level Optical Interactions with Rubidium Vapor in a Photonic Band-Gap Fiber. Physical Review Letters [Internet]. 2006 Jul [cited 2013 Feb 13];97(2):023603. Available from: http://link.aps.org/doi/10.1103/PhysRevLett.97.023603

16. Vorrath S, Möller S a, Windpassinger P, Bongs K, Sengstock K. Efficient guiding of cold atoms through a photonic band gap fiber. New Journal of Physics [Internet]. 2010 Dec 9 [cited 2013 Feb 14];12(12):123015. Available from: http://stacks.iop.org/1367-2630/12/i=12/a=123015?key=crossref.fef11793f31fc43564898ca281f561d8

17. Hermann AH, Huang W. Coupled-Mode Theory. Proceedings of IEEE. 1991;79(10):1505–18.

18. Miyagi M. Bending losses in hollow and dielectric tube leaky waveguides. Applied optics. 1981;20(7):1221–9.

19. Roberts P, Couny F, Sabert H, Mangan B, Williams D, Farr L, et al. Ultimate low loss of hollow-core photonic crystal fibres. Optics express [Internet]. 2005 Jan 10;13(1):236–44. Available from: http://www.ncbi.nlm.nih.gov/pubmed/19488348

20. Vincetti L, Setti V. Confinement Loss in Kagome and Tube Lattice Fibers: Comparison and Analysis. Journal of Lightwave Technology [Internet]. 2012 May;30(10):1470–4. Available from: http://ieeexplore.ieee.org/lpdocs/epic03/wrapper.htm?arnumber=6144683

21. Fourcade-Dutin C, Debord B, Dontabactouny M, Honninger C, Mottay E, Vincetti L, et al. Milli-Joule femtosecond laser-pulse delivery and compression in hypocycloid core Kagome HC-PCF. CLEO 2013. 2013. p. 7–8.

22. Alharbi M, Bradley T, Debord B, Fourcade-Dutin C, Ghosh D, Vincetti L, et al. Cladding effect on confinement and bend losses in hypocycloid-core Kagome HC-PCF. Cleo: 2013 [Internet]. Washington, D.C.: Osa; 2013;2:CTu2K.7. Available from: http://www.opticsinfobase.org/abstract.cfm?URI=CLEO_SI-2013-CTu2K.7

Chapter 5

Post Processing of Hollow Core Photonic Crystal Fibre

The post processing techniques which have been developed and optimised for atomic vapour photonic microcell fabrication are presented. These techniques involve physical alterations of the fibre structure through tapering and splicing of HC-PCF. Additionally the physical reactivity of alkali metal vapours can be addressed through the application of coatings to the inner core wall.

5.1 Molecular gas photonic microcell assembly

A photonic microcell (PMC) is an integrated optical component consisting of a length of hollow core photonic crystal fibre (HC-PCF) which has been filled with an active gas media and hermetically sealed to solid optical fibres. PMCs filled with molecular gases such as hydrogen (1) and acetylene (2) have been fabricated repeatedly. The assembly of molecular gas PMCs follows a precise fabrication process including flushing and baking the HC-PCF, active gas loading, evacuating the gas media to achieve the desired pressure and finally splicing through the helium process to seal the PMC (3). The first stage of the post process is baking and purging the HC-PCF with an inert gas (e.g. N_2, ^{18}Ar, ^{4}He). This process removes any residual gases in the hollow core remaining from the fibre drawing and minimises OH content on the inner core wall. To date this PMC fabrication process has been unsuccessful for sealing atomic vapour loaded HC-PCF which is inherently due to the reactivity of the atomic vapour. Previous attempts at sealing atomic vapour cells have either resulted in no optical transmission through the spliced PMC or

transmission but no Rb vapour is present in the PMC. The challenging nature of atomic vapour PMC fabrication necessitates development of novel post processing techniques such as tapering and sleeve splicing to address the technical issues in PMC assembly. Additionally micron-scale confinement of atomic vapours causes increased atom-surface interaction resulting in physio-chemical absorption and enhanced dephasing. These two issues can be addressed through the application of chemically inert wall coatings to the inner core wall of a HC-PCF (see chapter 6 where such ceramic coating is applied). The deposition of such coatings requires a careful process to avoid adversely affecting the HC-PCF transmission and modal properties, which is described in this chapter.

5.2 Gas Loading Dynamics in HC-PCF

Loading Rubidium (Rb) vapour into confined dielectric geometries such as HC-PCF is a notoriously challenging problem in part due to the extremely low vapour pressure of Rb as seen in Fig (5-1) a). This can be overcome to some extent by heating the ultra high vacuum (UHV) environment to increase the temperature dependent vapour pressure (4).

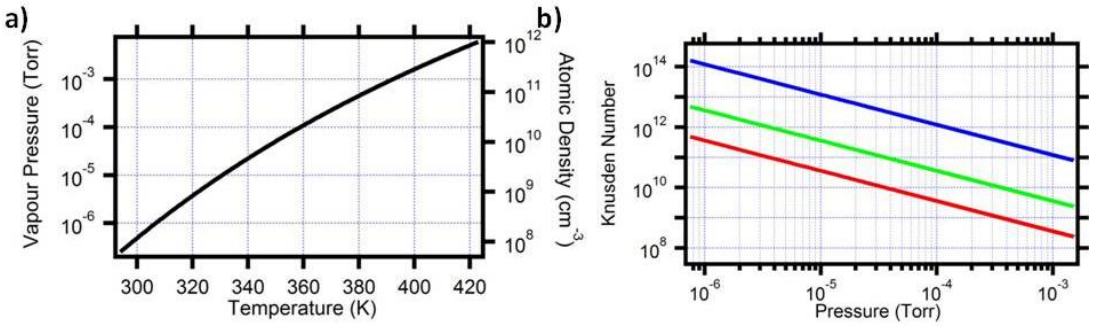

Figure (5-1) a) Rb vapour pressure (atomic density) behaviour with temperature, b) Knusden numbers for Rb vapour at different pressures, (Blue-30 µm diameter, Green-1 mm diameter and red -1 cm diameter)

A second consideration is a union of two problems namely the geometry of the HC-PCF and the low vapour pressure of Rb. This problem manifest itself best by considering the Knudsen number (Eq (5-1)) associated with different gaseous flow regimes (5,6).

$$K_n = \frac{\lambda_{MFP}}{d}, \tag{5-1}$$

where *d* is the diameter of the hole through which the gaseous medium has to diffuse and λ_{MFP} is the mean free path of the Rb atoms given by (5),

$$\lambda_{MFP} = \frac{\sqrt{\pi}\mu}{2P}\left(\frac{2k_B T}{m}\right)^{1/2}, \tag{5-2}$$

where k_B is the Boltzmann constant, T is the temperature, m the atomic mass, μ the viscosity coefficient (7,8) and P is the pressure of the gas. The Knudsen number (K_n) can be used to express the limits of different gas flow regimes. $K_n << 1$ is the regime of hydrodynamic flow, and where a pressure gradient between two section of the hollow core fibre can cause diffusive flow of gaseous mediums from high to low pressure. A second regime corresponds to $K_n >> 1$, and where the atoms or molecules follow the molecular-free flow regime. In this regime the ambient pressure is so low that the atoms can have mean free paths on the order of 10's of centimetres. In such a scenario the atoms do not experience atom-atom collisions and only atom-wall collisions can change the atom's velocity. The Knudsen number (Eq (5-1)) is plotted in Fig (5-1) b) for several different diameter holes as a function of Rb vapour pressure. It can clearly be seen that for high vapour pressure (1×10^{-3} Torr) and large diameter hole (1 cm) the Knudsen number is extremely large ($K_n > 1\times10^{8}$), and the regime is firmly that of molecular free flow. This is still a long way from the typical experimental parameters where the Rb vapour pressure is $< 1 \times 10^{-4}$ Torr and the fibre hollow core has a diameter of ~ 30 μm. In these typical experimental conditions shown by the blue curve in Fig (5-1) b) the Knudsen number is extremely large, typically $K_n > 1\times10^{12}$.

When the large Knudsen numbers are combined with the large aspect ratio of HC-PCF (fibre length >> core diameter), this results in extremely slow loading process of the Rb vapour into the hollow core. A typical pressure evolution of the gas media in a HC-PCF is given by the analytical expression (9),

$$\frac{P(t)}{P_o} = 1 - \frac{8}{\pi}\sum_{j=1,3,5\ldots}^{\infty}\frac{1}{j}\exp\left[-\left(\frac{j\pi}{\xi L}\right)Dt\right], \tag{5-3}$$

where *P(t)* is the pressure inside the HC-PCF at a given time, P_o is the initial gas pressure outside the HC-PCF, j is a positive odd integer, ξ is a geometrical factor equal to unity for gas loading from both open ends and equal to 2 for loading from a

single open end, L is the fibre length, t is the time and D is the diffusion constant which depends on the gas flow regime. The diffusion constant for molecular free regime is given by,

$$D = \frac{2}{3} a\bar{v}, \tag{5-4}$$

where a is the radius and $\bar{v}$ is the average thermal velocity. In the viscous flow regime the diffusion constant is given by,

$$D = \frac{a^2 P_o}{8\eta} \tag{5-5}$$

where P_o is the input gas pressure and η is the gas viscosity. Eq (5-3) is plotted in Fig (5-2) a) for the two different diffusion regimes of molecular free flow (Eq (5-4)) and viscous flow (Eq (5-5)). In the gas dynamics detailed by Eq (5-3) the adsorption to the walls of the HC-PCF are not included. Examples of the characteristic loading time for a molecular gas (acetylene) and atomic vapour (Rb) are shown in Fig (5-2) a) it is immediately obvious how much shorter the loading time for molecular acetylene is compared to Rb vapour.

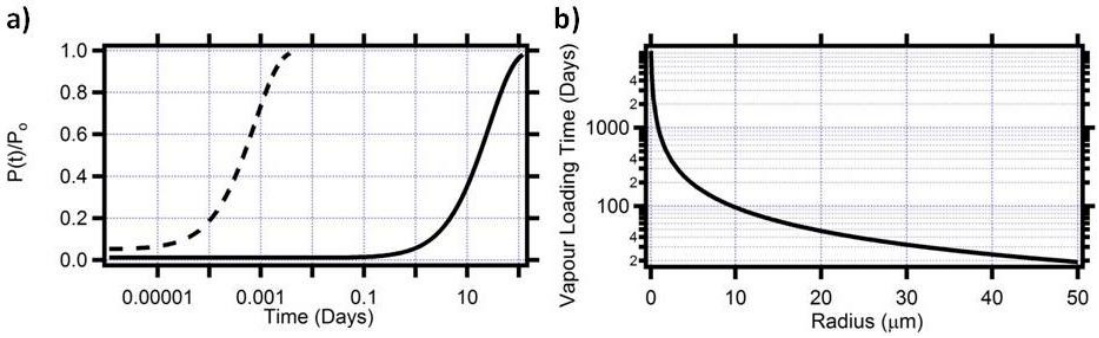

Figure (5-2) a) Molecular acetylene (dashed black) loading in 1 m length of HC-PCF with core diameter of 30 μm and atomic Rb vapour (solid black) loading dynamics in 80 mm length of Kagome HC-PCF with 30 μm diameter hollow core, b) Characteristic Rb vapour loading time as a function of hollow core radius (9)**.**

The characteristic loading time for acetylene gas at P_o = 1 bar in a 1 m HC-PCF with a 30 μm diameter hollow core is approximately 2.5 minutes whereas for Rb vapour the characteristic loading time is 64 days for an 80 mm length. The characteristic loading time is given by,

$$t_{fill} = \frac{(\xi L)^2}{\pi^2 D} \ln\left[\frac{\pi}{8} \times \frac{P_o}{P_o - P}\right] \tag{5-6}$$

where P is 85 % of P_o the other values are as given above. The characteristic ^{85}Rb vapour loading time decreases as a function of the hollow core radius as seen in Fig (5-2) b). For typical Kagome HC-PCF with hollow core radii from 10 – 50 µm the typical loading time varies from ~ 20 - 80 days. If one compares this with a PBG HC-PCF with typical core radii of ~ 3 µm for guidance at 780 nm the vapour loading time exceeds 100 days. Hence the benefit of using large core Kagome HC-PCF compared to PBG HC-PCF for reducing the vapour loading time is readily apparent.

5.3 PDMS Synthesis

Polydimethylsiloxane (PDMS) is a viscous material with viscosity in the region of 4000 mPas (10,11). Such a viscous material does not naturally lend itself to deposition in a confined geometry such as HC-PCF. Traditionally PDMS has been deposited through spin coating on material wafers (10,12). The extreme aspect ratio of HC-PCF requires a new method of deposition discussed below. However for this method to be successful the viscosity of the PDMS must be reduced. Secondly a low viscosity will allow for laminar flow in a microchannel and as such uniform coating deposition. Here we dilute PDMS by volume in diethyl ether to a 0.5 % concentration. Continuous stirring for a 24 hour period ensures uniform distribution of the PDMS in the diethyl ether solvent.

PDMS is chosen for its desirable antirelaxation (13) and LIAD (14) properties which should be advantageous in a HC-PCF. However to date the performance of such coating materials in confined geometries has not been characterised free from transit time broadening and as such the benefits of such materials in HC-PCF is still questioned. This shall be addressed in chapter 7 where the performance of PDMS is quantified through a magneto optical spectroscopic technique independent of transit time broadening.

5.4 Aluminosilicate Sol-Gel Synthesis

Aluminosilicate sol-gel is synthesized by dissolving aluminium nitrate nonahydrate in anhydrous ethanol to a 0.42 mol/L concentration at room temperature under continuous stirring for 12 hours. Then 11 ml of tetraethoxysilane (TEOS) was slowly added drop by drop to the solution under continuous stirring (15,16). The final solution is diluted to a 2 % molar concentration in ethanol to reduce the viscosity when coating the HC-PCF.

Sol-gel preparation is an extremely versatile method for producing surface coatings with a diverse range of physical properties (17,18). This diversity can be achieved because of the range of precursor chemicals which can be utilised for the wet solution from which the sol-gel is fabricated. The versatility of sol-gel chemistry combined with the previously reported properties of aluminosilicate glasses make coatings using aluminosilicate sol-gels extremely desirable. The choice of this material is motivated for its high corrosion resistance as it was demonstrated with silica sol-gel coated stainless steel, and where an increase of corrosion potential with higher heating temperature due to the reduced concentration of hydroxyl groups was reported (19).

5.5 HC-PCF Preparation and Coating Procedure

The most critical aspect of depositing a coating on the inner core wall of a HC-PCF is that the guidance properties such as modal content and transmission loss are not adversely affected by the coating deposition (20). To achieve this it is of paramount importance to deposit a thin film (not exceeding 100 nm thickness) of coating only on the inner core wall of HC-PCF.

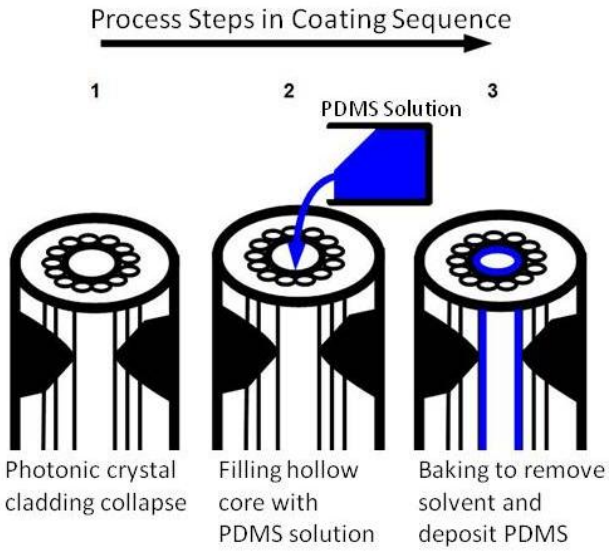

Figure (5-3) Schematic representation of inner core HC-PCF coating procedure

To achieve deposition of thin uniform coating layers, a three step process has been developed to ensure repeatability and uniformity of any coating material deposited. The three step process (Fig (5-3)) consists of HC-PCF preparation (step 1), coating deposition (step 2) and finally coating curing (step 3). The first two stages of the coating process are applicable to all types of coating material which may be deposited in the hollow core. Depending upon the material properties of the coating which is to be deposited the final curing stage may vary slightly from material to material.

The first step in the coating deposition (step 1 in Fig (5-3)) is the preparation of the HC-PCF. This involves collapsing the photonic crystal cladding structure in small section of the HC-PCF at both ends of the fibre while keeping the hollow core open as shown in Fig (5-4). The cladding structure is collapsed while keeping the hollow core open using a filament fusion splicer (Model: Vytran FSS 2000). This allows the hollow core to be filled with a coating solution without filling the photonic crystal cladding structure, hence preserving the guidance properties of the HC-PCF after the coating process. Following the cladding collapse the HC-PCF's are baked at 200 ^{o}C in a vacuum oven for 48 hours to outgas the HC-PCF's extensively before the coating deposition.

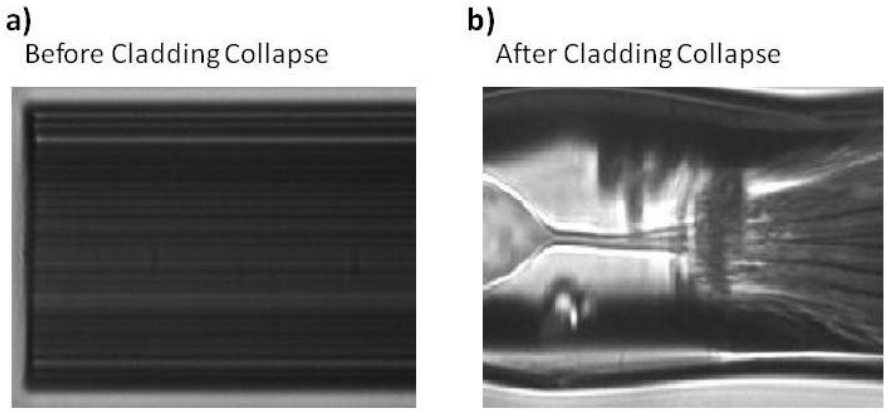

Figure (5-4) a) Optical micrograph of HC-PCF before cladding collapse, b) Optical micrograph of HC-PCF post cladding collapse.

In the lag time while the HC-PCF's are baking the coating materials are synthesised according to the processes in section 5.3 or 5.4. The second stage of the coating process (step 2 in Fig (5-3)) is the coating deposition inside the hollow core of the HC-PCF.

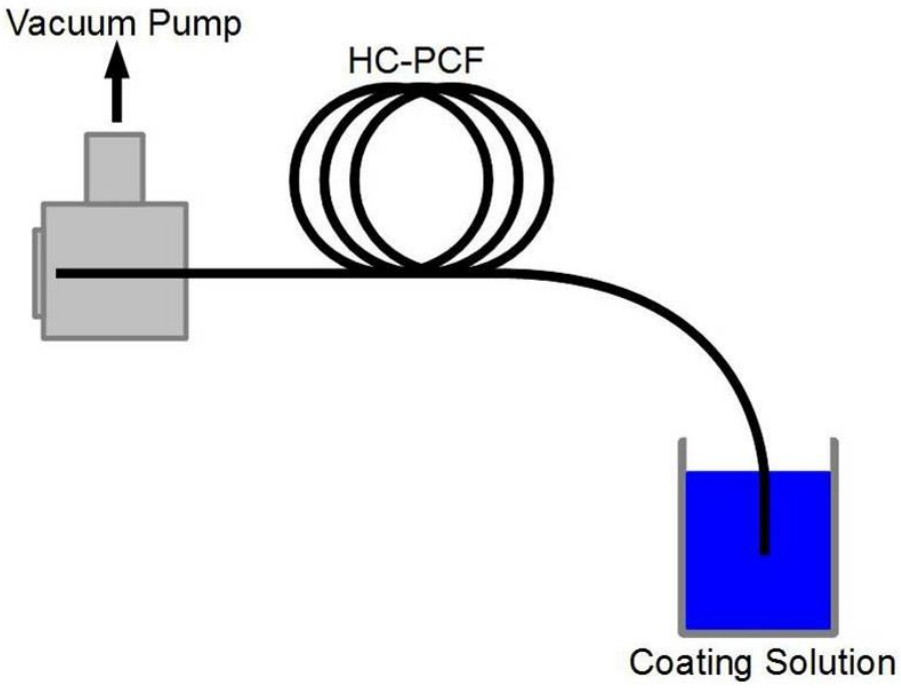

Figure (5-5) Schematic of coating deposition in HC-PCF

One end of the cladding collapsed HC-PCF prepared in stage 1 is inserted in a brass vacuum chamber which is connected to a rough vacuum pump and pressure gauge. The remaining end is inserted in the coating solution as shown in Fig (5-5). The attached rough pump is turned on and a vacuum of 1×10^{-3} mbar is achieved in the chamber drawing the coating solution into the hollow core. Approximately 3

minutes is required to fill a 50 cm fibre with sol gel or a 1 m fibre with PDMS solution. At the end of the HC-PCF filling a liquid droplet can be observed on the fibre end contained in the vacuum chamber. This indicates that the coating solution has successfully been drawn through the hollow core filling the hollow core with the coating solution.

While the first two stages are compatible with deposition of both aluminosilicate sol-gel and PDMS in a HC-PCF the final curing stage (step 3 in Fig (5-3)) is unique to the coating material which has been deposited. In this thesis two coating materials are investigated and deposited inside HC-PCF, these materials are PDMS and aluminosilicate sol-gel.

For curing the PDMS inside the HC-PCF, the PDMS solution filled fibre is removed from the vacuum chamber and placed in an ambient air furnace maintained at 80^{o}C for over 72 hours. This process evaporates the diethyl ether solvent depositing a uniform layer of PDMS on the inner core of the fibre (step 3 in Fig (5-3)). By considering the volume of the fibre core and the percentage of PDMS in the liquid filled HC-PCF and assuming a filling fraction of 100%, we estimate an upper thickness limit of ~ 100 nm for the deposited PDMS coating.

The curing of the aluminosilicate sol-gel inside the HC-PCF is a slightly more involved process than for PDMS. Firstly the liquid sol-gel filled HC-PCF is removed from the vacuum chamber and baked at 80 ^{o}C in an ambient air atmosphere for 24 hours to evaporate the ethanol. Following this process the HC-PCF is baked at a maximum of 600 ^{o}C for 6 hours including a 300 ^{o}C/hour ramp. A thin layer of sol gel is left deposited on the hollow core surround wall. During this time, the densification of the sol gel finalizes the ceramic like structure on the inner core wall (16).

Following these two separate but similar processes both types of coating have successfully been deposited on the inner wall of the HC-PCF. The success of the deposition process is testing the guidance properties of the coated HC-PCF with the deposited coating. An ECDL operating at 780.24 nm is coupled through the HC-PCF and the output is directed to a CCD camera to ensure efficient core mode coupling and provide an analysis of the mode content. Both sol-gel and PDMS coated HC-PCF still guided 780.24 nm laser light in a quasi Gaussian fundamental core mode.

This is indicative that the coating has little impact upon the guidance properties of the HC-PCF hence it is possible to speculate the coating has deposited as a thin uniform film. No additional characterisation of the coated fibres is performed. Finally the PDMS coated HC-PCF's are baked at 100 ^{o}C and the sol-gel coated HC-PCF are baked at 200 ^{o}C in a vacuum furnace to outgas before insertion in the UHV chamber.

5.6 Photonic Microcell Fabrication

A photonic microcell is a gas filled length of HC-PCF hermetically spliced to all solid optical fibres (21). Since the pioneering demonstration by Benabid *et al.* (21) both hydrogen (1) and acetylene (2,22–25) filled PMC's have been demonstrated. To date a significant body of PMC's which have been reported have been fabricated from gas filled PBG HC-PCF because of the possibility to fabricate low loss splices with single mode fibre (SMF) (26). Additionally a significant body of work has been published on using gas filled Kagome lattice HC-PCF's with one or both ends in vacuum chambers for loading and controlling the gas pressure in the hollow core (27–29). While Kagome HC-PCF's have desirable features for PMC fabrication such as reduced overlap with the silica core surround and absence of surface modes their integration in PMC format is challenging. The challenge arises when splicing large pitch Kagome HC-PCF with typical outer diameters between 200 – 350 µm to SMF with outer diameter 125 µm. Firstly the splices are mechanically weak because the SMF typically fuses to the photonic crystal cladding of the Kagome HC-PCF. Secondly the mode field mismatch between large core Kagome HC-PCF and SMF leads results in large splice loss and Fresnel reflections. Thirdly it is difficult to ensure a hermetic splice with no leaking. In ref (24) a PMC based upon a single cell Kagome HC-PCF was reported as an acetylene based frequency reference, while the splice loss is not quantified typical splices losses are around 2.0 dB (30). To date the only work to address large core Kagome HC-PCF for fabrication of PMC's is ref (25), here Kagome HC-PCF were adiabatically tapered to match the outer diameter of SMF and spliced.

5.6.1 Kagome HC-PCF Tapering

To fabricate Rb vapour loaded PMC's, optimisation of the splicing process is a necessity to ensure that the Rb vapour is hermetically sealed in the hollow core free from foreign gas contamination. Tapered Kagome HC-PCF transitions are fabricated as in Ref (25) but instead of a moving flame brush technique (31) a commercial Vytran GPX glass processing station is used. In addition to these techniques a "sleeve" splice technique has been developed.

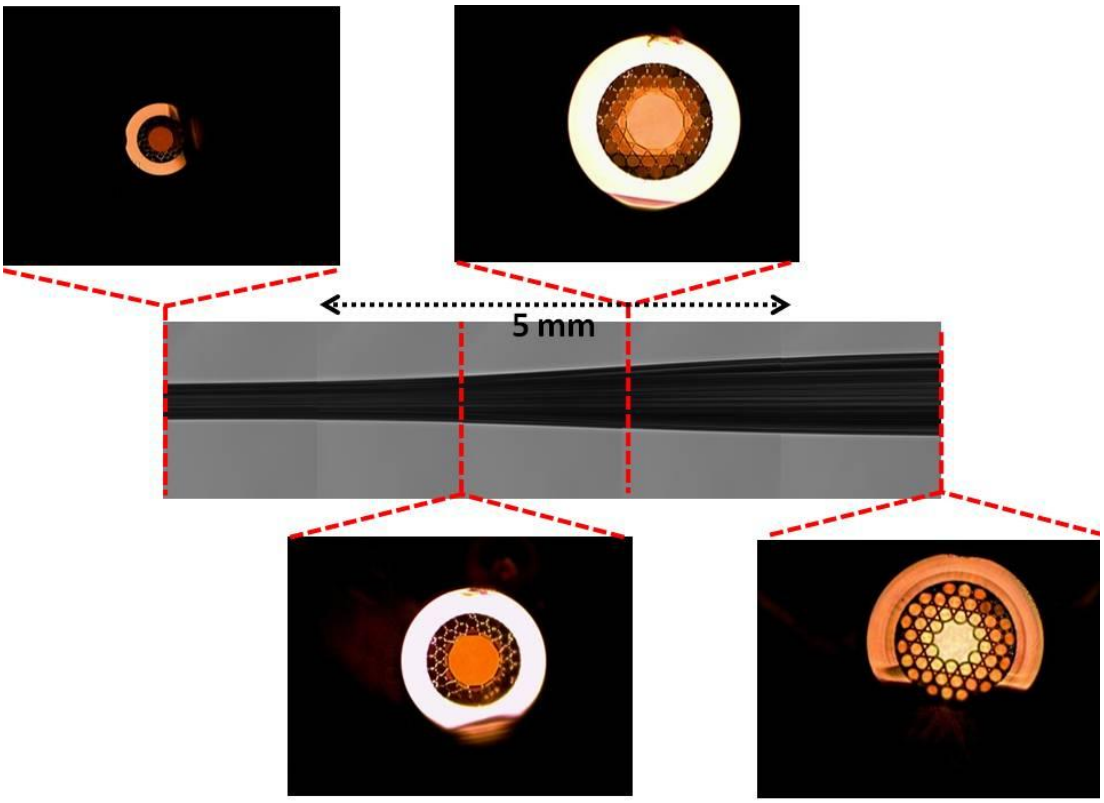

Figure (5-6) Optical micrograph of tapered Kagome HC-PCF from 300 to 125 µm with taper transition of 5 mm. Surrounding optical micrographs of transverse fibre structure through the taper transition

The physical parameters of taper are assessed first as seen in Fig (5-6), a uniform adiabatic taper with a transition length of 5 mm was fabricated. The surrounding optical micrographs show the evolution of the transverse structure of the fibre along the taper. The evolution of the hollow core size in comparison to the cladding hole size appears non uniform along the taper transition. In addition the core shape transitions from the original hypocycloid shape to a circular core in the taper waist region.

Table (5-3) Taper properties characterised using single frequency ECDL, λ = 1532.8 nm. Results averaged over 5 measurements

Taper Transmission Loss (dB)	Taper Kagome - SMF Splice Loss (dB)
0.14	2.6

The loss characteristics of the taper and a tapered Kagome HC-PCF spliced to a SMF are presented in table (5-1), these results were obtained at a single wavelength, λ = 1532.8 nm. It would appear that the tapering has limited impact upon the transmission properties of the fibre with an average loss of 0.14 dB from the taper. The tapered Kagome SMF splice losses are larger than those reported in Ref (25) of ~ 2 dB for a 19 cell core defect Kagome HC-PCF. The un-optimised tapering process, core size mismatch and the transition from hypocycloid to circular core shape could contribute to this discrepancy.

5.6.2 Kagome HC-PCF Sleeve Splicing

The reactivity of Rb vapour presents a final challenge to the fabrication of an Rb vapour loaded PMC. Splicing generally involves heating directly at the fuse position between the two fibres, however in Rb vapour applications this causes the Rb vapour to react strongly with the silica core surround and any foreign gas contamination.

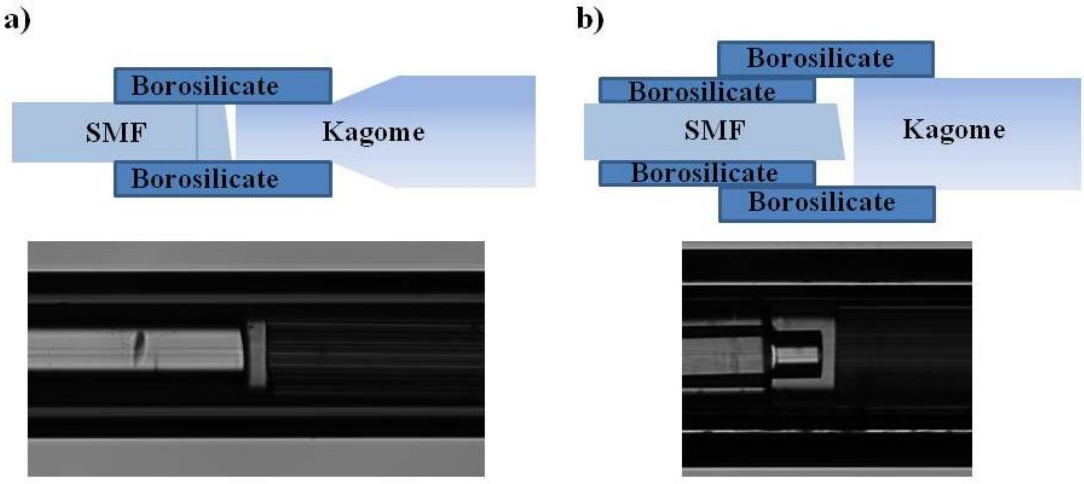

Figure (5-7) a) Angled sleeve splice using tapered Kagome HC-PCF and single borosilicate sleeve, b) Angled sleeve splice to Kagome HC-PCF using two sleeves.

To mitigate this problem a sleeve splicing technique based upon borosilicate capillary sleeves has been developed to use in conjunction with tapered Kagome HC-PCF (Fig (5-7)). Borosilicate glass is selected as the material for the sleeve

because of its lower glass softening temperature (32) compared to that of fused silica (33). Examples of the two different types of sleeve splicing are shown in Fig (5-7). The first sleeve splice (Fig (5-7) a) uses only a single sleeve with a tapered Kagome HC-PCF. The second process (Fig (5-7) b) uses two sleeves the first matches the outer diameter of the SMF with that of the Kagome HC-PCF. The second sleeve creates the hermetic seal between the Kagome HC-PCF and the SMF.

This sleeve splice process allows for hermetic splices with reasonable losses (Table (5-2)) but with the fuse point shifted from the open end of the HC-PCF. The option to fuse the silica sleeves away from the open end of the HC-PCF should reduce the reaction of Rb vapour during the splice process. The optimisation of this splicing process was reported in ref (34) for the development of large core Kagome HC-PCF acetylene filled PMC's. Angle splicing one end of a PMC is necessary to reduce Fresnel reflections at the air glass interface which can lead to the development of an etalon signal. Angle splicing in both single and dual sleeve configuration has been achieved with return losses > 55 dB for a single sleeve. However the single sleeve technique has ~ 2 dB increased transmission loss compared to a conventional taper splice (sleeve free in table (5-1)). Dual sleeve splicing reduces the transmission loss to 2.8 dB but a subsequent reduction in return loss to 43 dB.

Table (5-4) Angle Sleeve Splice characteristics. Loss measurements averaged over 5 repeats.

Splice	Angle (^{o})	Transmission Loss (dB)	Return Loss (dB)
Conventional	0	2.5	16
Single Sleeve	8	4.5	59
Dual Sleeve	8	2.8	43

This section describes the building blocks necessary for fabricating a Rb vapour PMC, in future such work should be possible by combining these results with the Helium diffusion splicing technique (35,36) and results from chapter 6.

5.7 Summary

The requirements for post processing of Kagome HC-PCF for the formation of atomic vapour PMC's and developing solutions to meet the challenges associated with confining atomic vapours on the micron scale are presented. The syntheses of two different coating materials PDMS and aluminosilicate sol-gel which are used in

later chapters are presented. In addition a three step deposition process for coating in the inner core wall of HC-PCF without adversely affecting the guidance properties is presented. This process is generally applicable to all potential coating materials and has been applied for both coating materials used in this thesis. Differences arise in the curing stage due to difference in processing temperatures required. Due to the techniques applicability to HC-PCF other novel coating materials could be deposited using this method in future work.

Post processing of the Kagome HC-PCF by tapering the outer diameter of the fibre to match that of SMF is presented. The taper performance is characterised and the splice loss to SMF is quantified at around 2.6 dB at 1532.8 nm. The technique of sleeve splicing is developed which allows for reasonable loss hermetic splices to be fabricated with the fuse point shifted from the open end of the HC-PCF. The sleeve splice technique reduces the probability of Rb vapour confined in the HC-PCF reacting during the splice process. Angle cleaving has been demonstrated in both a single and dual sleeve configuration with return losses above 40 dB and transmission losses of 2.8 dB.

The obvious future direction from these results is the fabrication of an atomic vapour loaded PMC. However the tapering and sleeve splice results will need to be optimised for the particular Kagome HC-PCF which will be used in the Rb vapour loading experiments. In chapters 6 and 7 the characterisation of both sol-gel and PDMS coatings in Kagome HC-PCF is presented.

References

1. Couny F, Benabid F, Light P. Subwatt Threshold cw Raman Fiber-Gas Laser Based on H2-Filled Hollow-Core Photonic Crystal Fiber. Physical Review Letters [Internet]. 2007 Oct [cited 2013 May 28];99(14):143903. Available from: http://link.aps.org/doi/10.1103/PhysRevLett.99.143903

2. Wheeler N V, Light PS, Couny F, Benabid F. Slow and Superluminal Light Pulses Via EIT in a. Journal of Lightwave Technology. 2010;28(6):870–5.

3. Benabid F. Hollow-core photonic bandgap fibre: new light guidance for new science and technology. Philosophical transactions. Series A, Mathematical, physical, and engineering sciences [Internet]. 2006 Dec 15 [cited 2013 Jan

29];364(1849):3439–62. Available from: http://www.ncbi.nlm.nih.gov/pubmed/17090469

4. Alcock CB, Itkin VP, Horrigan MK. Vapour Pressure Equations for the Metallic Elements: 298–2500K. Canadian Metallurgical Quarterly. 1984;23:309.

5. Sharipov F, Seleznev V. Data on Internal Rarefied Gas Flows. Journal of Physical Chemistry. 1998;27(3):660–709.

6. Weng C, Li W, Hwang C. Gaseous flow in microtubes at arbitrary Knudsen numbers. Nanotechnology. 1999;10:373–9.

7. Yargin VS. Peculiarities in Thermal Conductivity of Alkali Metals in Gas Phase. Relationship Between Thermal Conductivity and Viscosity. Inzhererno-Fizizheskii Zhurnal. 1978;34(3):0–7.

8. Vargaftik NB, Yargin VS. Alkalie metal liquid and vapor thermophysical properties. Inzhererno-Fizizheskii Zhurnal. 2000;54(I).

9. Dicaire I, Beugnot J-C, Thévenaz L. Analytical modeling of the gas-filling dynamics in photonic crystal fibers. Applied optics [Internet]. 2010 Aug 20;49(24):4604–9. Available from: http://www.ncbi.nlm.nih.gov/pubmed/20733632

10. Schneider F, Draheim J, Kamberger R, Wallrabe U. Process and material properties of polydimethylsiloxane (PDMS) for Optical MEMS. Sensors and Actuators A: Physical [Internet]. 2009 Apr [cited 2013 May 23];151(2):95–9. Available from: http://linkinghub.elsevier.com/retrieve/pii/S0924424709000466

11. Aldrich S. PDMS Product specification. 1993 Jan p. 21–2.

12. Mata A, Fleischman AJ, Roy S. Characterization of polydimethylsiloxane (PDMS) properties for biomedical micro/nanosystems. Biomedical microdevices [Internet]. 2005 Dec;7(4):281–93. Available from: http://www.ncbi.nlm.nih.gov/pubmed/16404506

13. Seltzer SJ, Michalak DJ, Donaldson MH, Balabas M V, Barber SK, Bernasek SL, et al. Investigation of antirelaxation coatings for alkali-metal vapor cells using surface science techniques. The Journal of chemical physics [Internet]. 2010 Oct 14 [cited 2013 Feb 13];133(14):144703. Available from: http://www.ncbi.nlm.nih.gov/pubmed/20950026

14. Kasprowicz MJ, Dohnalik T, Jozefowski L, Rubahn K, Rubahn H-G. Diffusion of rubidium atoms in PDMS thin films. Chemical Physics Letters [Internet]. 2004 Jun [cited 2013 Jul 6];391(1-3):191–4. Available from: http://linkinghub.elsevier.com/retrieve/pii/S0009261404006591

15. Hsu MF, Cates GD, Kominis I, Aksay IA, Dabbs DM. Sol-gel coated glass cells for spin-exchange polarized 3He. Applied Physics Letters. 2010;2069(2000):1–4.

16. Schwartz RW, Schneller T, Waser R. Chemical solution deposition of electronic oxide films. Comptes Rendus Chimie [Internet]. 2004 May [cited 2013 Feb 3];7(5):433–61. Available from: http://linkinghub.elsevier.com/retrieve/pii/S1631074804000852

17. Mackenzie JD, Bescher EP. Physical Properties of Sol-Gel Coatings. Journal of Sol-Gel Science and Technology. 2000;19:23–9.

18. Jones SD, Pritchard TN, Lander DF. Physical properties of sol-gel aluminosilicates. Microporous Materials [Internet]. 1995 Jan;3(4-5):419–31. Available from: http://linkinghub.elsevier.com/retrieve/pii/092765139400053X

19. Vasconcelos DC., Carvalho J a. ., Mantel M, Vasconcelos W. Corrosion resistance of stainless steel coated with sol–gel silica. Journal of Non-Crystalline Solids [Internet]. 2000 Aug;273(1-3):135–9. Available from: http://linkinghub.elsevier.com/retrieve/pii/S0022309300001551

20. Jiang-Bing D, Yan-Ge L, Zhi W, Zhan-Yuan L, Gui-Yun K, Xiao-Yi D. Characteristics of Photonic Bandgap Fibres with Hollow Core's Inner Surface Coated by a Layer Material. Chinese Physics Letters [Internet]. 2008 Jan 25;25(1):164–7. Available from: http://stacks.iop.org/0256-307X/25/i=1/a=045?key=crossref.ab6c1adf55e7378a1f5fb8e09a45991d

21. Benabid F, Couny F, Knight JC, Birks T a, Russell PSJ. Compact, stable and efficient all-fibre gas cells using hollow-core photonic crystal fibres. Nature [Internet]. 2005 Mar 24;434(7032):488–91. Available from: http://www.ncbi.nlm.nih.gov/pubmed/15791251

22. Benabid F, Light P, Couny F, Russell P. Electromagnetically-induced transparency grid in acetylene-filled hollow-core PCF. Optics express [Internet]. 2005 Jul 25;13(15):5694–703. Available from: http://www.ncbi.nlm.nih.gov/pubmed/19498571

23. Couny F, Light PS, Benabid F, Russell PSJ. Electromagnetically induced transparency and saturable absorption in all-fiber devices based on 12 C 2 H 2 -filled hollow-core photonic crystal fiber. Optics Communications. 2006;263:28–31.

24. Wang C, Wheeler N V, Lim J, Knabe K, Grogan M, Wang Y, et al. Portable acetylene frequency references inside sealed hollow-core kagome photonic crystal fiber. CLEO 2011 [Internet]. IEEE Computer Society; 2011. p. 23–4. Available from: http://opus.bath.ac.uk/25865/

25. Wheeler N V, Grogan MDW, Light PS, Couny F, Birks T a, Benabid F. Large-core acetylene-filled photonic microcells made by tapering a hollow-core photonic crystal fiber. Optics letters [Internet]. 2010 Jun 1;35(11):1875–7. Available from: http://www.ncbi.nlm.nih.gov/pubmed/20517447

26. Couny F, Benabid F, Light PS. Reduction of Fresnel Back-Reflection at Splice Interface Between Hollow Core PCF and Single-Mode Fiber. IEEE Photonics

Technology Letters [Internet]. 2007 Jul;19(13):1020–2. Available from: http://ieeexplore.ieee.org/lpdocs/epic03/wrapper.htm?arnumber=4232426

27. Knabe K, Wu S, Lim J, Tillman K a, Light PS, Couny F, et al. 10 kHz accuracy of an optical frequency reference based on (12)C2H2-filled large-core kagome photonic crystal fibers. Optics express [Internet]. 2009 Aug 31;17(18):16017–26. Available from: http://www.ncbi.nlm.nih.gov/pubmed/19724600

28. Nampoothiri a. VV, Jones AM, Fourcade-Dutin C, Mao C, Dadashzadeh N, Baumgart B, et al. Hollow-core Optical Fiber Gas Lasers (HOFGLAS): a review [Invited]. Optical Materials Express [Internet]. 2012 Jun 20;2(7):948. Available from: http://www.opticsinfobase.org/abstract.cfm?URI=ome-2-7-948

29. Jones AM, Nampoothiri a VV, Ratanavis A, Fiedler T, Wheeler N V, Couny F, et al. Mid-infrared gas filled photonic crystal fiber laser based on population inversion. Optics express [Internet]. 2011 Jan 31;19(3):2309–16. Available from: http://www.ncbi.nlm.nih.gov/pubmed/21369049

30. Wheeler NV. Molecular and Atomic Confinement in Large Core Photonic Microcells for Slow Light and Laser Metrology Applications. 2010.

31. Birks TA, Li YW. The Shape of Fiber Tapers. Journal of Lightwave Technology. 1992;10(4):432–8.

32. Corning LTD. Low Actinic PYREX Code 7740 Glasses.

33. Corning LTD. HPFS ® Fused Silica Standard Grade. 2003. p. 20–3.

34. Wang C, Bradley TD, Wang YY, Corwin KL, Gerome F, Benabid F. Angle splice of large-core kagome hollow-core photonic crystal fiber for gas-filled microcells. CLEO 2013. 2013. p. 2–3.

35. Benabid F, Roberts PJ, Couny F, Light PS. Light and gas confinement in hollow-core photonic crystal fibre based photonic microcells. Journal of the European Optical Society: Rapid Publications [Internet]. 2009 Jan 21 [cited 2013 Feb 21];4(c):09004. Available from: https://www.jeos.org/index.php/jeos_rp/article/view/09004

36. Light PS, Couny F, Benabid F. Low optical insertion-loss and vacuum-pressure all-fiber acetylene cell based on hollow-core photonic crystal fiber. Optics letters [Internet]. 2006 Sep 1;31(17):2538–40. Available from: http://www.ncbi.nlm.nih.gov/pubmed/16902611

Part II

The outstanding potential and diversity of atomic vapours in physical phenomena such as electromagnetically induced transparency, laser cooling and quantum sensors requires that we find easily integrated compact solutions for scientific and industrial applications. This work carries on from prior work in loading Rb vapour in hollow core photonic crystal fibre (HC-PCF). However while this prior work was proof of principle of the benefits of loading atomic vapours, these upcoming chapters address specific issues which occur when atomic vapours are confined in micron scale geometries. These issues arise from the increased interaction with the waveguide surface in a HC-PCF resulting in increased physio-chemical absorption of Rb vapour to the waveguide core and increased dephasing atom-wall collisions disrupting atomic coherence. In this Part two, three chapters are presented detailing experiments on loading atomic vapours in HC-PCF. The first chapter 6 presents results which attempt to address the loss of atomic vapour by phyiso-chemical absorption to the core cladding interface in HC-PCF. This is achieved by application of a novel aluminosilicate sol-gel coating to the inner core wall of the core cladding interface and a comparative study is undertaken against an uncoated HC-PCF. Chapter 7 addresses the impact of increased number of atom wall collisions in a micron scale hollow core leading to large dephasing of spin polarised atoms. The application of antirelaxation coating materials is known to increase the number of atom wall collisions before dephasing in bulk gas cells, however in confined waveguiding geometries their performance is still a subject of debate. For the first time a magneto optical spectroscopic technique is used to characterise the performance of antirelaxation coating materials free from transit time broadening in a HC-PCF. Chapter 8 the final instalment in this part 2 presents sub Doppler transparency features which have been observed via a novel mechanism for the first time in Rb vapour loaded Kagome HC-PCF. These sub Doppler transparencies are novel in nature because only a single beam is coupled through the HC-PCF to observe these features in the transmitted spectrum. The behaviour of the transparencies are studied with pump power, polarisation and applied magnetic field.

Chapter 6

Rb Vapour Lifetime in Aluminosilicate Sol-Gel Coated Hypocycloidal Core Shape Kagome HC-PCF

In this chapter the challenges associated with loading a micro-structured dielectric geometry such as hollow core photonic crystal fibre (HC-PCF) with Rb vapour are briefly discussed. The mechanisms that have been utilised to overcome these challenges such as light induced atomic desorption and light induced drift are introduced. The advantages and disadvantages of each technique are highlighted.

Aluminosilicate sol-gel is introduced as a coating material which has desirable anti-corrosion properties which should help overcome the physio-chemical absorption difficulties when working with alkali metal vapours in confined geometries. Long Rubidium vapour lifetimes are demonstrated in sol-gel coated Kagome HC-PCF in a comparative study with uncoated fibres.

6.1 Introduction

Confining atomic vapour (^{133}Cs, $^{85/87}$Rb) on the micron scale leads to increased atom surface interaction; this is exacerbated in hollow core photonic crystal fibre (HC-PCF) which exhibits an extremely large surface to volume ratio. The issues around alkali metal vapour loading in HC-PCF were discussed in detail in chapter 5. For ease of reading the main issues associated with alkali metal vapour loading will be briefly recalled. Firstly group 1 alkali metals are highly reactive and have low vapour pressure requiring operation in ultra high vacuum (UHV) environment. This places the loading of such atomic vapours into the HC-PCF core in the regime of molecular free flow which results in a slow and tedious loading process. Secondly the geometry of HC-PCF's does not lend itself to easy loading of vapours because of

the large surface to volume ratio of the hollow core. Residual OH radicals on the silica core surface react with large quantities of Rb vapour. The small core diameter combined with the low vapour pressure places a bottle neck upon the Rb vapour entering the hollow core, i.e. for an Rb atom to successfully enter the hollow core it must be travelling towards the core with in a small range of solid angles. These factors make it extremely challenging to load atomic alkali metal vapours into confined dielectric structures, hence researches have searched for means to mitigate these problems. Secondly, the strong reactivity of the Rb with the surface strongly limits the lifetime of Rb inside the HC-PCF, requiring thus a continuous replenishment.

The techniques of choice for increasing the loading capacity of atomic vapours in confined dielectric structures such as HC-PCF has been light induced drift (1,2) (LID) as used by Light *et al* (3), and for increasing the vapour density inside the core has been light induced atomic desorption (LIAD) (4). The latter has been extensively and successfully used by the group of Alexander Gaeta for generating on demand Rb vapour in photonic bandgap (PBG) HC-PCF (5–9). LIAD is not a means for decreasing the loading time of alkali metal vapours but rather a means to generate large vapour densities rapidly after sufficient exposure of the surface to an electromagnetic radiation (e.g. a laser). On chip integrated hollow and solid anti resonant reflecting optical waveguides (ARROW) loaded with Rb vapour (10,11) utilise on chip Rb vapour reservoirs. However none of these techniques or technologies addresses the fundamental issue of the physio-chemical interaction of the atoms with the surface when utilising confined waveguiding geometries with large aspect ratios. Considering the ongoing research trend towards fabricating compact atomic vapour devices (3,10–15) it is readily apparent that this issue should be addressed.

Here, aluminosilicate sol-gel coating of the inner core wall of HC-PCF's is introduced; the qualities which make aluminosilicate sol-gel a candidate for alkali metal vapour applications are discussed. Experimental results are presented demonstrating extended Rb vapour lifetime within the hollow core of an aluminosilicate sol-gel coated fibre in comparison to HC-PCF with no coating and the background vapour in the UHV chamber.

6.2 Discussion of coating materials for alkali metal vapours applications

Confinement of atomic vapours in bulk geometries is a standardised technique. Inert buffer gases (e.g. He, Ne) have been extensively used to slow the migration of atoms to the walls of the macroscopic vapour cells (16). In addition an extensive body of work has focused on developing antirelaxation coatings for reducing the atom wall collision dephasing rate in buffer gas free atomic vapour cells (17,18). Antirelaxation coatings have been successfully applied in confined waveguiding geometries (3,11,13), however, the quantification of their performance is limited. This will be discussed extensively in chapter 7. On the other hand, and given the recent developments in HC-PCF other coating materials are still to be investigated. Of particular interest is a coating which is chemically inert and minimises surface adsorption. This will be a determinant factor in the development of atomic vapour photonic microcell (PMC), which requires that atomic vapour be maintained within the hollow core free from bulk vacuum equipment and an Rb source. To meet the requirements necessary for PMC fabrication novel coating materials above and beyond antirelaxation materials need to be considered. The aim of these coating materials should be to reduce the rate of reaction between the atomic vapour and the walls of the HC-PCF, thus extending the atomic vapour lifetime within the hollow core without resorting to techniques such as LIAD.

Previous studies on coatings for ultra high vacuum (UHV) based Cs magneto optical trapping applications identified the need for coating materials to have low dielectric constants, low surface absorption energy, low reaction rates and to have low out gassing rates (19). The importance of low surface absorption energy is epitomised by the expression of the atom dwell time on the surface when it is in thermal equilibrium with the surface (20),

$$\tau_s = \tau_0 e^{E_a / k_B T}, \tag{6-1}$$

where $\tau_0 \sim 10^{-12}$ s is the elastic collision time, E_a is the surface absorption energy, k_B is the Boltzmann constant, T is the characteristic temperature of the atom. If surface absorption energy is known then the dwell time on the surface can be readily calculated as shown in Table (6-1). A small difference of 0.3 eV in E_a can drastically increase the dwell time on the surface from 50 ps to 7.6 μs. Increased dwell time on

the surface can result in increased dephasing probability and the atom spends less time in the vapour phase interacting with the laser radiation.

Table (6-1) Surface absorption energy and corresponding dwell time on the surface

Coating Material	Surface Absorption Energy (eV)	Dwell Time (ns) (T = 20 ^{o}C)
OTS	0.4 (19)	7600
Paraffin	0.1 (20)	0.05
PDMS	0.18 (21)	1.3

Low reaction rate as a desirable property speaks for itself in that maintaining atomic vapour in the hollow core rather than chemically bonded to the surface (22,23) of the waveguide is a necessity. In ref (22,23) the formation of alkali metal "whiskers" on the coated surface is observed, in a waveguiding geometry the impact of such "whiskers" could be significantly more dramatic (i.e. perturbation of the optical mode, increased confinement loss). A low out-gassing material is a necessity because the Rb vapour is released and loaded into the HC-PCF in a UHV environment. To minimise time spent pumping down to the UHV level and trying to achieve the lowest possible vacuum in the UHV chamber, sources of out-gassing need to be minimised. Out-gassing from the stainless steel UHV components is minimised by following the procedure in ref (24). Out-gassing from the HC-PCF's is minimised by following the post processing procedures in chapter 5. Additionally low out-gassing materials decrease the amount of foreign gas species with which the atomic vapour can react.

In a previous study by Stephens *et al.* (19) thin sapphire plates and octdecyltrichlorosilane (OTS) were identified as suitable materials for coating atomic vapour cells fulfilling the above criteria, as shown in table (6-2). Table (6-2) outlines some of the materials investigated previously for antirelaxation coatings and gives values for the activation energy and the surface out-gassing rate. As discussed in the previous section the activation energy determines the surface dwell time for alkali metal atoms. Hence from table (6-2) it can be seen that aluminosilicate has significantly lower activation energy than both OTS and sapphire which were identified by Stephens *et al.* as being suitable materials for atomic vapour applications.

Table (6-2) Properties of different potential coating materials as identified by Stephens *et al.* (19) and aluminosilicate glass for comparison.

Coating Material	Activation Energy (eV)	Outgassing Rate (Torr $cm^{-3}cm^2/s$)	Refractive Index	ε_r
Sapphire	0.43 ± 0.1	---	1.81	8.9-11.1 (25)
Pyrex	0.53 ± 0.03	10^{-6}	1.47	4.7
OTS	0.4 ± 0.03	$<4 \times 10^{-7}$	1.46	2.5 (26)
Aluminosilicate	0.28 ± 0.04 (27)	10^{-13} (28)	1.54 (29,30)	4.5 (31)

From Eq (6-1) the dwell time on an aluminosilicate surface can be estimated at ~ 4.4 ns compared to 250 ns and 440 ns for OTS and sapphire respectively. Immediately the benefits of aluminosilicate over OTS and sapphire become obvious. From Ref (28) the out gassing rate from aluminosilicate glasses can be extremely low after proper vacuum baking, a 6 orders of magnitude decrease compared to OTS. Short range interaction between atoms and surfaces are mediated by Van der Waals and electrostatic forces (32). The strength of the two interactions depends upon the polarisability of the surface which is linked to the dielectric constant of the material. At optical frequencies the real part of the effective index $n \sim \sqrt{\varepsilon_r}$, hence the dielectric constant can be estimated. This indicates the degree of polarisability and as such materials with lower dielectric constant have a reduced probability of forming an attractive image charge on the surface. The measured dielectric constants of PDMS, OTS, sapphire and aluminosilicate are 2.8 (33), 2.5 (26), ~9 (25) and 4.5 (31) respectively. The dielectric constant of aluminosilicate is between that of OTS and sapphire both of which were identified by Stephens *et al.* as suitable coating materials. PDMS and OTS are coating material where the shielding effect plays a major role in reducing the interaction with the substrate surface. The electronic properties of aluminosilicate sol-gels were studied in Ref (34) where dielectric constants as low as 5.7 were reported. Additionally by controlling the porosity and the hydroxyl group content of the sol-gel it is possible to tailor the dielectric constant to lower values. From this discussion of the physical and chemical properties of aluminosilicate glasses hopefully the motivation behind choosing this material is now apparent.

6.3 Rb Lifetime in Sol-Gel Coated Kagome HC-PCF

The Kagome HC-PCF is post processed and the aluminosilicate sol-gel coating deposited following the techniques of chapter 5. After the post processing, the sol-gel coated and uncoated Kagome HC-PCF were both inserted in the UHV chamber and the pump down process commenced. Natural Rb vapour is released from a getter source into the UHV chamber containing the sol-gel coated and uncoated HC-PCF's when the ambient UHV chamber pressure is reduced below 5×10^{-8} mbar (Fig (6-1)). Rb vapour loading into 8 cm lengths of aluminosilicate sol-gel coated and uncoated Kagome HC-PCF is continuous for a period of 4 weeks at the end of which the atomic density is $n = 2.8 \times 10^{8}$ cm^{-3} in the sol-gel coated and $n = 2.5 \times 10^{8}$ cm^{-3} in the uncoated Kagome HC-PCF. The atomic density is measured by monitoring the on resonance transmission of a weak probe beam and knowing the atomic cross section, cell temperature and sample length, hence $n = -\frac{1}{\sigma z}\ln(1-A)$ (35). Where σ is the atomic cross section, z is the interaction length, A=1-Tr and here Tr is the relative transmission. In the following chapters the atomic density is calculated in the same manner.

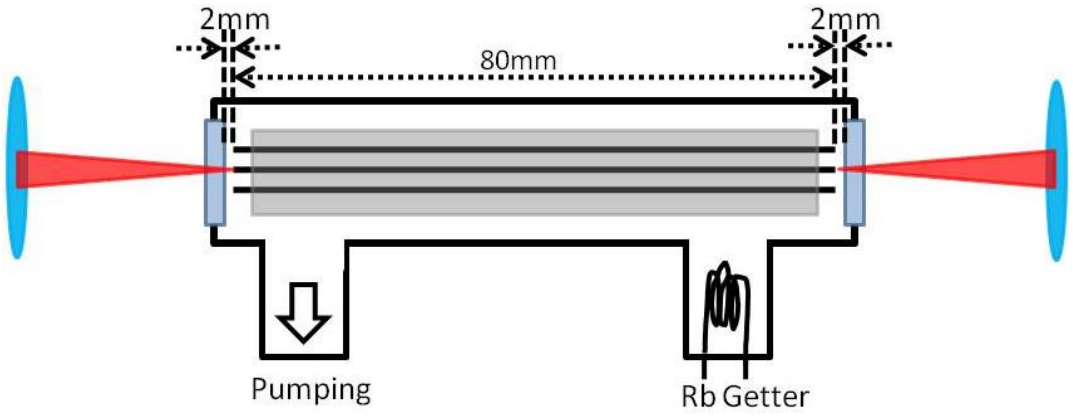

Figure (6-1) Setup of the experimental apparatus used for loading the Sol-Gel coated Kagome HC-PCF's

Comparison can be made between the Rb absorption line contrast when the on resonant external cavity diode laser (ECDL) is coupled to the HE_{11} like core mode or to a mode of the photonic crystal cladding structure. Significant improvement in line contrast can be observed when light is coupled to the core mode indicating that Rb is loaded in the hollow core. An example of the Rb absorption lines during the Rb vapour loading process can be seen in Fig (6-2), here both the ^{85}Rb and ^{87}Rb D2

absorption lines are shown. Greater contrast of the Rb absorption line can be observed in the sol gel coated HC-PCF compared to the bare silica HC-PCF. The larger contrast in the sol gel coated HC-PCF compared to the bare silica HC-PCF is further indication that the coating maintains the Rb vapour in the hollow core. While in the bare silica HC-PCF the Rb vapour under goes both physiosorbition and chemisorbtion to the silica hollow core surround hence resulting in a reduced contrast. For comparison the absorption line contrast is shown across the entire UHV chamber (dashed blue).

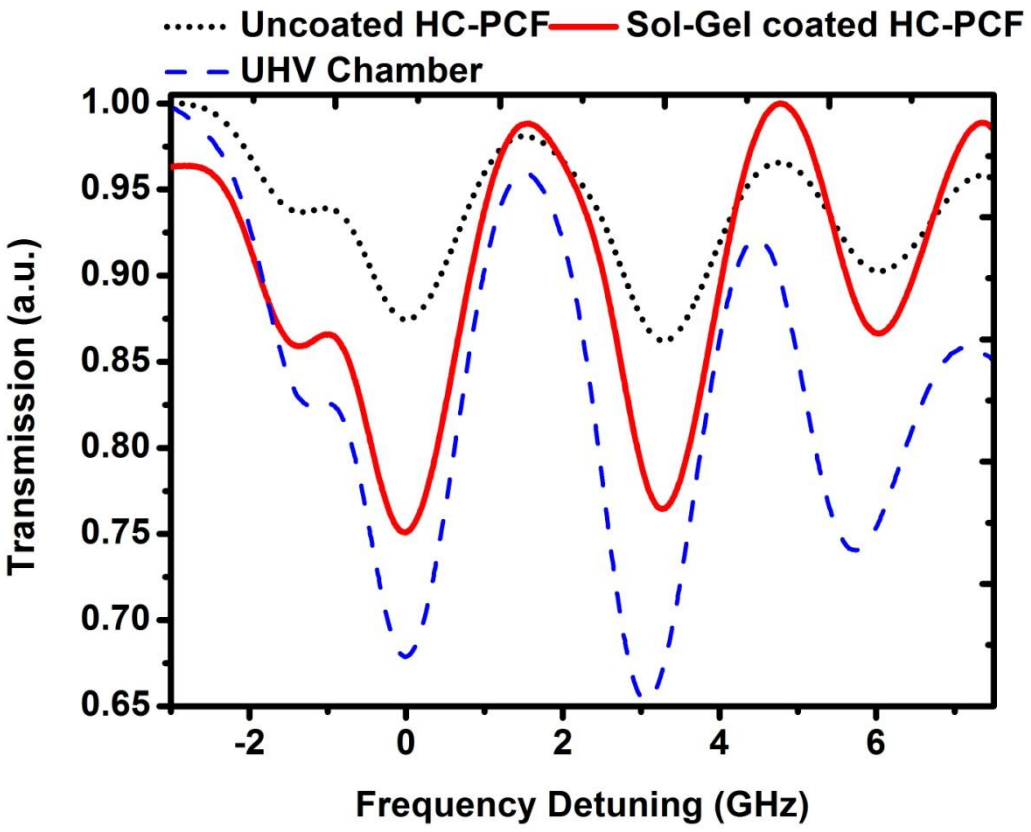

Figure (6-2) Rb Absorption lines of Rb vapour confined in uncoated (dotted black), Sol-Gel coated (solid red) Kagome HC-PCF's and in (dashed blue) UHV chamber for reference.

Once the Rb vapour loading process is complete the current supply to the natural Rb getter source is switched off. The ^{85}Rb $5S_{1/2}$ F=3 → $5P_{3/2}$ F'=2, 3, 4 absorption line is probed using a weak linearly polarised probe beam, power = 180 pW. The linearly polarised probe beam comes from an ECDL operating at 780.24 nm and is coupled through the Rb vapour loaded HC-PCF's. A CCD camera is used to ensure efficient coupling to the fundamental mode of the HC-PCF. A photodiode is used to detect the light exiting the Rb loaded Kagome HC-PCF and measure the absorption line

contrast. The $^{85}Rb\ 5S_{1/2}\ F=3 \rightarrow 5P_{3/2}\ F'=2, 3, 4$ absorption line contrast evolution is recorded over 500 hours in the UHV chamber, the sol gel coated and the uncoated Kagome HC-PCF's as seen in Fig (6-3) a). The photo diode noise equivalent power (NEP) is 2.2 pW/Hz$^{1/2}$ from DC – 1 MHz and the detected off resonant output power for the two Kagome HC-PCF and the UHV chamber is typically ~ 50 ± 5 pW which corresponds to an in chamber fibre coupling efficiency of ~ 27 ± 2 %. Assuming that contrast variations on the order of 10 % of the NEP can be detected, the minimum detectable absorption line contrast is then ~ 0.22/50 pW = 0.4 %. This is in good agreement with the minimum observed experimental contrast of 0.5 % (Fig (6-3) b).

The absorption line contrast in the uncoated HC-PCF rapidly drops to only a 2-5% percent within 100 hours and slowly decays to zero over 450 hours. The contrast in the sol-gel coated Kagome HC-PCF drops slowly decreases from 10 % to 6 % over 400 hours. The Rb absorption contrast across the entire length of the UHV chamber starts off significantly stronger than both fibres but gradually decays to 0 % over 450 hours due to the continuous pumping of the UHV chamber.

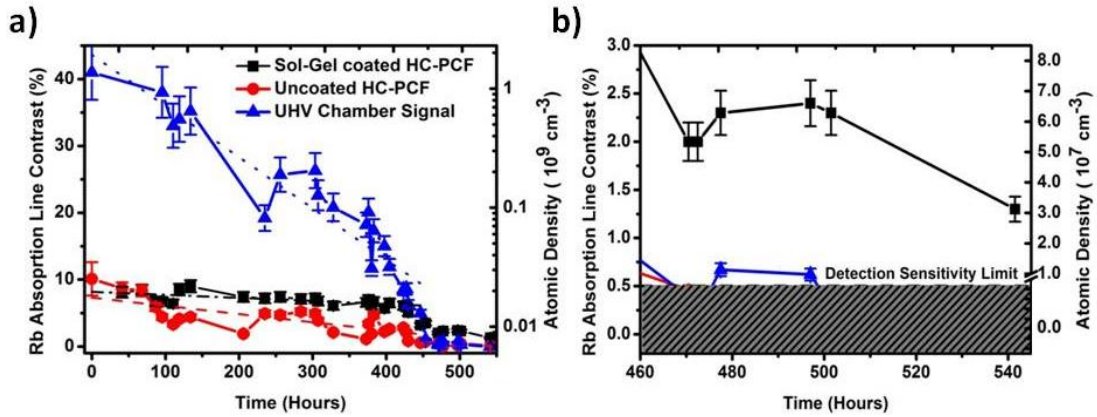

Figure (6-3) a) Rb absorption line contrast evolution in uncoated (red circles) HC-PCF, Sol-Gel (black squares) HC-PCF and UHV chamber, b) Focus on last 80 hours of Rb evolution

In Fig (6-3) a), we can observe qualitatively three linear decay rates, the first spans the time range from 0 - 350 hours and is marked by lines in Fig (6-3) a), the second decay spans ~ 350-450 hours and the third decay spans the region greater than 450 hours. In 0-350 hours range, the UHV signal contrast drops at a rate of 0.07 %/ hr, the uncoated fibre by ~0.01 %/hr, whilst the sol-gel one drops at a linear rate of 0.004%/hr as summarized in the second column of table (6-3). The decay rate in the sol-gel coated fibre is 2.5× slower than the uncoated fibre and ~ 17.5× slower than in the UHV chamber. In the 350 - 450 hours range the UHV signal decay accelerates to

~ 0.19 %/hr, the uncoated fibre ~ 0.04 %/hr and the sol-gel coated ~ 0.03 %/hr. In the second decay regime the decay rate in the sol-gel fibre ~ 1.3× slower than in the uncoated fibre and ~ 6× slower than the UHV chamber. In the final linear decay region (i.e. > 450 hours) a decay rate of 0.02 %/hr is observed only in the sol-gel coated Kagome HC-PCF, while in the uncoated HC-PCF and UHV chamber the signal has dropped below the detection sensitivity limit.

Table (6-3) Decay rates from Fig (6-3) a)

Enviroment	1^{st} Decay (%/hr)	2^{nd} Decay (%/hr)	3^{rd} Decay (%/hr)
UHV Chamber	0.07	0.19	NA
Uncoated HC-PCF	0.01	0.04	NA
Sol-Gel HC-PCF	0.004	0.03	0.02

After 450 hours the Rb absorption line contrast in the vacuum chamber and the uncoated Kagome HC-PCF drop rapidly to zero (Fig (6-3) b) indicating that Rb vapour is no longer present. However the Rb absorption line contrast in the sol-gel coated Kagome HC-PCF is maintained between 1-2% for an additional 80 hours. This is indicative that the sol-gel coating is having the desired effect of reducing the reaction rate with the Rb vapour. This conclusion is drawn on the basis of two observations, first that the Rb absorption contrast in the UHV chamber has dropped to zero indicating that there is no longer an ambient Rb atmosphere around the fibres. Hence the only possible way to detect an Rb absorption line signal is if the vapour is maintained in the sol-gel coated HC-PCF. Secondly in the uncoated Kagome HC-PCF which is from the same length of fibre as that with the sol-gel coating (i.e. identical physical properties to within fabrication tolerances) has zero Rb absorption line contrast. This indicates that all the Rb vapour in the uncoated HC-PCF has reacted with the waveguide walls. The only differences between the two HC-PCF's is the sol-gel coating indicating that the coating has an impact upon the Rb vapour lifetime in the hollow core.

The observation of longer Rb vapour lifetime (Fig (6-3) b) in a sol-gel coated Kagome HC-PCF compared to an uncoated Kagome HC-PCF, where the two fibres have the same physical characteristics raises the question as to why the sol-gel coating has this property. The answer to this question is multi-faceted and requires discussion of the various physical, chemical and electronic properties of aluminosilicate sol-gels which were highlighted earlier in section 6.2. Firstly the

physical structure of the sol-gel should be compared with other well known coating materials such as PDMS and OTS. PDMS and OTS are both self assembly polymer structures with high permeability to gases (33) compared to aluminosilicate sol-gel which has a low porosity ceramic structure (34). Comparison of Helium diffusion rates (Table (6-3)) through PDMS and aluminosilicate shows an 18 order of magnitude reduction in the diffusion rate of Helium through aluminosilicate compared to PDMS. This striking difference in Helium diffusion rates indicates that Rb vapour will be unable to diffuse into aluminosilicate sol-gel coatings and as such will either remain on the coating surface or in the vapour phase in the hollow core. For comparison the diffusion rate for silica is shown (Table (6-4)), the diffusion rate for He through aluminosilicate is five orders of magnitude lower than silica. Hence sol-gel coatings act as a diffusion barrier, preventing gases reaching the substrate surface (36). The coating performance is dependent on its uniformity (lack of cracking and delamination present in the film) on the coating thickness and finally on its compactness, which sets its level of porosity. The porosity of the sol-gel and hence its permeability can be controlled through the fabrication parameters (e.g. temperature, concentration). Decreasing the pore dimensions restricts the diffusion of gases through the film (37).

Table (6-4) Helium diffusion rates through coating materials

Material	Diffusion Rate (^{4}He) (cm^2/s)
PDMS	6.0×10^{6} (33,38)
Aluminosilicate	5.4×10^{-12} (39,40)
Silica	5.0×10^{-7} (41,42)

In addition to the physical properties of the sol-gel coating the electronic properties of the sol-gel coating are of vital importance. The measured refractive indices and dielectric constants are shown in Table (6-2) for different coating materials. Low dielectric constant materials have a reduced polarisability and as such the short range Van der Waals and electrostatic forces that mediate atom surface interactions will be reduced (32). This results in reduced attraction to the surface and lower dwell time at a specific surface lattice site. The surface activation energy of the aluminosilicate is lower than both OTS and sapphire (Table(6-2)) which were identified by Stephens *et al.* (19) as suitable coating materials for Cs magneto optical trapping. The surface activation energy of aluminosilicate is 0.28 eV (27) which from Eq (6-1)

corresponds to a surface dwell time of ~ 4.4 ns, two orders of magnitude lower than that of sapphire ~ 440 ns. Considering the high impermeability to gaseous media, reduced surface polarisability and low surface activation energy it is speculated that Rb atoms have a weak short time period interaction with aluminosilicate surfaces. It is thought that this is due to a combination of the factors discussed above. Firstly the interaction time on the surface is short on the order of nanoseconds and secondly the short range Van der Waals and electrostatic forces that mediate the atom surface interaction are reduced because of the low polarisability of the surface. Thirdly the aluminosilicate surface is highly impermeable as such in the short atom dwell time (< 10 ns) on the surface there is little possibility for the atom to absorb in the aluminosilicate coating. Hence these combined properties effectively extends the Rb vapour lifetime in the sol-gel coated Kagome HC-PCF.

6.4 Summary

The technical challenges associated with working with Rb vapour in extremely confined geometries with very large aspect ratios such as HC-PCF are briefly discussed. Some of the experimental techniques which have been used to speed the loading of Rb vapour are briefly outlined. Discussion of previous work on coating materials for atomic vapour applications are presented and the conclusions of these works summarised. Aluminosilicate sol-gel is introduced as a potential coating material with excellent physical and chemical properties for reduced atom surface interaction. These properties are compared with those identified by Stephens *et al.* as being desirable for atomic vapour applications and contrasted with materials which have been identified as suitable for atomic vapour applications.

Several sections from the same Kagome HC-PCF fabrication are post processed in accordance with chapter 5 and aluminosilicate sol-gel is synthesised and deposited on the inner core wall of one fibre. Sol-gel coated and uncoated Kagome HC-PCF's are inserted in a UHV chamber and loaded with Rb vapour. At the end of the loading process the current source to the natural Rb getter is turned off. The time dependent evolution of the Rb vapour is monitored in the UHV chamber, the uncoated and sol-gel coated Kagome HC-PCF's over a period of 500 hours. Experimental observation demonstrates that Rb vapour is maintained in the sol-gel coated Kagome HC-PCF

for greater than 500 hours with no fresh Rb release. The striking result however is that for the Rb vapour can be maintained for an additional 80 hours in the sol-gel coated Kagome HC-PCF, even when all the ambient Rb vapour has been pumped away and all the Rb vapour in an uncoated Kagome HC-PCF has reacted with the walls of the waveguide. From discussion of the physical, chemical and electronic properties of aluminosilicate sol-gel it is speculated that the Rb vapour has a very weak interaction with the sol-gel surface for a short period of time (< 10 ns). As such the Rb atoms do not react or bond with the sol-gel surface resulting in a greater vapour lifetime in the hollow core. The potential for long Rb vapour lifetimes free from an Rb source demonstrated in this work opens up exciting possibilities. One of these possibilities is fabricating Rb vapour PMC's where large atomic densities could be maintained in the hollow core free from external vacuum equipment and Rb sources. If the performance and lifetime of such a device could be characterised then Rb vapour PMC's has potential to become a versatile platforms which can compete with existing compact devices e.g. the microchip atomic clock.

One of the primary strengths of the sol-gel technique is the incredible versatility that is on offer, this can come by varying the precursor chemicals and/or the processing parameters (e.g. curing temperatures/time). Tailoring of these different parameters allows for control of both physical properties such as the coating thickness and electronic properties such as the dielectric constant. Future development will focus on depositing completely different sol-gel materials inside HC-PCF's with different physical and chemical properties to study the benefits and effects these have on the Rb vapour. Additionally aluminosilicate sol-gels could be studied in depth by varying the ratio of Al to SiO_2 in the sol-gel and by altering the treatment process. Both of these routes offer the potential to tailor the sol-gel and optimise the performance in maintaining Rb vapour. Such a study offers secondary information in understanding further the physical nature of the reaction or lack thereof between the Rb atoms and the sol-gel surface. This information will be of critical importance for fabricating Rb vapour PMC's where the longevity and performance will be of fundamental importance. A final possibility afforded by sol-gels is the ability to build multilayer structures by repeat sol-gel processes. This could be used to generate multilayer sol-gel structures with specific properties or sol-gel layers could be combined with organosilane self assembly polymers. Sol-gel polymer layered

structures could have the dual benefits of the apparent lack of interaction with the sol-gel surface combined with the antirelaxation properties of many polymers such as PDMS and OTS.

References

1. Gel'mukhanov FK, Shalagin AM. Light-induced diffusion of gases. JETP Letters. 1979;29(12):773–6.

2. Antsygin VD, Atutov SN, Gel'mukhanov FK, Telegin GG, Shalagin AM. Light-induced diffusion of sodium vapor. JETP Letters. 1979;30(5):262–5.

3. Light PS, Benabid F, Couny F, Maric M, Luiten a N. Electromagnetically induced transparency in Rb-filled coated hollow-core photonic crystal fiber. Optics letters [Internet]. 2007 May 15;32(10):1323–5. Available from: http://www.ncbi.nlm.nih.gov/pubmed/17440575

4. Meucci M, Mariotti E, Bicchi P, Marinelli C, Moi L. Light-Induced Atom Desorption. Europhysics Letters [Internet]. IOP Publishing; 1994;25(9):639–43. Available from: http://iopscience.iop.org/0295-5075/25/9/001

5. Bhagwat A, Slepkov A, Venkataraman V, Londero P, Gaeta A. On-demand all-optical generation of controlled Rb-vapor densities in photonic-band-gap fibers. Physical Review A [Internet]. 2009 Jun [cited 2013 Feb 25];79(6):063809. Available from: http://link.aps.org/doi/10.1103/PhysRevA.79.063809

6. Slepkov AD, Bhagwat AR, Venkataraman V, Londero P, Gaeta AL. Spectroscopy of Rb atoms in hollow-core fibers. Physical Review A [Internet]. 2010 May [cited 2013 Feb 25];81(5):053825. Available from: http://link.aps.org/doi/10.1103/PhysRevA.81.053825

7. Slepkov AD, Bhagwat AR, Venkataraman V, Londero P, Gaeta AL. Generation of large alkali vapor densities inside bare hollow-core photonic band-gap fibers. Optics express [Internet]. 2008 Nov 10;16(23):18976–83. Available from: http://www.ncbi.nlm.nih.gov/pubmed/19581990

8. Londero P, Venkataraman V, Bhagwat A, Slepkov A, Gaeta A. Ultralow-Power Four-Wave Mixing with Rb in a Hollow-Core Photonic Band-Gap Fiber. Physical Review Letters [Internet]. 2009 Jul [cited 2013 Feb 25];103(4):043602. Available from: http://link.aps.org/doi/10.1103/PhysRevLett.103.043602

9. Venkataraman V, Londero P, Bhagwat AR, Slepkov AD, Gaeta AL. All-optical modulation of four-wave mixing in an Rb-filled photonic bandgap fiber. Optics letters [Internet]. 2010 Jul 1;35(13):2287–9. Available from: http://www.ncbi.nlm.nih.gov/pubmed/20596222

10. Yang W, Conkey DB, Wu B, Yin D, Hawkins AR, Schmidt H. Atomic spectroscopy on a chip. Nature Photonics [Internet]. 2007 Jun [cited 2013 Feb

13];1(6):331–5. Available from: http://www.nature.com/doifinder/10.1038/nphoton.2007.74

11. Wu B, Hulbert JF, Lunt EJ, Hurd K, Hawkins AR, Schmidt H. Slow light on a chip via atomic quantum state control. Nature Publishing Group; 2010;4(November):5–8. Available from: http://dx.doi.org/10.1038/nphoton.2010.211

12. Knappe S, Shah V, Schwindt PDD, Hollberg L, Kitching J, Liew L-A, et al. A microfabricated atomic clock. Applied Physics Letters [Internet]. 2004 [cited 2013 Feb 13];85(9):1460. Available from: http://link.aip.org/link/APPLAB/v85/i9/p1460/s1&Agg=doi

13. Ghosh S, Bhagwat A, Renshaw C, Goh S, Gaeta A, Kirby B. Low-Light-Level Optical Interactions with Rubidium Vapor in a Photonic Band-Gap Fiber. Physical Review Letters [Internet]. 2006 Jul [cited 2013 Feb 13];97(2):023603. Available from: http://link.aps.org/doi/10.1103/PhysRevLett.97.023603

14. Stern L, Desiatov B, Goykhman I, Levy U. Nanoscale light-matter interactions in atomic cladding waveguides. Nature communications [Internet]. Nature Publishing Group; 2013 Jan [cited 2013 May 29];4:1548. Available from: http://www.pubmedcentral.nih.gov/articlerender.fcgi?artid=3615375&tool=pmcentrez&rendertype=abstract

15. Stern L, Desiatov B, Goykhman I, Levy U. Evanescent light-matter Interactions in Atomic Cladding Wave Guides. 2012 Apr 2 [cited 2013 Feb 13];20(27):10. Available from: http://arxiv.org/abs/1204.0393

16. Happer W. Optical Pumping. Reviews of Modern Physics. 1972;44(2):169–222.

17. Seltzer SJ, Michalak DJ, Donaldson MH, Balabas M V, Barber SK, Bernasek SL, et al. Investigation of antirelaxation coatings for alkali-metal vapor cells using surface science techniques. The Journal of chemical physics [Internet]. 2010 Oct 14 [cited 2013 Feb 13];133(14):144703. Available from: http://www.ncbi.nlm.nih.gov/pubmed/20950026

18. Yi YW, Robinson HG, Knappe S, Maclennan JE, Jones CD, Zhu C, et al. Method for characterizing self-assembled monolayers as antirelaxation wall coatings for alkali vapor cells. Chemical Analysis. 2008;1–7.

19. Stephens M, Rhodes R, Wieman C. Study of wall coatings for vapor-cell laser traps. Journal of Applied Physics [Internet]. 1994 [cited 2013 Mar 13];76(6):3479. Available from: http://link.aip.org/link/JAPIAU/v76/i6/p3479/s1&Agg=doi

20. Bouchiat MA, Brossel J. Relaxation of Optically Pumped Rb Atoms on Paraffin-Coated Walls. Physical Review. 1966;147(1).

21. Arslanov V V, Ogarev VA. Kinetics of the fusion of drops of polydimethylsiloxane on solid surfaces. Izvestiya Akademi Nauk SSSR. 1974;(8):1795–9.

22. Balabas M V., Sushkov A o., Budker D. Rubidium " whiskers " in a vapour cell. Nature Physics. 2007;3(January):33401.

23. Seltzer SJ. Developments in Alkali-Metal Atomic Magnetometry. 2008.

24. Lewandowski HJ, Harber DM, Whitaker DL, Cornell EA. Simplified System for Creating a Bose-Einstein Condensate.

25. Harman AK, Ninomiya S, Adachi S. Optical constants of sapphire (alpha-Al2O3) single crysals. Journal of Applied Physics. 1994;76(12).

26. Di C, Yu G, Liu Y, Guo Y, Sun X, Zheng J, et al. Effect of dielectric layers on device stability of pentacene-based field-effect transistors. Physical chemistry chemical physics : PCCP [Internet]. 2009 Sep 7 [cited 2013 Jul 14];11(33):7268–73. Available from: http://www.ncbi.nlm.nih.gov/pubmed/19672538

27. Giuntini JC, Douillard JM, Maurin G, Devautour-Vinot S, Nicolas a., Henn F. Aluminosilicate surface energy and its evolution upon adsorption using dielectric relaxation spectroscopy. Chemical Physics Letters [Internet]. 2006 May [cited 2013 May 3];423(1-3):71–5. Available from: http://linkinghub.elsevier.com/retrieve/pii/S0009261406003824

28. Redhead P a. The ultimate vacuum. Vacuum Surface Engineering, Surface Instrumentation & Vacuum Technology [Internet]. 1999 May;53(1-2):137–49. Available from: http://linkinghub.elsevier.com/retrieve/pii/S0042207X98003492

29. Farrell RA, Neu JT. Refractive Index of Several Glasses as a Function of Wavelength and Temperature *. Journal of the Optical Society of America. 1969;59(6):774–6.

30. Benatsou M, Capoen B, Bouazaoui M. Structural and Optical Properties of Sol-Gel Derived Aluminosilicate Planar Waveguides Doped with Er 3 Ions. 1998;533:529–33.

31. Teiserskis A, Zukova A, Gun'ko YK, Grudinkin S, Perova TS, Moore R a. Investigation of alumina–silica films deposited by pulsed injection metal–organic chemical vapour deposition. Thin Solid Films [Internet]. 2006 Dec [cited 2013 Jul 12];515(4):1830–4. Available from: http://linkinghub.elsevier.com/retrieve/pii/S0040609006008054

32. Zaremba E, Kohn W. Van der Waals interaction between an atom and a solid surface. Physical Review B. 1976;13(6).

33. Kuo ACM. Poly (dimethylsiloxane). 1999. p. 411–35.

34. Hietala SL, Smith DM, Hietala VM, Brinker CJ. Closed porosity aluminosilicate for electronic packaging applications. Journal of Materials Research [Internet]. 2011 Jan 31;8(05):1122–7. Available from: http://www.journals.cambridge.org/abstract_S0884291400020446

35. Petersen M. Laser-cooling of neutral Mercury and Laser-spectroscopy of the 1S0 - 3P0 transition. 2009. p. 1–156.

36. Guglielmi M. Sol-Gel Coatings on Metals. Journal of Sol-Gel Science and Technology. 1997;8:443–9.

37. Jones SD, Pritchard TN, Lander DF. Physical properties of sol-gel aluminosilicates. Microporous Materials [Internet]. 1995 Jan;3(4-5):419–31. Available from: http://linkinghub.elsevier.com/retrieve/pii/092765139400053X

38. Robb WL. Thin silicone membranes-thier prmeation properties and some applications. Annals of the New York Academy of Sciences. 1968;146:119–37.

39. Altemose VO. Helium Diffusion through Glass. Journal of Applied Physics [Internet]. 1961 [cited 2013 Mar 14];32(7):1309. Available from: http://link.aip.org/link/JAPIAU/v32/i7/p1309/s1&Agg=doi

40. Fitzsimmons WA, Tankersley LL, Walters GK. Nature of Surface-Induced Nuclear-Spin Relaxation of Gaseous He3+. Physical Review. 1969;179(1):156–65.

41. Williams GA, Ferguson JB. The Diffusion of Hydrogen and Helium through Silica Glass and other Glasses. Journal of the American Chemical Society. 1922;44(10):2160–7.

42. Norton FJ. Permeation of Gases through Solids. Journal of Applied Physics [Internet]. 1957 [cited 2013 Jul 3];28(1):34. Available from: http://link.aip.org/link/JAPIAU/v28/i1/p34/s1&Agg=doi

Chapter 7

Polarisation and Coherence Time measurements in Rubidium loaded Hypocycloidal Core Shape Kagome HC-PCF

Spin polarised atoms are fundamental to applications such as sensitive magnetometry and frequency standards. In this chapter ground state polarisation relaxation times are measured directly for the first time in confined waveguiding geometry utilising a magneto optical spectroscopic technique in Rb vapour loaded borosilicate capillaries and hollow core fibres. Polydimethylsiloxane coated borosilicate capillaries and hypocycloidal core shape Kagome HC-PCF are used for the tests. Electromagnetically induced transparency measurements are recorded for Rb vapour loaded polydimethylsiloxane coated borosilicate capillaries and hypocycloidal core shape Kagome HC-PCF.

7.1 Introduction

Ground state polarisation relaxation times can be maximised by use of antirelaxation coatings and/or inert buffer gases (^{4}He, ^{10}Ne, ^{18}Ar) (1). Since the 1960's anti-relaxation coatings have been investigated for their spin polarisation (2,3) preservation properties in atom wall collisions for applications such as atomic frequency standards (4–6), magnetometry (7,8), and, quantum and nonlinear optical effects (9–11). Initial investigations centred on paraffin (2,4,12) coatings and there derivatives but more recent work has

expanded to the use of self assembly dry films such as octadecyltrichlorosilane (OTS) (13,14), octadecyldimethylmethoxysilane (ODMS) (15) and polydimethylsiloxane (PDMS) (16). In 2010 alkene based coatings were reported with 60 s long transverse relaxation times (17).

Two different characteristic time constants can be attributed to the relaxation of spin polarised atoms colliding with antirelaxation coatings. The first time constant is referred to as the longitudinal relaxation time (T1) because of its historical significance in nuclear magnetic resonance (NMR) experiments. The longitudinal relaxation time (T1) describes the characteristic time period over which the excited state population decays (18,19). The second time constant is referred to as the transverse relaxation time (T2). The transverse relaxation time (T2) depicts the time scale over which the phase relationship of the excited state population is disrupted (20) and is generally faster than the longitudinal relaxation (i.e. T2 < T1).

Bouchiat and Brossel (2) postulated the existence of two weak magnetic type interactions on the surface of antirelaxation coatings which act to depolarise the atom. The first interaction is a dipole-dipole interaction between the electron spin $\vec{S}$ and the nuclear spin $\vec{I}$ of the hydrogen atoms of the coating surface. This interaction was shown to have a relatively long correlation time $\tau_{c1} = 4 \times 10^{-10} s$ which can be physically interpreted as a dwell time at a particular lattice site on the wall coating. The second interaction is a spin orbit interaction, which is dependent on the relative angular momentum of the colliding atom. This spin orbit interaction has a correlation time $\tau_{c2} = 1 \times 10^{-12} s$ which is on the order of thermal vibrations around a particular site on the coating surface. Antirelaxation coatings provide a second function of equal importance to their spin preserving properties. This is, to reduce level of alkali metal interaction with the glass substrate which forms the walls of most conventional macroscopic gas cells.

7.2 Decoherence phenomena in HC-PCF

Decoherence or dephasing of polarised atoms can reduce the precision measurements which are possible using alkali metal vapours due to the broadening of the spectral features these processes rely on. Broadening of absorption lines and narrow transparency features such as in electromagnetically induced transparency (EIT), coherent population trapping (CPT) or in saturable absorption spectroscopy (SAS) can be caused by a range of mechanisms such as Doppler, collision (pressure), transit time and power broadening. In the case of Rb filled HC-PCF, the typical experimental conditions are (i), low Rb vapour density (~1 - 7 × 10^9 cm^{-3}), and (ii), a micrometre scale transverse dimension (typically 10 – 40 μm diameter range, 10^4 shorter than the mean free path of Rb). The low vapour density of Rb (21) means that the probability of atom-atom collisions are extremely low. In the Rb filled HC-PCF, the self broadening contribution to the linewidth, $\gamma_{SB} = \beta_2 n \sim 100 Hz$ (22), where β_2 = 1.1 × 10^{-7} $Hzcm^{-3}$ (22,23) is the self broadening coefficient and n is the atomic density. Finally, because of the waveguiding nature of HC-PCF, the geometrical diameter of the fibre core is very close to the beam diameter. An approximate relationship between the fibre hollow core radius, R_{core} and the mode-field radius, R_{MFD} of the HE_{11} guided mode is $R_{MFD} \sim (\pi/4) R_{core}$. This salient feature, which is illustrated in Fig 7-1, makes it challenging to distinguish transit time broadening from the atom-wall collision broadening. Furthermore, it puts into question the judiciousness of an anti-relaxation coating to reduce the linewidth of optical transition induced sub-Doppler spectral lines, as the linewidth will always be limited by transit time broadening.

The transit time broadening and atom wall collision broadening are respectively given by the following (20,24,25),

$$\gamma_{TT} = \frac{0.58}{\pi R_{MFD}} \sqrt{\frac{2 k_B T}{m}}, \tag{7-1}$$

and

$$\gamma_{walls} = \frac{2.405^2 D}{R_{core}^2}\left(\frac{1}{1+cK_n}\right). \tag{7-2}$$

Here k_B is the Boltzmann constant, T is the temperature, m is the atomic mass, c = 6.8 is obtained from the hard sphere model (26), K_n is the Knudsen number as defined in chapter 5 Eq (5-1) and D is the diffusion coefficient given by (27)

$$D = \frac{1.86\times10^{-22}T^{3/2}}{P\sigma^2\sqrt{m}}, \tag{7-3}$$

where T is the temperature, P is the pressure and σ is the atomic collision cross section (28) which equals 2.9×10^{-9} cm^2 for ^{85}Rb.

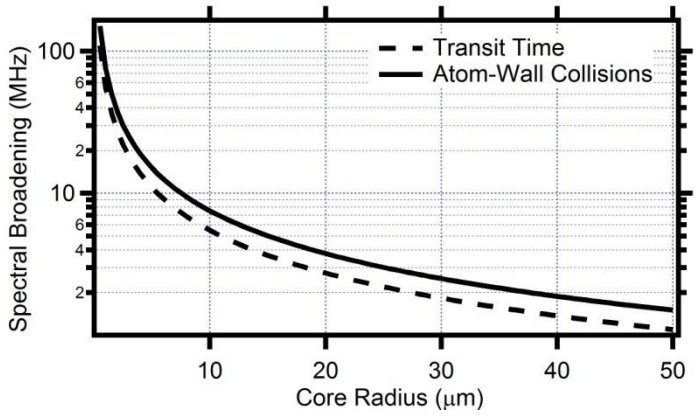

Figure (7-1) Rb vapour dephasing rate due to atom-wall collisions (solid black) and transit time (dashed black) as a function of hollow core radius.

The dephasing rates given by Eq (7-1) and Eq (7-2) and shown in Fig (7-1), can be drastically reduced by using large core fibres because of the R^{-1} dependence. Hence using Kagome large pitch fibres is advantageous over small core diameter PBG guiding HC-PCF's (29,30) in terms of reduced dephasing. Both transit time and atom wall collisions give broadening contributions of comparable magnitude to the linewidth of sub Doppler features in confined HC-PCF geometries. In a HC-PCF, and for typical core diameter of 15 μm (case of Kagome HC-PCF is taken), we have $\gamma_{TT} \sim 4MHz$ and $\gamma_{walls} \sim 5MHz$. However such a small difference between the two dephasing mechanisms makes assessing the performance of antirelaxation coatings in HC-PCF using sub Doppler transparencies (16,31,32)

challenging because of the comparative strength and intrinsic link between transit time broadening and atom wall collisions. Ideally another experimental technique is required to investigate the atom wall collisions independently from the transit time broadening.

Indeed, antirelaxation coating performance has been studied extensively in vacuum pressure macroscopic alkali metal vapour cells most notably by Balabas and Budker (8,13,17,33–37), who have made outstanding contributions to the field including demonstrating minute long transverse relaxation time in alkene type coating materials (17). However, in confined dielectric geometries (16,31,32), the performance of antirelaxation coatings has been estimated from the measurement of the full width at half maximum (FWHM) of sub Doppler transparency features. To date these measurements have not clarified the performance of these antirelaxation coatings in confined hollow core waveguiding geometries. Neither has direct measurement of the longitudinal and/or transverse relaxation times in confined dielectric geometries been reported to date.

In this chapter, firstly a modified Franzen technique (36) is presented which can be used to assess the longitudinal polarisation relaxation time of atoms colliding with antirelaxation coatings inside HC-PCF free from the transit time broadening. Section 7.3 presents experimental results on the relaxation time of Rb atoms on PDMS in a 2 mm inner diameter capillary and a hypocycloidal core shape Kagome HC-PCF with inner diameter of 30 µm. Additionally an uncoated Kagome HC-PCF from the same fibre draw is characterised for comparison with the PDMS coated fibre. The results from the uncoated HC-PCF are surprising and as such lead to the assessment of the impact of the hypocycloidal core shape geometry on the relaxation time of Rb atoms within the hollow core. Finally, EIT features are generated in a PDMS coated capillary and Kagome HC-PCF, and uncoated Kagome HC-PCF to assess the transit time broadening and atom wall collisions in a single measurement.

7.3 Linear Magneto Optical Rotation

The investigation of antirelaxation coatings has been carried out utilising a variety of methods. Robinson *et al.* investigated hyperfine resonances in tetracontane coated ^{87}Rb vapour cells (38). Dicke narrowed sub Doppler resonances with full widths of 10.6 Hz were

demonstrated using these tetracontane coated cells. In 1959 Franzen used a pump probe method to investigate the relaxation time of optically pumped Rb atoms in buffer gas filled and antirelaxation coated cells (39). In Franzen's original technique circularly polarised light is used to optically pump Rb atoms. The pump light is blocked for a controllable length of time using a mechanical shutter. During this time the polarised Rb atoms are allowed to freely evolve in the dark, when the shutter opens exposing the circularly polarised light, the change in transparency can be monitored directly. Due to the evolution of the Rb atoms in the dark the measured relaxation time has only contributions from collisions with either the cell walls or the buffer gas. In 2005 Graf *et al.* proposed modifications to Franzen's original method to measure the longitudinal relaxation time of alkali metal vapours in buffer gas free paraffin coated vapour cells (36). In Franzen's original method both the longitudinal electronic polarisation $\langle S_z \rangle$ and the hyperfine population difference $\langle \vec{S} \bullet \vec{I} \rangle$ contribute to the relaxation time. However these two contributions have several mechanisms of relaxation including spin exchange collisions between atoms, electron randomising collisions with the walls and relaxation due to exchange of atoms between the cell and the reservoir (reservoir effect), hence has multiple contributions to the relaxation time.

The modified Franzen technique is a pump probe experiment whereby a strong pump beam (often circularly polarised) polarises an atomic vapour and then the decay of the spin polarisation is probed by monitoring the time dependent optical rotation (i.e. Faraday rotation) of a weak linear polarised probe beam (36). Optical pumping with circularly polarised light redistributes the populations of the Zeeman sublevels of the probed hyperfine manifold. Thus the atomic ensemble acquires orientation and alignment in the direction of light propagation. Alignment can be understood physically as the Zeeman sublevel population distribution which corresponds to zero overall magnetic moment. On the other hand orientation corresponds to a Zeeman sublevel population distribution whereby the total magnetic moment is non-zero (40). Mathematically orientation, and alignment correspond to the k = 1, 2 irreducible tensor components of the polarisation multipole moment and k = 0 component is referred to as population (41). Three different types of collision mechanisms contribute to the destruction of ground state polarisation these are 1) electron randomisation collisions with the walls, 2) spin exchange collisions between atoms and 3) uniform relaxation from the reservoir effect. In the traditional Franzen method by monitoring the absorption of circularly polarised light all multipole moments contribute to the optical rotation signal and hence it decays with multiple time constants.

Optical rotation arises from the birefringence occurring in the atomic vapour. The refractive indices ($n_{+/-}$) of right and left circularly polarised light propagating in a birefringent atomic vapour are plotted in Fig (7-2). The refractive indices are given by (42),

$$n_{-}(\upsilon)=1+2\left(\frac{3}{4}\rho(-1/2)+\frac{1}{4}\rho(+1/2)\right)\left(\frac{nr_e c^2 f_{D2}}{4\upsilon_0}\right)\mathrm{Im}(V(\upsilon-\upsilon_0))$$
$$n_{+}(\upsilon)=1+2\left(\frac{1}{4}\rho(-1/2)+\frac{3}{4}\rho(+1/2)\right)\left(\frac{nr_e c^2 f_{D2}}{4\upsilon_0}\right)\mathrm{Im}(V(\upsilon-\upsilon_0)) \quad , \qquad (7\text{-}4)$$

where ρ(-1/2), ρ(+1/2) are the ground state population densities of the spin down and up respectively and, assume a closed system i.e. ρ(-1/2) + ρ(+1/2) = 1, V(υ-υ_0) is a Voigt distribution of the atomic absorption profile, n is the atomic density, r_e is the classical electron radius, c is the speed of light, f_{D2} is the D2 absorption line oscillator strength and υ_0 is the fundamental transition frequency.

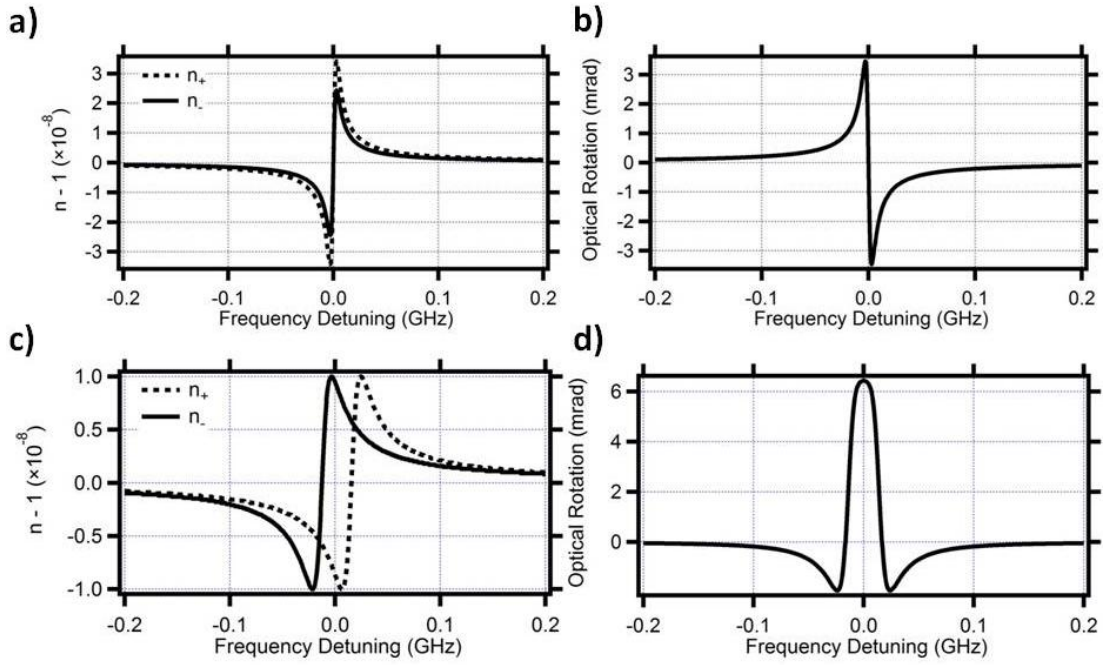

Figure (7-2) a) Refractive index (n+/-) variation near atomic resonance due to orientation in hyperfine levels in ^{85}Rb at n = 1 × 10^{12} cm^{-3}, b) optical rotation due to difference in n(+/-) from a) due to orientation in the hyperfine levels, c) Refractive index (n+/-) variation near atomic resonance due to alignment in hyperfine levels in ^{85}Rb at n = 1 × 10^{12} cm^{-3}, d) optical rotation due to difference in n(+/-) from b) due to alignment in the hyperfine levels.

In the modified Franzen technique used here, whereby the time dependent optical rotation of narrow band linearly polarised light is detected in the dark time of the pump, the signal is primarily only sensitive to orientation of the probed hyperfine level (36). Orientation in the probed hyperfine level produces optical rotation (Fig (7-2) b) of linearly polarised light because the left and right hand circular components of the light experience different phase velocities during propagation. The difference in the phase velocities arise because the real part of the complex refractive indices of left and right circular polarisations have different amplitudes (Fig (7-2) a). Optical rotation produced by population and alignment is first order dependent on the B field. The real parts of the complex indices of left and right hand circular components are now shifted in frequency (Fig (7-2) c) because of the Zeeman sublevel splitting. The difference in phase velocities gives a symmetric optical rotation response (Fig (7-2) d) (36).

In the modified Franzen technique the relaxation signals can be described using simply two time constants, as such, the interpretation of the results is straight forward. Here we coat 2 mm inner diameter borosilicate capillaries and Kagome HC-PCF with polydimethylsiloxane (PDMS) using the method discussed previously in section 5.3 and measure its antirelaxation properties for the first time in a confined dielectric geometry.

7.4 Polarisation rotation measurements in antirelaxation coated capillaries and Hypocycloidal Core Shape Kagome HC-PCF

The energy level structure of ^{85}Rb is shown in Fig (7-3) a), the pump and probe are 500 MHz detuned from D2 resonance of ^{85}Rb ($5S_{1/2}F=3\rightarrow5P_{3/2}$ F'=1, 2, 3, 4). The 7 cell 3 ring HC-PCF discussed in chapter 4 is used in these experiments (Fig (7-3) b), which is supported in a cane structure of fused silica capillaries to ensure efficient core mode coupling in the ultra high vacuum (UHV) chamber. The experimental setup shown in Fig (7-3) c) is the modified Franzen technique as detailed by Graf *et al.* (36) which is used to probe the ground state polarisation relaxation of Rb vapour confined in PDMS coated capillaries, PDMS coated Kagome HC-PCF and uncoated Kagome HC-PCF. The beam from an external cavity diode laser is linearly polarised and split into two beams using a polarising beam splitter cube. The high power pump beam is circularly polarised and cycled on and off

at a frequency of 70 Hz using a chopper wheel. The second beam is a low power probe beam below the saturation power (P_{sat} ~ 15 nW in 30 µm hollow core) with linear polarisation.

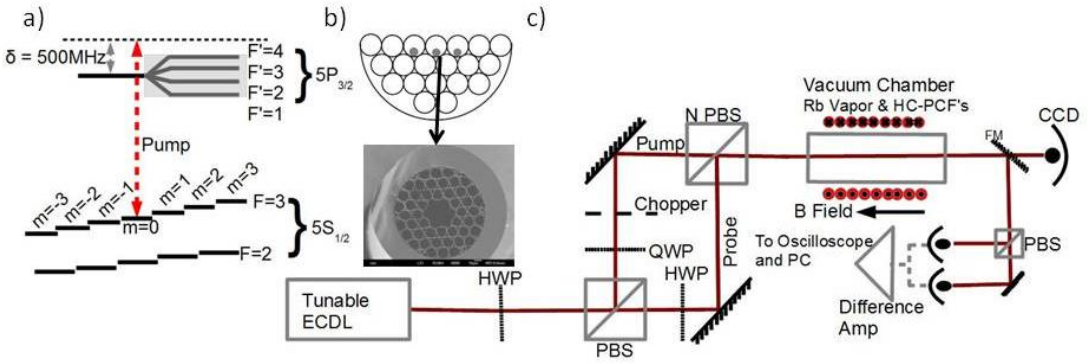

Figure (7-3) a) Rb Energy level structure, b) Cane holder for supporting HC-PCF's and capillaries in vacuum chamber, c) Experimental setup for modified Franzen method used to probe ground state polarisation relaxation. PBS-polarising beam splitter cube, QWP-quarter waveplate, HWP-half waveplate, N PBS-None polarising beam splitter cube, FM-flipper mirror.

The pump and probe beams are recombined on a non polarising beam splitter (NPBS) cube and coupled through the HC-PCF's contained in the UHV chamber. The output light can be directed to a CCD camera to ensure efficient core mode coupling or to a balanced polarimeter to measure the time dependent polarisation rotation of the linearly polarised probe beam. At the low powers used in these experiments the pump beam does not saturate the polarimeter, nor does it affect the time dependent optical rotation signal. A solenoid coil is wound round the UHV chamber provides a uniform magnetic field (< 3.5 mT) along the propagation axis of the fibres. Additionally the applied magnetic field suppresses transverse polarisation moments. The angle of polarisation rotation is given by Eq (7-5) where P_1 and P_2 are the signals from each arm of the balanced polarimeter,

$$\phi = \frac{P_1 - P_2}{2(P_1 + P_2)}. \tag{7-5}$$

Prior to doing any measurements in the Kagome HC-PCF's it is necessary to successfully load Rb vapour in the hollow core. In Fig (7-4) a) the atomic density evolution in the UHV chamber and the PDMS coated 7 cell Kagome HC-PCF are shown. The atomic density is measured by monitoring the on resonance transmission of a weak probe beam and knowing the atomic cross section, cell temperature and sample length, hence $n = -\frac{1}{\sigma z}\ln(1-A)$ (43).

Where σ is the atomic scattering cross section, z is the interaction length, A=1-Tr and here Tr is the relative transmission.

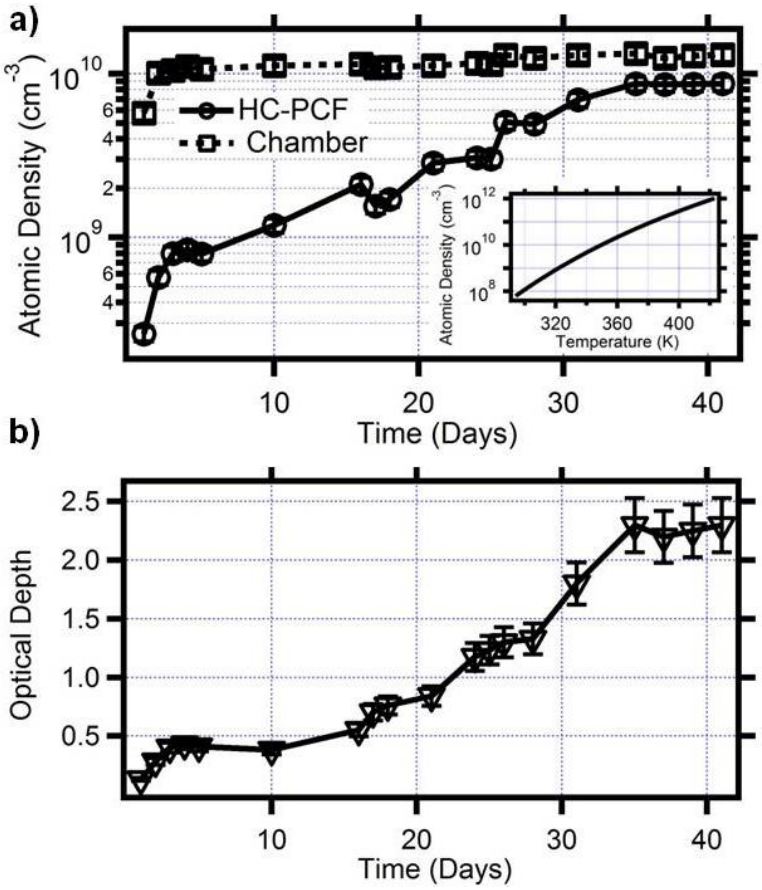

Figure (7-4) a) Atomic density evolution in Kagome HC-PCF (black circles) and the UHV chamber (black squares) (Inset: Atomic density evolution with temperature), b) Optical depth evolution in Kagome HC-PCF.

The atomic density in the UHV chamber rapidly increases to a steady state value of 1.0 ± 0.1×10^{10} cm^{-3}. While the atomic density in the HC-PCF increases steadily to 7.0 ± 0.5×10^{9} cm^{-3} over a period of 35 days. The corresponding optical depth (OD = -ln (T), where T is the transmission) (Fig (7-4) b) in the same 7 cell Kagome HC-PCF is shown to increase to OD ~ 2.2 over a period of 35 days before it stabilises. This is indicative of Rb vapour loading in the hollow core.

Polarisation rotation relaxation measurements for 2% PDMS coated borosilicate capillary are shown in Fig (7-5). The ground state polarisation (GSP) relaxation time is extracted by fitting the raw polarisation rotation signal with an exponential and extracting the time constant.

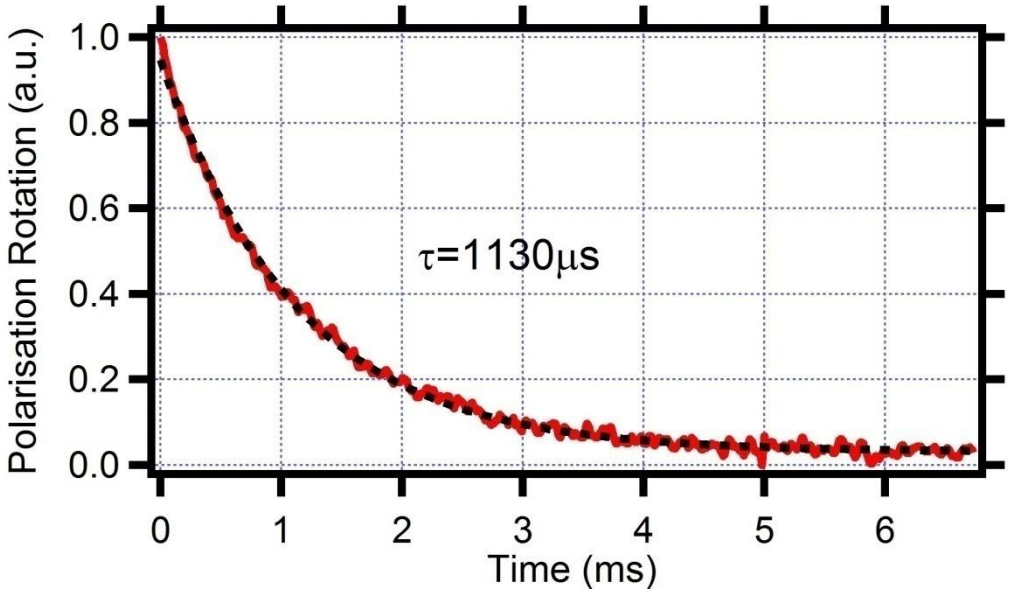

Figure (7-5) Polarisation rotation measurement in 2mm inner diameter PDMS coated capillary. (Red- experimental data, dashed black- exponential fitting)

The GSP relaxation time for Fig (7-5) is 1130 ± 10 μs which when converted to a number of effective bounces gives an estimate number of ~94 wall collisions. The number of bounces was deduced by considering the time taken for an atom with the average thermal velocity of the ensemble to traverse the hollow core, one can calculate the number of atom wall collisions before relaxation. The time to traverse the hollow core is given by $t_{core} = d_{core}/v_{thermal}$, where d_{core} is the diameter of the hollow core and $v_{thermal}$ is the thermal velocity, $v_{thermal} = \sqrt{8k_B T/\pi m}$. The value found here for a capillary is qualitatively comparable with the value of 450 collisions reported for OTS in (44). The discrepancy between these two values can be due to a combination of reasons such as the difference in coating materials, the difference in wall geometry of the host structure, and to the quality of the coating layer.

The polarisation rotation signal for Rb vapour confined in the core of a PDMS coated hypocycloid core shape Kagome HC-PCF is shown in Fig (7-6) a). The GSP relaxation time for the PDMS coated HC-PCF is 31 μs as shown in Fig (7-6) a). Multiple repeat measurements for the same experimental conditions for a PDMS coated and uncoated Kagome HC-PCF are shown in Fig (7-6) b).

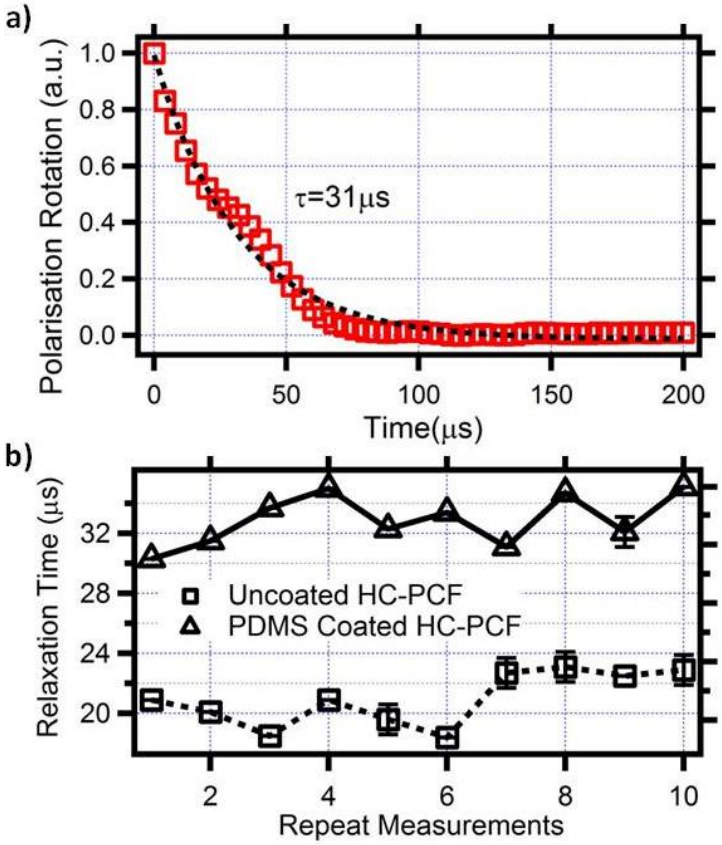

Figure (7-6) a) Polarisation rotation in PDMS coated HC-PCF (Experimental data-red squares, exponential fitting-black dashed), b) repeat measurements of relaxation time in PDMS coated (black triangles) and uncoated HC-PCF(black squares) (45,46)**.**

The average GSP relaxation time for PDMS coated and uncoated Kagome HC-PCF are 32 μs and 20 μs respectively. These relaxation times correspond to a number of bounces before dephasing of 240 for coated fibre and 170 for uncoated fibre. This number of wall collisions for the uncoated HC-PCF is much greater than prior works which have shown uncoated glass surfaces have a maximum of 1 (14) or 2 (47) atom-wall collisions. However, in these prior works, the cells are macroscopic and the dielectric surface thickness is of the order 1 – 2 mm. In the PhD thesis of Seltzer (42) less than 10 atom wall collisions are reported for uncoated glass substrates, and the results show a qualitative dependence of the measured bounce-number with the thickness of the wall. In the absence of prior knowledge on the number of bounces upon a nanometre and micrometre-scale dielectric surfaces (in our case the capillary wall thickness was ~ 320 nm) an Rb atom has to go through before it dephases, we take our measured 170 bounces as the reference figures for uncoated HC-PCF.

A comparison of the bounces between the coated and the uncoated HC-PCF indicates that PDMS coating does have a minor impact upon the relaxation of Rb vapour in a HC-PCF

allowing a single additional wall collision before dephasing compared to an uncoated silica surface. Such a low increase in antirelaxation could be due to the small thickness of the coating and/or the quality of the coating surface. Investigating both parameters of the coating is planned for future work and is beyond the scope of the present work. In parallel, and for comparison an uncoated silica capillary with circular geometry and core diameter of ~ 950 µm and a wall thickness ~ 150 µm loaded with Rb vapour has a measured GSP relaxation time ~ 55 µs corresponding to ~ 18 atom-wall collisions. Additionally it is speculated that the geometry of the hypocycloidal core shape results in longer than expected atom trajectories outside of the optical mode profile. We will show that the hypocycloidal core provides greater mode confinement away from the silica core boundaries and the geometrical shape allows for numerous atom wall collisions without returning to the centre of the hollow core.

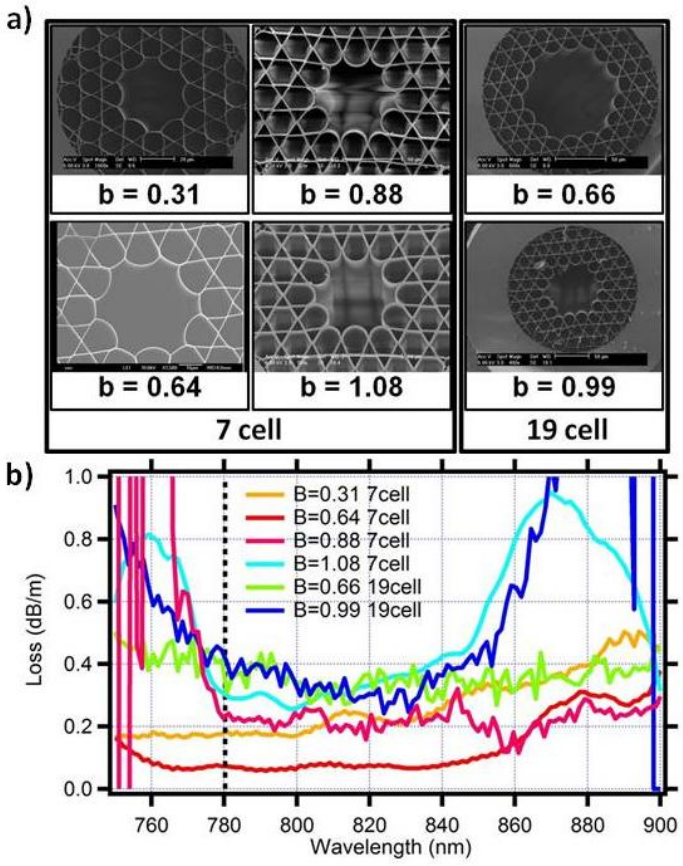

Figure (7-7) a) Scanning electron micrographs of different arc curvature (b) values, b) Optical loss spectrum of Kagome HC-PCF with different curvature values.

Given that this is the first time that hypocycloid core shape Kagome HC-PCF has been used for Rb vapour loading experiments, it is beneficial to assess the impact of the hypocycloid

geometry on the relaxation time of Rb atoms confined in the hollow core. Hence a detailed investigation of the impact of the hypocycloid curvature on the ground state polarisation relaxation time of Rb vapour in hypocycloid core shape Kagome HC-PCF became imperative. For this investigation four different 7 cell and two different 19 cell 3 ring Kagome HC-PCF's (Fig (7-7) a) with guidance optimised for 780 nm (Fig (7-7) b) but with different curvature parameters (b - see chapter 4 for definition) of the hypocycloidal core were inserted in the UHV chamber and loaded with Rb vapour.

Table (7-1) Properties of Hypocycloid Kagome HC-PCF

Core Defect	Curvature Parameter (b)	Inner Diameter (μm)	PER (dB)
19 cell	0.66	76	5.8
19 cell	0.99	96	10.4
7 cell	0.31	30	3.0
7 cell	0.64	33	7.0
7 cell	0.88	51	7.3
7 cell	1.08	59	7.6

The physical parameters of the 6 different hypocycloid core shape Kagome HC-PCF utilised in this study are summarised in table (7-1). Additionally for completeness the polarisation extinction ratio (PER) of the different Kagome HC-PCF are given in table (7-1). The GSP relaxation times (Fig (7-9)) were measured in the different curvature HC-PCF's utilising the modified Franzen method outlined previously. Fig (7-9) demonstrates a small linear increase of the measured GSP relaxation time with increasing hypocycloid core curvature in both the 7 and 19 cell core defect Kagome HC-PCF's. It is proposed that the greater curvature parameter (b) of the hypocycloid contour results in more atom-wall collisions before the atom returns to the optical mode area which is confined by the inward most tangential cusps, where the polarisation decay is probed. This hypothesis is corroborated via Monte-Carlo simulations of the atomic trajectories in hypocycloid Kagome HC-PCF with varying curvature parameters, a brief description of the model is given below.

As it was discussed above the polarization rotation signal is caused by the difference in populations of ground state Zeeman sublevels, provided by optical pumping. Each collision of the atom with the wall can lead to spontaneous change of its state. In the absence of pump laser the atoms gradually via collisions with the walls become thermally distributed between Zeeman sublevels and the polarization rotation signal ceases. In the theoretical model described below we associate the pumped population with the pseudo-spin value $S = 0, 1$.

We assume that initially each atom is prepared in the chosen Zeeman state which corresponds to $S = 1$. In case of the spontaneous change of the state the spin drops to zero, $S = 0$. The probability of the polarization being lost due to the single collision P_{scpl} is the model free parameter. The atomic velocity vector stochastically changes after each collision with the wall. Each time the absolute value of the velocity is the probabilistic value obeying the Maxwell distribution. Monte Carlo simulations were used (with 20000 realizations) to obtain the time dependence of the average polarization in ensemble. We calculated the lifetimes of the polarization in the volume and the effective polarization in the interaction volume. The last should be understood as follows. The atoms interact with the probe beam only when they are in the modal area, which is about $3/4R_{in}$, where R_{in} is the internal radius of the fibre. In Monte Carlo simulations (Fig (7-8)), to fit with experimental parameters the polarisation probability parameter is set to $P_{SCPL} = 0.006$ (42).The results of the Monte Carlo simulations mapping the atomic trajectories are summarised in the contour plot of Fig (7-8) a).

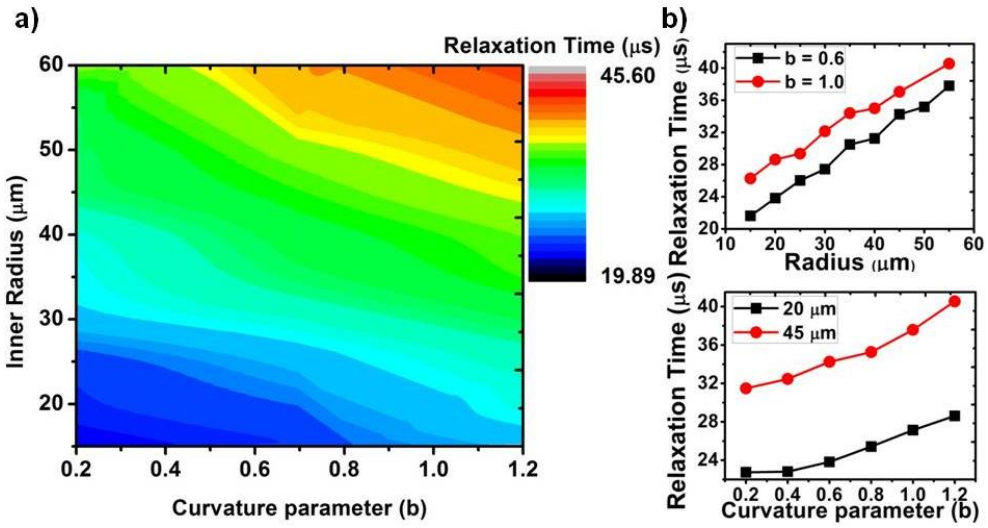

Figure (7-8) a) Contour plot of relaxation time as a function of both hollow core radius and hypocycloid curvature. b) Relaxation time as a function of radius for fixed arc curvature (upper) and relaxation time versus arc curvature for fixed hollow core radius (lower)[4].

The over arching trend is summarised in the two panels of Fig (7-8) b). In the upper panel the GSP relaxation time demonstrates the expected linear evolution (3) with core radius for two fixed values of the curvature parameter. The lower panel demonstrates the new trend of increasing relaxation time versus hypocycloid curvature parameter for a fixed radius. This trend is similar to that which was speculated for hypocycloid core Kagome HC-PCF and gives rise to a longer than expected relaxation time. Hence this result supports the idea of a

[4] Acknowledgement: Monte Carlo Simulations performed by Ekaterina Illinova.

geometrical contribution from the hypocycloid curvature to the relaxation time of the Rb vapour.

Experimental results for the GSP relaxation time of Rb vapour in 7 cell and 19 cell (black squares in Fig (7-9) a)) demonstrates a small linear increase with increasing hollow core inner radius. Monte Carlo simulations with P_{SCPL} = 0.006 of the atomic trajectories demonstrate excellent agreement with the experimental results (dashed black). The relaxation time increases (Fig (7-9) a) from ~ 17 μs to ~ 35 μs with increasing hollow core diameter (30 μm – 96 μm) (46). Additionally the relaxation time is plotted against the hypocycloid curvature parameter, b (Fig (7-9) b) to demonstrate the increasing relaxation time with core curvature.

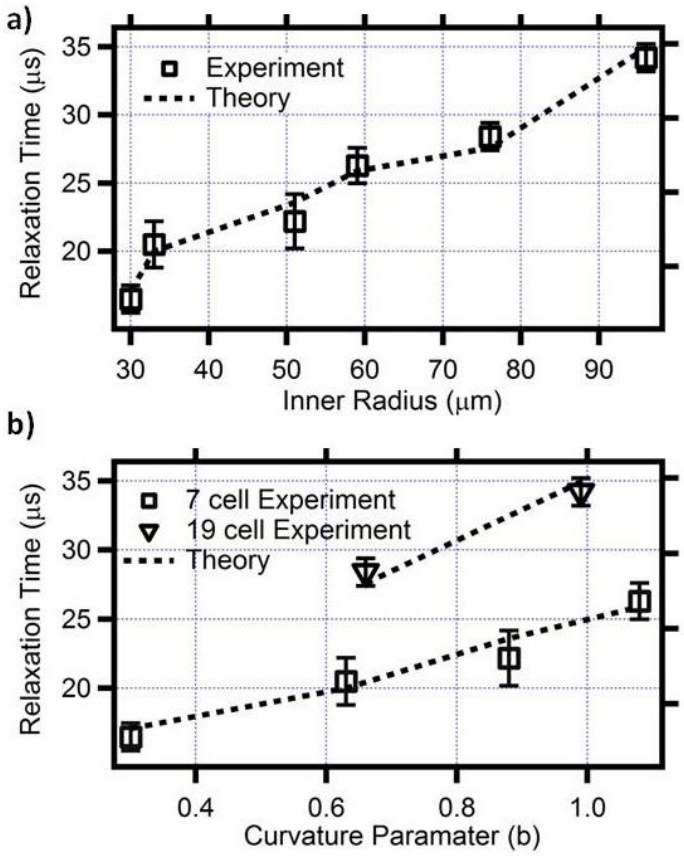

Figure (7-9) a) GSP Relaxation time in hypocycloidal core Kagome HC-PCF with inner core radius, (black squares-experimental results for 7 and 19 cell core defect Kagome HC-PCF), and black dashed line and are theoretical results for 7 and 19 cell core defect Kagome HC-PCF. b) GSP relaxation time (as in a) but plotted against hypocycloid curvature parameter, b (7 cell – black squares, 19 cell – black triangles, Monte Carlo simulations – dashed black).

Both of these trends were observed in Monte Carlo simulations of the atomic trajectories and strong agreement can be observed with the theoretical results in both Fig (7-9) a) & b). The strong correlation of experiment and theory allows for the assessment of the impact of the

hypocycloid curvature on the relaxation time. It appears that while the hypocycloid curvature does have an impact upon the relaxation time as demonstrated by theoretical and experimental results, its impact is minor allowing approximately twice as many atom wall collisions when the curvature parameter is increased from 0.31 to 1.08.

7.5 EIT Measurements in antirelaxation coated capillaries and Hypocycloidal Core Shape Kagome HC-PCF

The experimental set-up used to observe EIT in Rb vapour loaded PDMS coated and uncoated HC-PCF's is shown in Fig (7-10) a). Two external cavity diode lasers (ECDL) are coupled through the HC-PCF's under test. The first ECDL acts as a weak probe beam and has its frequency scanned across the $^{85}Rb\ 5S_{1/2}\ F=3 \rightarrow 5P_{3/2}\ F'= 2, 3, 4$ energy level as seen in Fig (7-10) b).

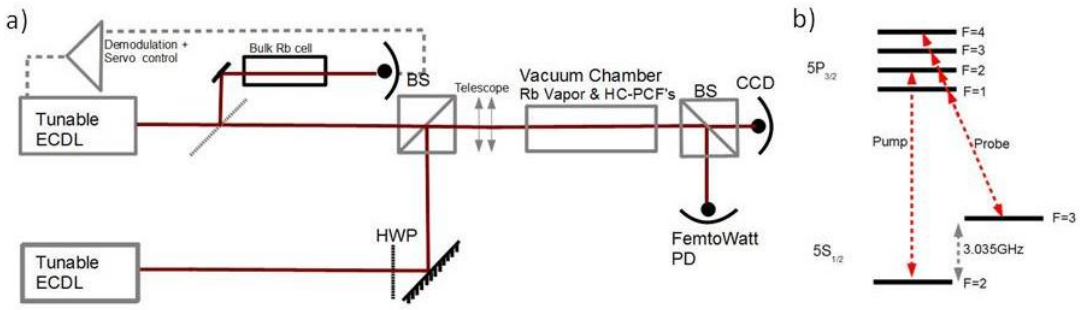

Figure (7-10) a) Experimental setup for observing EIT in RB loaded coated and uncoated capillaries and HC-PCF, b) Rb energy level structure probed for EIT experiments

The second ECDL acts as the strong coupling beam and couples the $^{85}Rb\ 5S_{1/2}F=2 \rightarrow 5P_{3/2}$ F'= 2 energy level (Fig (7-10) b). At the output of the HC-PCF's a CCD camera is used to ensure good core mode coupling of both lasers and a femtowatt photodiode connected to an oscilloscope is used to record the EIT features. Initially EIT features were demonstrated in a 2% PDMS coated 2 mm inner diameter borosilicate capillary as seen in Fig (7-11) a).

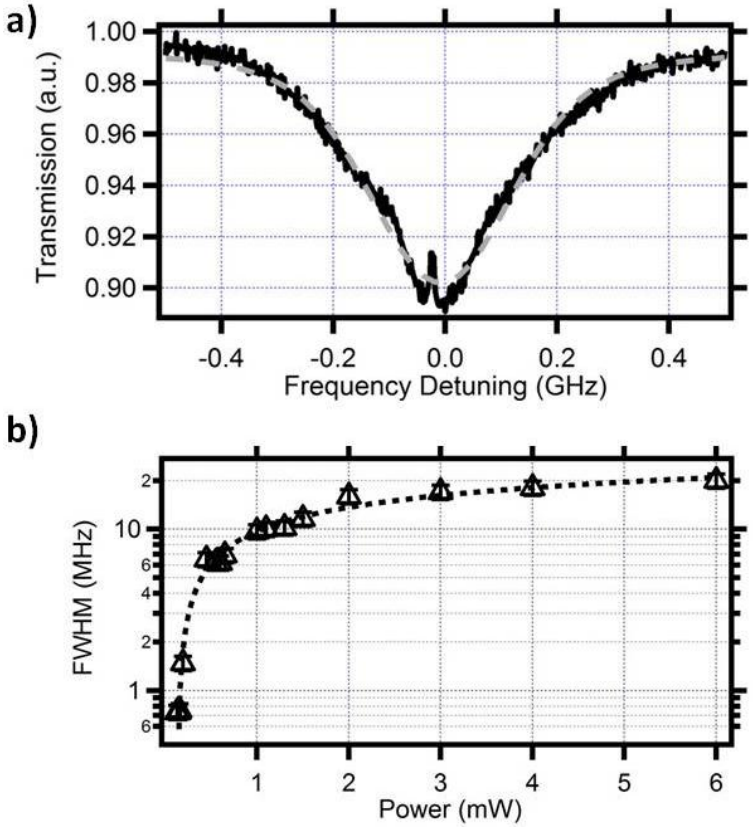

Figure (7-11) a) EIT trace observed in 2% PDMS coated capillary (solid black). Gaussian fit to the Doppler broadened ^{85}Rb $5S_{1/2}$ F=3→$5P_{3/2}$ F'= 2, 3, 4, b) EIT FWHM evolution with pump power in 2% PDMS coated capillary.

Fitting the Doppler broadened absorption line to a Voigt distribution (dashed grey curve in Fig (7-11) a) the Doppler FWHM is estimated ~ 330 MHz. It is speculated that the experimental data distortion around the EIT resonance from the Voigt distribution is due to optical pumping. A 2% PDMS coating is used because it gives approximately similar coating thickness to that estimated in the Kagome HC-PCF's (t_{PDMS} ~ 100 nm). The evolution of the EIT FWHM with coupling laser power is shown in Fig (7-11) b). Typical EIT power broadening behaviour can be observed; where the FWHM decreases as the coupling laser power is reduced (48–50). A minimum EIT FWHM of ~750 ± 80 kHz is observed for a coupled power of 150 µW (corresponding to an intensity of 7.7 mW/cm^2, 5.5 times the saturation intensity). As the coupled power increase the FWHM plateaus towards 20 MHz. The transit time broadening given by Eq (7-1) gives a value of ~100 kHz for an experimentally measured beam diameter of 0.5 mm which is significantly below the minimum observed linewidth of 750 ± 80 kHz. Below the power levels used in these experiments the EIT feature cannot be observed.

EIT is investigated in ^{85}Rb (Fig (7-10) b) loaded in PDMS coated and uncoated hypocycloid core shape Kagome HC-PCF. A minimum FWHM of 10.9 ± 0.9 MHz is observed in uncoated HC-PCF for a coupling power of ~ 6.0 nW (intensity of 1.4 mW/cm^2) and probe power of 180 pW (intensity of 0.04 mW/cm^2) shown in Fig (7-12) a). In the PDMS coated HC-PCF a minimum EIT FWHM of 6.2 ± 0.8 MHz (Fig (7-12) b) is observed for the same coupled pump and probe powers.

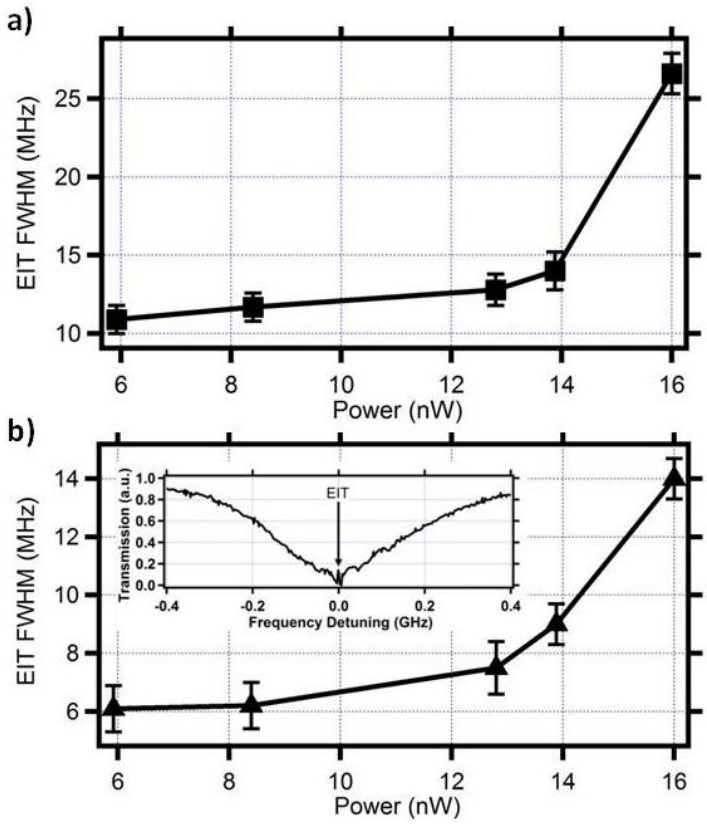

Figure (7-12) EIT FWHM evolution with control field power in a) uncoated HC-PCF (black squares) and b) PDMS coated HC-PCF (black triangles). Inset: EIT feature in Doppler broadened absorption line confined in PDMS coated HC-PCF.

Both sets of experimental data (coated and uncoated) shown in Fig (7-12) a) and b) respectively, demonstrate typical EIT linewidth power broadening as the control field power is increased (48,50,51). The linewidth measurements are made on the time scale of ~5 ms. A minimum EIT linewidth of 6.2 ± 0.8 MHz is observed in PDMS coated HC-PCF which is consistent with the transit time broadening given by Eq (7-1) and the laser linewidths used in these experiments. The transit time broadening is ~ 4 MHz from Eq (7-1) for the geometry of the HC-PCF used in this work. The two external cavity diode lasers have a linewidth of ~1 MHz each, giving a total broadening contribution of ~6 MHz. This is in good quantitative agreement with the experimental result and within the experimental uncertainty of the FWHM measured in the PDMS coated Kagome HC-PCF. The minimum EIT linewidth of

10.9 ± 0.9 MHz in the uncoated HC-PCF is slightly above the minimum expected value (from transit time broadening and laser linewidths) implying that some additional dephasing mechanism is contributing to the total EIT linewidth. The additional spectral broadening of the EIT feature in an uncoated HC-PCF can be accounted for by considering Fig (7-1) where the transit time and atom-wall collision broadening are plotted. Considering the core radius of 15 μm of the HC-PCF used here the broadening contribution to the linewidth from atom-wall collisions (Fig (7-1)) is ~ 5 MHz. This accounts for the linewidth difference of the EIT features, $\Delta_{Difference} = \delta^{EIT}_{Uncoated} - \delta^{EIT}_{PDMS} = 4.7MHz = \gamma_{walls}$, between PDMS coated and uncoated Kagome HC-PCF's. The reduction of the EIT linewidth by the 5 MHz corresponds to the atom wall broadening contribution, thus demonstrates the effectiveness of PDMS coating in a Kagome HC-PCF to at least reducing the EIT linewidth to transit-time limit.

7.6 Summary

In the first part of this chapter, measurements of the GSP relaxation time for PDMS coated capillaries and, PDMS coated and uncoated Kagome HC-PCF's are presented. This is the first time such measurements have been achieved in confined dielectric waveguiding geometries giving us a means to quantify the performance of antirelaxation coatings on the micron scale and distinguish their impact from that of transit time broadening. GSP relaxation times of 32 μs and 20 μs were measured in PDMS coated and uncoated HC-PCF's respectively, corresponding to approximately 240 and 170 effective collisions. It is proposed that the hypocycloidal geometry of the core gives rise to extended atom trajectories outside of the guided optical mode and hence gives longer than expected GSP relaxation times. The geometrical factor introduced by the hypocycloidal geometry is demonstrated experimentally by studying the atomic polarisation relaxation time in Kagome HC-PCF's with different core curvature parameters, b. Relaxation times are increased two fold in hypocycloid curvature Kagome HC-PCF when the core diameter increase from ~ 30 μm to ~ 96 μm. Monte-Carlo simulations of atomic trajectories in hypocycloid core shapes demonstrate remarkable agreement with the observed experimental results.

The latter part of this chapter is given over to the discussion of EIT features in both PDMS coated capillaries and Kagome HC-PCF, and uncoated Kagome HC-PCF. EIT features are investigated as a function of coupling field power with typical power broadening behaviour

observed, a minimum transparency linewidth of 750 ± 80 kHz is observed in a PDMS coated capillary with inner diameter of 2 mm. In PDMS coated and uncoated HC-PCF's a minimum EIT linewidth of 6.2 ± 0.8 MHz and 10.9 ± 0.9 MHz are measured respectively. The minimum linewidth observed in the PDMS coated HC-PCF agrees quantitatively with the limit set by the transit time broadening combined with the linewidths of the two laser sources used to generate the transparency. The additional broadening in the uncoated HC-PCF is dominated by atom wall collisions.

Future work will focus on depositing different coating materials on the inner core wall such as alkene based coatings, with the aim of observing longer atomic polarisation relaxation times using the modified Franzen technique. By incorporating a length of Rb vapour loaded Kagome HC-PCF into a photonic microcell it should be possible to make a compact, sensitive and portable magnetometer. Sub Doppler feature generation in HC-PCF's will focus on using larger core 19 cell defect Kagome HC-PCF's where hollow core diameters up to 100 μm can be fabricated (52). Utilising a Kagome HC-PCF with a hollow core this large reduces the transit time broadening ~ 1 MHz; as such narrower sub Doppler features should be achievable. The possibility exists to then use such narrow sub Doppler features to frequency stabilise lasers utilising both frequency modulation stabilisation and diachroic atomic vapour laser locking (DAVLL).

References

1. Happer W. Optical Pumping. Reviews of Modern Physics. 1972;44(2):169–222.

2. Bouchiat MA, Brossel J. Relaxation of Optically Pumped Rb Atoms on Paraffin-Coated Walls. Physical Review. 1966;147(1).

3. Franz A. Relaxation at Cell Walls in Optical-Pumping Experiments. Physical Review A. 1972;6(5):1921–5.

4. Vanier J, Simard J-F, Boulanger J-S. Relaxation and frequency shift in the geound state of Rb 85. Physical Review A. 1974;9(3).

5. Klein M, Hohensee M, Phillips DF, Walsworth RL. Electromagnetically induced transparency in paraffin-coated vapor cells. Physical Review A [Internet].

2011 Jan [cited 2013 Feb 13];83(1):013826. Available from: http://link.aps.org/doi/10.1103/PhysRevA.83.013826

6. Bandi T, Affolderbach C, Mileti G. Laser-pumped paraffin-coated cell rubidium frequency standard. Journal of Applied Physics [Internet]. 2012;111(12):124906. Available from: http://link.aip.org/link/JAPIAU/v111/i12/p124906/s1&Agg=doi

7. Budker D, Yashchuk V, Zolotorev M. Nonlinear Magneto-optic Effects with Ultranarrow Widths. Physical Review Letters [Internet]. 1998 Dec;81(26):5788–91. Available from: http://link.aps.org/doi/10.1103/PhysRevLett.81.5788

8. Budker D, Kimball D, Rochester S, Yashchuk V, Zolotorev M. Sensitive magnetometry based on nonlinear magneto-optical rotation. Physical Review A [Internet]. 2000 Sep;62(4):043403. Available from: http://link.aps.org/doi/10.1103/PhysRevA.62.043403

9. Klein M, Novikova I, Phillips DF, Walsworth RL. Slow light in paraffin-coated Rb vapour cells. Journal of Modern Optics [Internet]. 2006 Nov 10 [cited 2013 Aug 14];53(16-17):2583–91. Available from: http://www.tandfonline.com/doi/abs/10.1080/09500340600952135

10. Kuzmich a, Mandel L, Bigelow N. Generation of spin squeezing via continuous quantum nondemolition measurement. Physical review letters [Internet]. 2000 Aug 21;85(8):1594–7. Available from: http://www.ncbi.nlm.nih.gov/pubmed/10970566

11. Julsgaard B, Sherson J, Cirac JI, Fiurásek J, Polzik ES. Experimental demonstration of quantum memory for light. Nature [Internet]. 2004 Nov 25;432(7016):482–6. Available from: http://www.ncbi.nlm.nih.gov/pubmed/15565148

12. Brewer RG. Study of Atom—Wall Collisions by Optical Pumping. The Journal of Chemical Physics [Internet]. 1963 [cited 2013 Apr 23];38(12):3015. Available from: http://link.aip.org/link/JCPSA6/v38/i12/p3015/s1&Agg=doi

13. Yi YW, Robinson HG, Knappe S, Maclennan JE, Jones CD, Zhu C, et al. Method for characterizing self-assembled monolayers as antirelaxation wall coatings for alkali vapor cells. Chemical Analysis. 2008;1–7.

14. Seltzer SJ, Romalis M V. High-temperature alkali vapor cells with antirelaxation surface coatings. Journal of Applied Physics [Internet]. 2009 [cited 2013 Feb 13];106(11):114905. Available from: http://link.aip.org/link/JAPIAU/v106/i11/p114905/s1&Agg=doi

15. Kessel CR, Granick S. Formation and Characterization of a Highly Ordered and Well- Anchored Alkylsilane Monolayer on Mica by Self -Assembly. Langmuir. 1991;7(9):532–8.

16. Light PS, Benabid F, Couny F, Maric M, Luiten a N. Electromagnetically induced transparency in Rb-filled coated hollow-core photonic crystal fiber. Optics letters [Internet]. 2007 May 15;32(10):1323–5. Available from: http://www.ncbi.nlm.nih.gov/pubmed/17440575

17. Balabas M, Karaulanov T, Ledbetter M, Budker D. Polarized Alkali-Metal Vapor with Minute-Long Transverse Spin-Relaxation Time. Physical Review Letters [Internet]. 2010 Aug [cited 2013 Jan 30];105(7):070801. Available from: http://link.aps.org/doi/10.1103/PhysRevLett.105.070801

18. Shuker M, Firstenberg O, Sagi Y, Ben-kish A, Davidson N, Ron A. Ramsey-like measurement of the decoherence rate between Zeeman sublevels. Physical Review A [Internet]. 2008 Dec [cited 2013 Sep 5];78(6):063818. Available from: http://link.aps.org/doi/10.1103/PhysRevA.78.063818

19. Demtroder W. Laser Spectroscopy Vol. 1. 4 th. New York: Springer; 2008. p. 468.

20. Demtroder W. Laser Spectroscopy Vol. 2: Experimental Techniques. Fourth. New York: Springer; 2008.

21. Gallagher a., Lewis EL. Determination of the vapor pressure of rubidium by optical absorption. Journal of the Optical Society of America [Internet]. 1973 Jul 1;63(7):864. Available from: http://www.opticsinfobase.org/abstract.cfm?URI=josa-63-7-864

22. Weller L, Bettles RJ, Siddons P, Adams CS, Hughes IG. Absolute absorption on rubidium D 1 line: including resonant dipole-dipole interactions. Journal of Physics B: Atomic, Molecular and Optical Physics. 2011;44(195006):1–5.

23. Kondo R, Tojo S, Fujimoto T, Hasuo M. Shift and broadening in attenuated total reflection spectra of the hyperfine-structure-resolved D_{2} line of dense rubidium vapor. Physical Review A [Internet]. 2006 Jun [cited 2013 Sep 28];73(6):062504. Available from: http://link.aps.org/doi/10.1103/PhysRevA.73.062504

24. Bhagwat AR. LOW-LIGHT-LEVEL NONLINEAR OPTICS WITH RUBIDIUM ATOMS IN HOLLOW-CORE PHOTONIC BAND-GAP FIBERS. 2010. p. 1–102.

25. Shimoda K. 2 . Line Broadening and Narrowing Effects. High Resolution Laser Spectroscopy. New York: Springer-Verlag; 1964. p. 11–49.

26. Haverkort JEM, Werij, H G C and Woerdman JP. Numerical study of light-induced drift of Na in noble gases. Physical Review A. 1988;38(8).

27. Cussler EL. Diffusion: Mass Transfer in Fluid Systems. Third. Cambridge University Press; 2009. p. 647.

28. Steck DA. Rubidium 85 D Line Data. 2001. p. http://steck.us/alkalidata.

29. Wheeler N V, Grogan MDW, Light PS, Couny F, Birks T a, Benabid F. Large-core acetylene-filled photonic microcells made by tapering a hollow-core photonic crystal fiber. Optics letters [Internet]. 2010 Jun 1;35(11):1875–7. Available from: http://www.ncbi.nlm.nih.gov/pubmed/20517447

30. Wheeler NV. Molecular and Atomic Confinement in Large Core Photonic Microcells for Slow Light and Laser Metrology Applications. Bath; 2010.

31. Ghosh S, Bhagwat A, Renshaw C, Goh S, Gaeta A, Kirby B. Low-Light-Level Optical Interactions with Rubidium Vapor in a Photonic Band-Gap Fiber. Physical Review Letters [Internet]. 2006 Jul [cited 2013 Feb 13];97(2):023603. Available from: http://link.aps.org/doi/10.1103/PhysRevLett.97.023603

32. Wu B, Hulbert JF, Lunt EJ, Hurd K, Hawkins AR, Schmidt H. Slow light on a chip via atomic quantum state control. Nature Publishing Group; 2010;4(November):5–8. Available from: http://dx.doi.org/10.1038/nphoton.2010.211

33. Seltzer SJ, Michalak DJ, Donaldson MH, Balabas M V, Barber SK, Bernasek SL, et al. Investigation of antirelaxation coatings for alkali-metal vapor cells using surface science techniques. The Journal of chemical physics [Internet]. 2010 Oct 14 [cited 2013 Feb 13];133(14):144703. Available from: http://www.ncbi.nlm.nih.gov/pubmed/20950026

34. Balabas M V., Karuzin MI, Pazgalev a. S. Experimental investigation of the longitudinal relaxation time of electronic polarization of the ground state of potassium atoms in a cell with an antirelaxation coating on the walls. Journal of Experimental and Theoretical Physics Letters [Internet]. 1999 Aug;70(3):196–200. Available from: http://www.springerlink.com/index/10.1134/1.568152

35. Budker D, Hollberg L, Kimball D, Kitching J, Pustelny S, Yashchuk V. Microwave transitions and nonlinear magneto-optical rotation in anti-relaxation-coated cells. Physical Review A [Internet]. 2005 Jan [cited 2013 Feb 13];71(1):012903. Available from: http://link.aps.org/doi/10.1103/PhysRevA.71.012903

36. Graf M, Kimball D, Rochester S, Kerner K, Wong C, Budker D, et al. Relaxation of atomic polarization in paraffin-coated cesium vapor cells. Physical Review A [Internet]. 2005 Aug [cited 2012 Mar 23];72(2):25–8. Available from: http://link.aps.org/doi/10.1103/PhysRevA.72.023401

37. Corsini EP, Karaulanov T, Balabas M, Budker D. Hyperfine frequency shift and Zeeman relaxation in alkali-metal-vapor cells with antirelaxation alkene coating. Physical Review A [Internet]. 2013 Feb [cited 2013 Mar 1];87(2):022901. Available from: http://link.aps.org/doi/10.1103/PhysRevA.87.022901

38. Robinson HG. Narrow 87Rb hyperfine-structure resonances in an evacuated wall-coated cell. Applied Physics Letters [Internet]. 1982 [cited 2013 Feb 13];40(9):771. Available from: http://link.aip.org/link/?APL/40/771/1&Agg=doi

39. Franzen W. Spin Relaxation of Optically Aligned Rubidium Vapor. Physical Review. 1959;115(4).

40. Skrotskii G V, Izyumova TG. Optical orientation of atoms and its applications. Soviet Physics Uspekhi. 1961;4(2):177–203.

41. Budker D, Fizyki I, Smoluchowskiego M, Jagiellon U, Weis A. Resonant nonlinear magneto-optical effects in atoms *. Reviews of Modern Physics. 2002;74(October).

42. Seltzer SJ. Developments in Alkali-Metal Atomic Magnetometry. 2008.

43. Petersen M. Laser-cooling of neutral Mercury and Laser-spectroscopy of the 1S0 - 3P0 transition. 2009. p. 1–156.

44. Seltzer SJ, Rampulla DM, Rivillon-Amy S, Chabal YJ, Bernasek SL, Romalis M V. Testing the effect of surface coatings on alkali atom polarization lifetimes. Journal of Applied Physics [Internet]. 2008 [cited 2013 Feb 13];104(10):103116. Available from: http://link.aip.org/link/JAPIAU/v104/i10/p103116/s1&Agg=doi

45. Bradley T, McFerran JJ, Jouin J, Benabid F, Thomas P, Ilinova E. Atomic polarization relaxation time measurement of Rb filled hypocycloidal core shape Kagome HC-PCF. Cleo: 2013 [Internet]. San Jose: Osa; 2013. p. CM3I.8. Available from: http://www.opticsinfobase.org/abstract.cfm?URI=CLEO_SI-2013-CM3I.8

46. Bradley TD, McFerran JJ, Jouin J, Ilinova E, Thomas P, Benabid F. Progress towards atomic vapor photonic microcells: Coherence and polarization relaxation measurements in coated and uncoated HC-PCF. In: Shahriar SM, Narducci FA, editors. SPIE [Internet]. 2013 [cited 2013 Apr 26]. p. 86360J–86360J–9. Available from: http://proceedings.spiedigitallibrary.org/proceeding.aspx?doi=10.1117/12.2013177

47. Camparo JC. Alkali <I.S> wall relaxation in dichlorodimethylsilane coated resonance cells. The Journal of Chemical Physics [Internet]. 1987 [cited 2013 Feb 13];86(3):1533. Available from: http://link.aip.org/link/JCPSA6/v86/i3/p1533/s1&Agg=doi

48. Akulshin AM, Sautenkov VA, Velichansky VL, Zibrov AS. POWER BROADENING OF SATURATION A B S O R P T I O N R E S O N A N C E ON THE D2 LINE OF RUBIDIUM. Optics Communications. 1990;77(4):30–3.

49. Vanier J, Levine MW, Janssen D, Delaney MJ. On the use of intensity optical pumping and coherent population trapping techniques in the implementation of atomic frequency standards. IEEE Transactions on Instrumentation and

Measurement [Internet]. 2003 Jun;52(3):822–31. Available from: http://ieeexplore.ieee.org/lpdocs/epic03/wrapper.htm?arnumber=1213668

50. Vanier J, Levine M, Janssen D, Delaney M. Contrast and linewidth of the coherent population trapping transmission hyperfine resonance line in ^{87}Rb: Effect of optical pumping. Physical Review A [Internet]. 2003 Jun [cited 2013 Feb 13];67(6):065801. Available from: http://link.aps.org/doi/10.1103/PhysRevA.67.065801

51. Zanon-willette T. Ultrahigh-resolution spectroscopy with atomic or molecular dark resonances : Exact steady-state line shapes and asymptotic profiles in the adiabatic pulsed regime. Physical Review A. 2011;062502:1–17.

52. Cheng Y, Wang Y, Auguste JL, Gerome F, Humbert G, Blondy JM, et al. Fabrication and characterization of ultra-large core size (100 m) Kagome fiber for laser power handling. CLEO 2011 [Internet]. IEEE Computer Society; 2011. p. 15–6. Available from: http://opus.bath.ac.uk/25835/

Chapter 8

Saturable absorption transparency features in Rb vapour confined in hypocycloid core shape Kagome HC-PCF

This chapter reports on the observation of saturable absorption transparencies in Rubidium vapour confined in the core of Kagome HC-PCF utilizing only a single circularly polarized beam. The height and full width at half maximum (FWHM) of the different saturable absorption transparency features are investigated as a function of pump power in the transmitted signals. Additionally the FWHM and the frequency shift of the line centre of each saturable absorption transparency feature are investigated as a function of applied magnetic field. The impact of the single beam polarisation on the saturable absorption transparencies is quantified. The theoretical explanation behind the generation of such transparency lines is under development and lies beyond the scope of the present chapter.

8.1 Introduction

Narrow sub Doppler transparency features based upon saturable absorption spectroscopy (SAS) (1), electromagnetically induced transparency (EIT), coherent population trapping (CPT) (2,3) and nonlinear magneto optical rotation (4) have been well understood and have been implemented in a range of applications. Such applications span from laser metrology to the investigation of the individual physical phenomena. Confined dielectric geometries (5,6) especially HC-PCF have been investigated extensively for laser metrology applications because of their compactness, inherent ruggedness and easy integration in all fibre systems . SAS has

been investigated extensively for acetylene based fibre frequency standards (7–9). Acetylene filled photonic microcells (PMC) are inherently easier to use than multipass power build up cavities (10) because there are no alignment challenges and give reasonable short term stability (8). However experimental techniques such as frequency shifting the pump and probe beams to avoid interference and amplitude modulating the pump beam to avoid noise distortions are necessary to achieve this stability in HC-PCF (7). Atomic vapours such as Cs and Rb with simple hydrogen like energy level structures are widely exploited for frequency standards based upon Ramsey fringes (11) or CPT. EIT has been demonstrated in Rb vapour confined in HC-PCF (12,13), however this requires careful preparation of the atomic coherence and the ultimate achievable linewidth is limited by the dephasing (i.e. atom wall collisions and transit time). In addition both EIT and SAS require pump and probe beams to either generate an atomic coherence or saturate the atomic population. Recently two photon transitions have been demonstrated in Rb vapour in both PBG (14,15) and Kagome HC-PCF (16). In a Rb vapour loaded Kagome HC-PCF a fractional frequency stability of 9.8×10^{-12} at 1 s integration time has been demonstrated (16).

In this chapter experimental results are presented demonstrating saturable absorption features generated using a single circularly polarised beam coupled through Rb vapour loaded hypocycloid core shape Kagome HC-PCF. This contrasts strongly with typical configuration for observing saturated absorption spectroscopy whereby counter propagating pump and probe lasers are utilized (8,17,18). In the configuration reported here the source of the counter propagating wave (i.e. reflected wave) which acts to saturate a particular velocity class of the atomic ensemble is novel and as of yet not fully understood. The generated saturable absorption features are experimentally investigated as a function of the beam power, the applied magnetic field and single beam polarisation. In order to characterise the physical mechanism behind the counter propagating beam giving rise to these saturable absorption features, reflection and transmission spectra are measured. In the final section the experimental results are summarized and potential applications of these features are discussed.

8.2 Fibre Preparation and Coating Procedure

HC-PCF's are prepared in the same manner as in chapter 5 to ensure reduced out-gassing in the UHV chamber and uniform PDMS coating deposition on the inner core wall. The Kagome HC-PCF's are inserted in the UHV chamber and natural Rb vapour is released for a period of 4 weeks to load the HC-PCF's. At the end of the vapour loading period the atomic density is $3.0 \pm 0.5 \times 10^{9}$ cm^{-3} in the PDMS coated Kagome HC-PCF. A strong circularly polarised beam up to 3.0 nW is coupled through the Rb vapour loaded Kagome HC-PCF's to generate saturable absorption transparencies. Beam polarisation and power are controlled independently using a quarter waveplate and neutral density filters. A magnetic field (< 3.5 mT) can be applied in the direction of light propagation using a solenoid coil wound round the UHV chamber.

Two different configurations of the same experimental setup are utilised to characterise the saturable absorption transparency features. The first configuration is a transmission measurement setup shown in the top panel of Fig (8-1). Here an external cavity diode laser (ECDL) operating at 780.24 nm has its polarisation set to circular using a quarter wave plate.

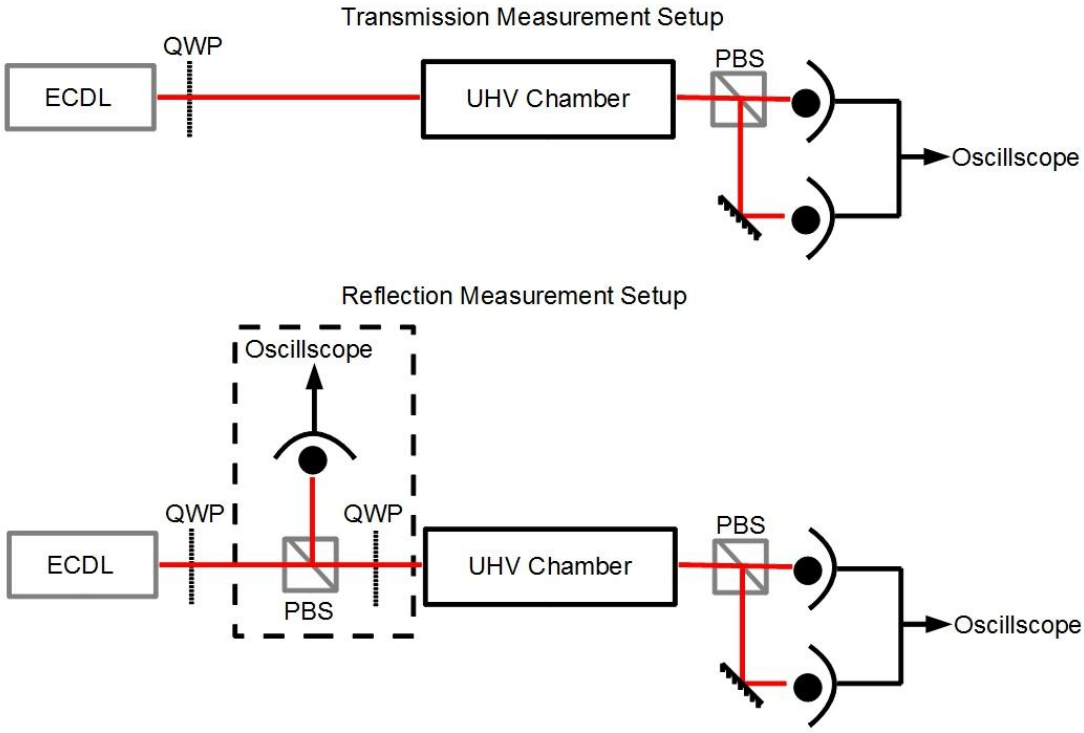

Figure (8-1) Saturable absorption experimental detection in transmission and reflection configurations.

The beam is coupled through the Rb vapour loaded Kagome HC-PCF inside the UHV chamber and the transmitted light is collimated and directed to a polarizing beam splitter cube and the different polarization states are recorded using photodiodes. Transmission measurements of sub-Doppler transparencies were characterised with pump power, applied magnetic field and polarization state. The second experimental configuration is a reflection measurement (lower panel of Fig (8-1)) setup developed after the transmission spectra have been obtained to record the reflected signal from the Rb vapour loaded Kagome HC-PCF's. The setup is identical to the transmission measurement but with the additional optical components shown in the dashed rectangle added to characterise the back reflection signal. Given the novel single beam configuration utilised to generate these features, the back reflection signal provides insight of the physical mechanism behind the generation of the saturable absorption transparencies.

8.3 Saturable absorption transparency features in Rb vapour loaded in coated HC-PCF

Saturable absorption transparency features are observed in Rb vapour confined in Kagome HC-PCF as seen in Fig (8-2) a) within the Doppler broadened ^{85}Rb $5S_{1/2}F=3\rightarrow5P_{3/2}F'=2,3,4$ absorption line. In Fig (8-2) b) the saturable absorption transparency features are shown in detail with the Doppler broadened absorption background subtracted. Comparison with existing work in Rb vapour cells (19) demonstrates remarkable agreement of the spectral location of the saturable absorption features with the ^{85}Rb cross over transition $F=2\rightarrow F=4$ and $F=3\rightarrow F=4$ respectively. However , the occurrence of such features are unusual as only a single circularly polarised beam from a frequency scanned ECDL is used to generate them, which contrasts with those generated via EIT, CPT or SAS, and in which pump and probe laser beam configuration is required. In this configuration the novel question is, by what mechanism does the reflected beam (i.e. counter propagating beam) arise? The saturable absorption transparency features are investigated as a function of laser power, applied magnetic field and input polarisation.

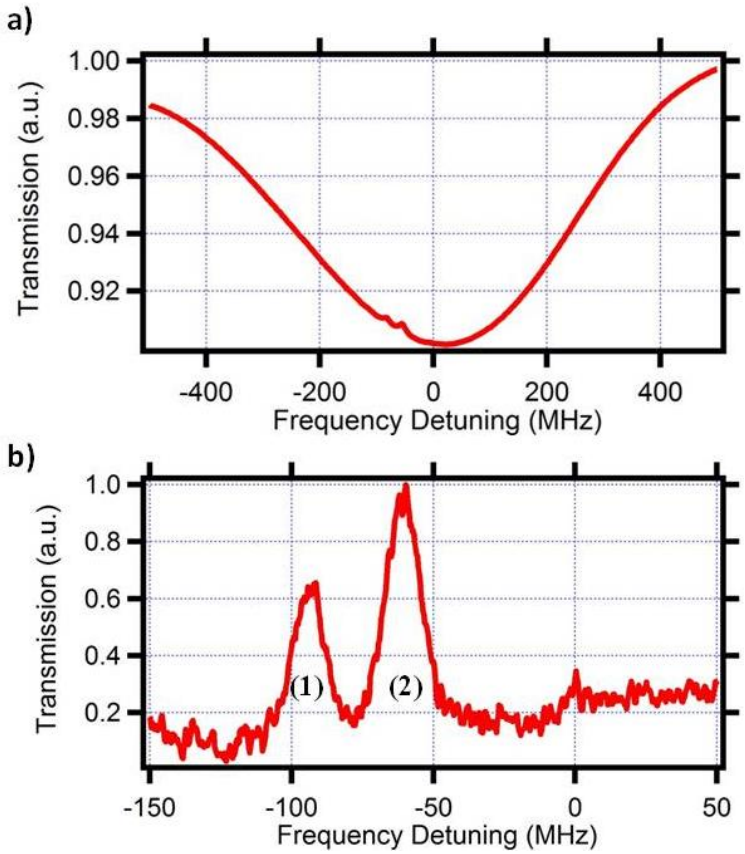

Figure (8-2) a) Saturable absorption transparency features in Doppler broadened absorption line, b) Focus on saturable absorption transparency features with Doppler background subtracted (19)**. The weak feature will be referred to as peak (1) and the strong feature as peak (2).**

In Fig (8-3) a) the evolution of the saturable absorption transparencies FWHM as a function of the single beam power can be observed. Typical power broadening behaviour can be observed for increasing coupled power into the HC-PCF with both features (Fig (8-3) b) exhibiting similar behaviour (20,21). This power broadening behaviour is typically observed in EIT and SAS features as seen in chapter 7.

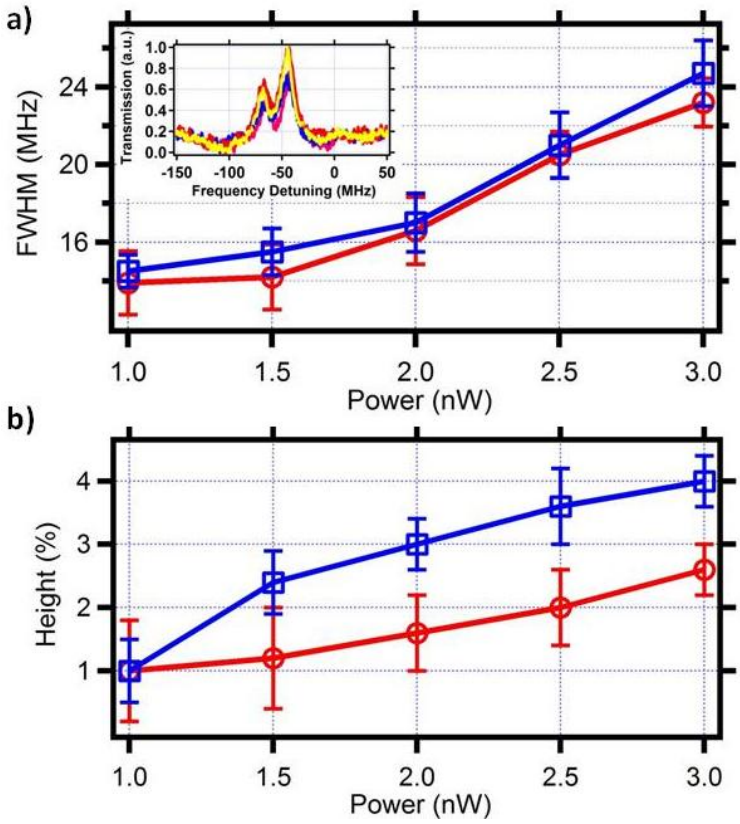

Figure (8-3) a) FWHM evolution of saturable absorption transparency features (blue squares is strong saturable absorption feature, red circles is the weak saturable absorption feature) Inset: Saturable absorption Transparency Features, b) Evolution of Height of saturable absorption transparency features (blue squares is the strong saturable absorption feature, red circles is the weak saturable absorption feature).

Additionally in Fig (8-3) b) the evolution of the transparency height as a percentage of the total Doppler broadened absorption line contrast is plotted as a function of coupled power. The saturable absorption transparency height increases as a function of the coupled power, this behaviour is qualitatively similar to that of EIT features (20,21).

The behaviour of the saturable absorption transparencies is investigated as a function of the applied magnetic field. Fig (8-4) a) presents the evolution of the saturable absorption transparency features FWHM as a function of applied magnetic field, and clearly shows the strong line broadening as the applied magnetic field increases.

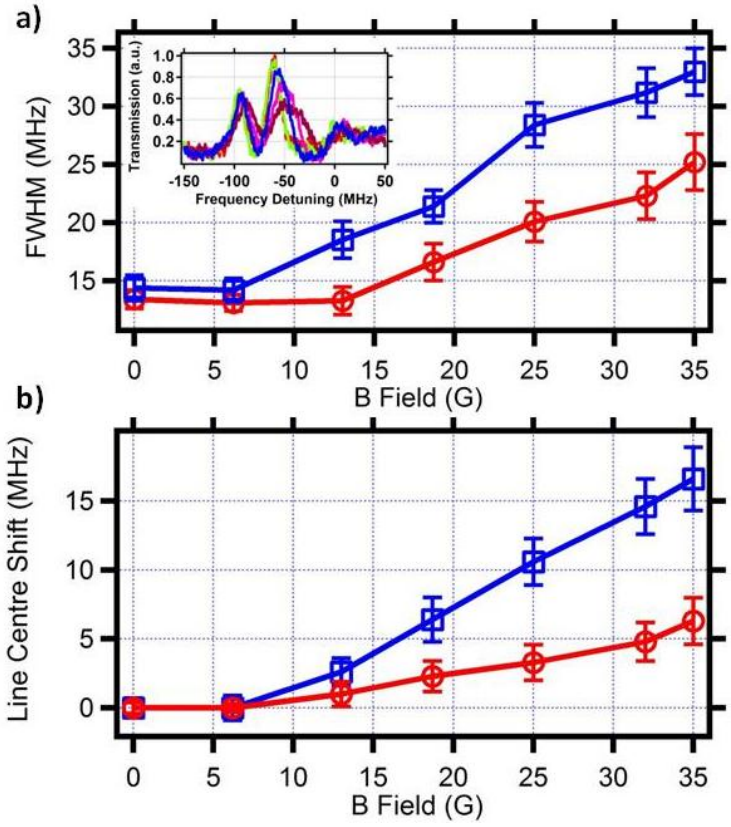

Figure (8-4) a) FWHM evolution of saturable absorption transparency features with applied magnetic field (blue squares – peak 2, red circles – peak 1) Inset: Saturable absorption Transparency Features, b) Frequency shift of line centre evolution of saturable absorption transparency features with applied magnetic field blue squares – peak 2, red circles – peak 1).

In addition to the spectral broadening of the saturable absorption transparencies with magnetic field there is a shift of the transparency line centre frequency (Fig (8-4) b). Both the saturable absorption transparencies experience a shift of the line centre as the magnetic field is increased above 10 G. The difference in the frequency shift of the different saturable absorption transparencies is attributed to the different number of Zeeman sublevels (2F+1) which compose each hyperfine manifold of the excited $5P_{3/2}$ state.

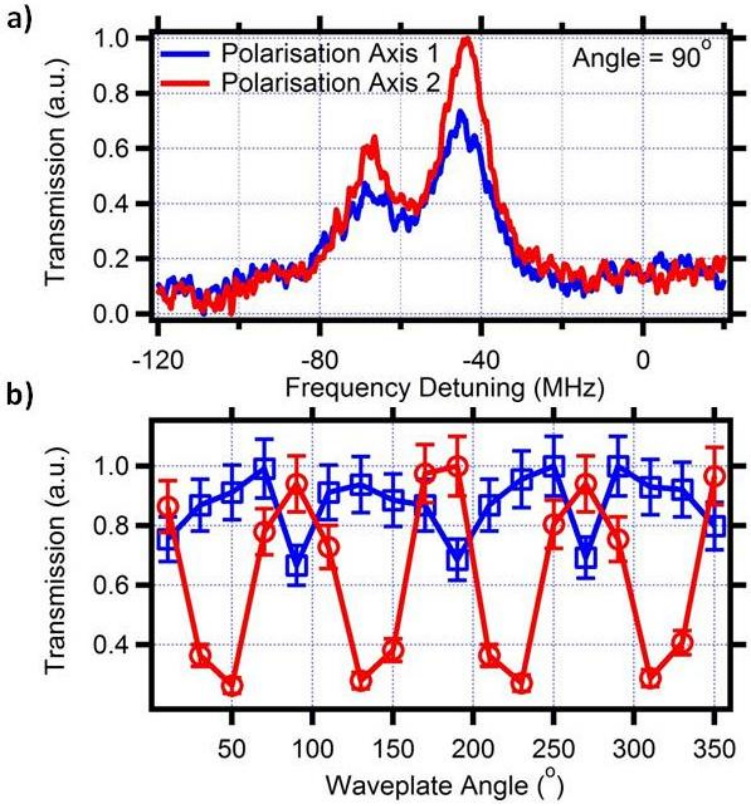

Figure (8-5) a) Saturable absorption features measured on the two different output ports (red - transmission port, blue - reflection port) of a polarising beam splitter (PBS) cube when the input quarter waveplate (QWP) is set at an angle of 90°. b) Evolution of on resonance transmission peak 2 amplitude of the two output ports of PBS with input QWP angle (blue – reflection port of PBS, red - transmission port of PBS).

The impact of the initial light polarisation state on the amplitude of the saturable absorption features is investigated. This is done by directing the output light from the Rb vapour loaded HC-PCF to a polarising beam splitter (PBS) and measuring the amplitude of the saturable absorption transparency features on each arm of the PBS as the angle of the quarter waveplate (QWP) at the input is varied. An example of the saturable absorption transparency features observed on each polarisation axis are shown in Fig (8-5) a) at a single angle of the QWP. The evolution of the peak 2 amplitude with QWP angle readily shows an oscillation with a period of $\pi/2$ rotation of the QWP, there is a coupling between the different polarisation axes (Fig (8-5) b). This behaviour is indicative that the polarisation ellipticity has an impact on the peak amplitude of the saturable absorption features.

In addition to the transmission measurements through the Rb vapour loaded HC-PCF, back reflection measurements are acquired. Here the back reflection measurements (Fig (8-6) a)) are taken in an Rb vapour loaded HC-PCF and an Rb vapour loaded capillary with inner diameter of 950 µm. In addition the reflected

signal of a silica rod was recorded to act as a reference. The silica rod has the same length as the HC-PCF and the capillary but light coupled into the rod only interacts with Rb vapour in the 2 mm space at either end of the UHV chamber. In the reflection measurements presented in Fig (8-6) a) and b) the 4 % Fresnel power reflection from the silica window at the input has been subtracted.

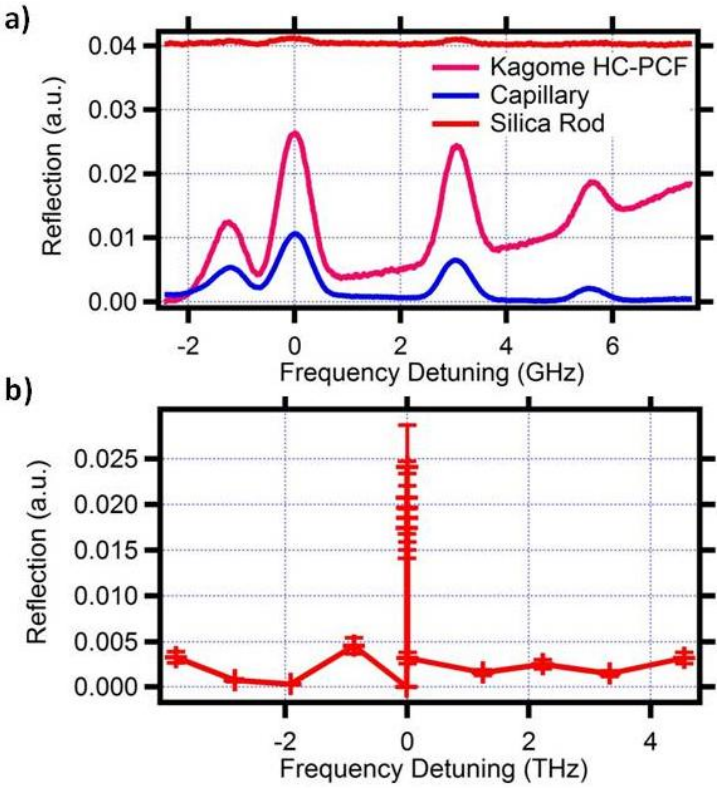

Figure (8-6) a) Back reflected spectrum at different laser detuning for Rb Vapour loaded HC-PCF (pink), silica capillary (blue) and silica rod (red), b) Reflection spectrum from Rb Vapour loaded HC-PCF (red) over large frequency detuning from resonance.

The reflection from the silica rod presents a uniform 4 % of the input power over detuning range from the Rb D2 resonances. Small variations on resonance can be observed due to the interaction with the Rb vapour in the 2 mm space at either end of the rod. In the Rb loaded HC-PCF and capillary resonant reflection can be observed, whereby enhanced reflection signal is observed as the laser is tuned across the Rb absorption lines (22–27). The reflection signal is stronger in the HC-PCF. Additionally several data points were taken at very large laser detuning from resonance (> 1 THz) either side of the D2 resonances (Fig (8-6) b). These points showed only 4% reflection which is primarily attributed to reflection from the silica windows at the input to the UHV chamber. The uniformity of the reflected signal at far detuning from the Rb D2 absorption lines indicates that the reflected signal is highly dependent upon the Rb vapour. The increased reflection above this 4 %

background (Fig (8-6) a) combined with its extremely resonant response is indicative that this reflection is due to the presence of the Rb vapour. Strong back reflections are necessary to generate saturable absorption features by saturating a particular velocity class of the atomic population and as such creating a transparency in the absorption line which can be detected at the output as seen in Fig (8-1) a) & b).

The back reflection signal strength is investigated on resonance with the ^{85}Rb $5S_{1/2}F=3\rightarrow5P_{3/2}$ F'=2, 3, 4 transition as a function of coupled input power (Fig (8-7) a). A linear increase in reflection signal is observed with increasing coupled power.

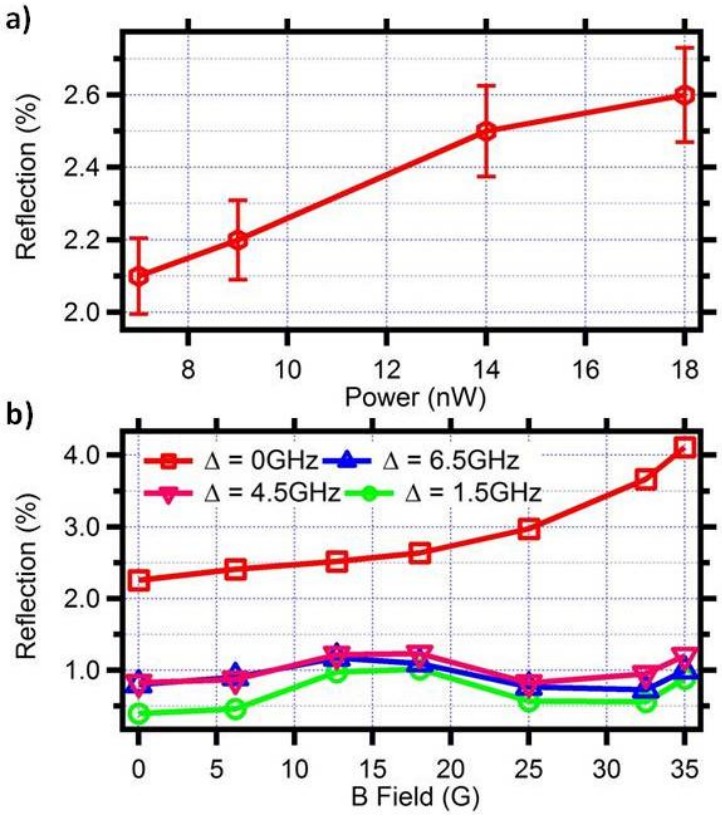

Figure (8-7) Rb 5S1/2F=3-5P3/2F=2, 3, 4 Reflection signal evolution with power a) and magnetic field b)

Here the coupled powers are larger than the typical 3 nW input power used to record the majority of the data. The modest linear increase in reflection signal with increasing coupled powers suggests that the reflection signal is not due to a χ_3 nonlinear process as in (28). The reflection signal is investigated as a function of applied magnetic field (Fig (8-7) b). The reflection signal on resonance (Δ = 0 GHz) with the ^{85}Rb $5S_{1/2}F=3\rightarrow5P_{3/2}$ F'=2,3,4 (red squares) increases from ~ 2.2 % to ~ 4% contrast as the applied magnetic field increases from the geomagnetic field to ~35 G.

The reflection signal is characterised at three off resonance laser detuning (Δ = 1.5 GHz-green circles, 4.5GHz-inverted pink triangles & 6.5GHz-blue triangles) as a function of applied magnetic field. The off resonant reflection signal demonstrates oscillatory behaviour with applied field.

8.4 In progress theoretical model

The experiment has generated novel results demonstrating saturable absorption transparency features in Rb vapour confined in hypocycloid core shape Kagome HC-PCF and resonant reflection spectra. The configuration used to observe such effects contrasts strongly with the configurations used to generate sub-Doppler spectral lines, and consequently, it indicates a new physical mechanism behind these reflections. In order to elucidate this mechanism, two theoretical models are under investigation (at time of writing). The first one relies on the possibility of a non-uniform distribution of Rb vapour along the propagation axis of the HC-PCF. The atomic vapour distribution along the HC-PCF is most likely to be parabolic because of the molecular free flow loading from the open fibre ends. The parabolic atomic vapour density distribution will have an associated variation in refractive index along the fibre length. Such a variation in index gives rise to a sufficiently strong reflection signal. This in turn creates an SAS type pump probe laser beam configuration.

The second theoretical model which is being worked on, as a possible explanation of the experimentally observed reflection signals is one based upon a Faraday rotation induced Bragg grating in the Rb vapour confined in the Kagome HC-PCF. In Kagome HC-PCF the birefringence beat length is on the order of several meters, which was estimated from theoretical modelling. This model has some experimental support based upon the oscillatory behaviour of the reflection signals (Fig (8-7)) with applied magnetic field is indicative of a beat length (l_{BL}) within the Rb vapour loaded Kagome HC-PCF given by (29),

$$l_{BL}^{F} = \frac{2\pi\hbar\Delta l_0}{g\mu_B B}, \tag{8-1}$$

where g is the landé factor , ħ is the reduced Planck's constant, μ_B is the Bohr magnetron, B is the applied magnetic field, l_0 is the absorption length and Δ is the frequency detuning from resonance. Using the experimental parameters in Eq (8-1) a beat length of ~ 1.3 ± 0.2 mm is calculated, this is approximately 1/8th of the total fibre length. This beat length can be assigned to a change in the refractive index,

$$\Delta n = \frac{2\lambda}{l_{BL}^{F}}. \tag{8-2}$$

Where λ is the wavelength and Δn is the difference in left and right hand refractive indices. From Eq (8-2) using the calculated beat length of 1.3 mm from the experimental data it is possible to calculate the difference in refractive indices, a value of $1.2 \pm 0.2 \times 10^{-3}$ is found. It is speculated that there is a periodic modulation of the refractive index at the beat length along the entire length of the Rb vapour loaded Kagome HC-PCF. This periodic modulation behaves as a Bragg grating reflecting a portion of the on resonant input field, hence generating the reflected signal which acts to saturate the atomic population generating the observed transparency features in the transmission spectrum (30). At the time of writing this thesis the complimentary theoretical work is still being developed to explain the observed experimental results. As such this section is a brief overview of the ideas which is being explored to give the best understanding of the observed experimental phenomena presented in section 8.3.

8.5 Summary

For the first time saturable absorption transparencies are generated from a single circularly polarised beam coupled through an Rb vapour loaded hypocycloid core shape Kagome HC-PCF. This configuration is contrary to the traditional pump probe technique, here a counter propagating beam is generated by a novel mechanism which acts to saturate a particular velocity class of the Rb vapour. The behaviour of the saturable absorption transparencies is investigated as a function of the applied magnetic field, laser beam power and polarisation independently. Power broadening behaviour similar to that observed in EIT and SAS features is observed whereby at low powers the FWHM of the features plateaus towards a minimum value of ~14 ± 1

MHz while at high powers significant broadening of the features is observed. As the external magnetic field is varied from the geomagnetic field to 35 G the FWHM of the saturable absorption transparencies increases from ~ 14 ± 1 MHz to ~ 32 ± 2 MHz as the Zeeman sublevel degeneracy is lifted. Additionally the line centre of the transparency features shifts by a maximum of ~16 ± 2 MHz as the applied magnetic field is increased to 35 G above the geomagnetic field in the laboratory. The input polarisation is altered and coupling between the two different polarisation axes is observed every $\pi/2$ rotation of the QWP.

Following on from the characterisation of the saturable absorption features in transmission spectrum, reflection spectra are obtained to investigate the physical mechanism behind the generation of the counter propagating beam. Initially reflection spectrums are obtained from an Rb vapour loaded Kagome HC-PCF, an Rb vapour loaded capillary and a silica rod to act as a reference. In the silica rod a uniform 4% Fresnel reflection is observed at all laser detuning from resonance, small variations are observed on resonance with the Rb D2 absorption line because of the 2 mm space at either end of the silica rod in the UHV chamber. In the Rb vapour loaded capillary and Kagome HC-PCF resonant reflection is observed with contrast of 1 % and 2.5 % respectively. The strong resonant reflection behaviour indicates that the signal is dependent upon the presence of the Rb vapour. Far off resonance (Δ = 4 THz) reflection demonstrates a uniform 4% Fresnel reflection from the input window. This reinforces that the on resonance enhancement of the reflection above 4% is primarily due to the presence of Rb vapour. Additionally the reflection dependence upon input power is studied on resonance with the ^{85}Rb $5S_{1/2}F=3\rightarrow5P_{3/2}F'=2, 3, 4$. A moderate linear increase is observed with increasing coupled power which decreases the possibility of the effect being a nonlinear χ_3 process. Two in progress theoretical models are proposed which could give rise to the observed experimental results. The first models proposes that the non-uniform distribution of Rb vapour along the fibre core gives rises to a step-wise refractive index profile along the HC-PCF giving rise to an enhanced reflection signal. The second possible explanation is based upon the formation of a Bragg grating in the Rb vapour due to the Faraday rotation effect of the Rb vapour of the left and right hand circularly polarised components. Off resonant oscillations of the reflection spectrum with applied magnetic field suggests the formation of a Bragg grating based upon

periodic modulations of the refractive index at the calculated beat length gives the possibility for enhanced reflection. The enhanced resonant reflection could saturate the atomic population and generates transparency features in the transmitted spectrum.

Future work could focus on observing these saturable absorption transparencies in larger diameter core HC-PCF's so as to observe narrower features because the transit time broadening will be reduced. Different antirelaxation coatings such as OTS, ODMS and alkene based coated could be applied to inner wall of the hollow core before observing the saturable absorption transparency features. The features could be used to frequency stabilise an ECDL through frequency modulation stabilisation for applications such as magneto optical traps or optical metrology. Such a system has advantages over those utilising EIT or saturable absorption features because of the simplicity of the set up required. Future work could focus on using higher magnetic fields to split the Zeeman sublevels further and utilising frequency stabilised lasers to interrogate single Zeeman sublevels. Additionally applying magnetic fields perpendicular to the axis of light propagation could reveal fundamental properties of the saturable absorption transparency features.

References

1. Labachelerie M De, Nakagawa K, Ohtsu M. Ultranarrow 13 C2H2 saturated-absorption lines at 1.5um. Optics Letters. 1994;19(11):840–2.

2. Vanier J, Godone A, Levi F. Coherent population trapping in cesium: Dark lines and coherent microwave emission. Physical Review A [Internet]. 1998 Sep;58(3):2345–58. Available from: http://link.aps.org/doi/10.1103/PhysRevA.58.2345

3. Vanier J. Atomic clocks based on coherent population trapping: a review. Applied Physics B [Internet]. 2005 Jul 22 [cited 2013 Feb 13];81(4):421–42. Available from: http://www.springerlink.com/index/10.1007/s00340-005-1905-3

4. Budker D, Yashchuk V, Zolotorev M. Nonlinear Magneto-optic Effects with Ultranarrow Widths. Physical Review Letters [Internet]. 1998 Dec;81(26):5788–91. Available from: http://link.aps.org/doi/10.1103/PhysRevLett.81.5788

5. Knappe S, Shah V, Schwindt PDD, Hollberg L, Kitching J, Liew L-A, et al. A microfabricated atomic clock. Applied Physics Letters [Internet]. 2004 [cited 2013

Feb 13];85(9):1460. Available from: http://link.aip.org/link/APPLAB/v85/i9/p1460/s1&Agg=doi

6. Yang W, Conkey DB, Wu B, Yin D, Hawkins AR, Schmidt H. Atomic spectroscopy on a chip. Nature Photonics [Internet]. 2007 Jun [cited 2013 Feb 13];1(6):331–5. Available from: http://www.nature.com/doifinder/10.1038/nphoton.2007.74

7. Wang C, Wheeler N V, Fourcade-dutin C, Grogan M, Bradley TD, Washburn BR, et al. Acetylene frequency references in gas-filled hollow optical fiber and photonic microcells. Applied optics. 2013;52(22):5430–9.

8. Knabe K, Wu S, Lim J, Tillman K a, Light PS, Couny F, et al. 10 kHz accuracy of an optical frequency reference based on (12)C2H2-filled large-core kagome photonic crystal fibers. Optics express [Internet]. 2009 Aug 31;17(18):16017–26. Available from: http://www.ncbi.nlm.nih.gov/pubmed/19724600

9. Wang C, Wheeler N V, Lim J, Knabe K, Grogan M, Wang Y, et al. Portable acetylene frequency references inside sealed hollow-core kagome photonic crystal fiber. CLEO 2011 [Internet]. IEEE Computer Society; 2011. p. 23–4. Available from: http://opus.bath.ac.uk/25865/

10. Czajkowski a, Madej a. ., Dubé P. Development and study of a 1.5 μm optical frequency standard referenced to the P(16) saturated absorption line in the (ν1+ν3) overtone band of 13C2H2. Optics Communications [Internet]. 2004 Apr [cited 2013 Jul 25];234(1-6):259–68. Available from: http://linkinghub.elsevier.com/retrieve/pii/S0030401804000483

11. Zanon-willette T. Ultrahigh-resolution spectroscopy with atomic or molecular dark resonances : Exact steady-state line shapes and asymptotic profiles in the adiabatic pulsed regime. Physical Review A. 2011;062502:1–17.

12. Ghosh S, Bhagwat A, Renshaw C, Goh S, Gaeta A, Kirby B. Low-Light-Level Optical Interactions with Rubidium Vapor in a Photonic Band-Gap Fiber. Physical Review Letters [Internet]. 2006 Jul [cited 2013 Feb 13];97(2):023603. Available from: http://link.aps.org/doi/10.1103/PhysRevLett.97.023603

13. Light PS, Benabid F, Couny F, Maric M, Luiten a N. Electromagnetically induced transparency in Rb-filled coated hollow-core photonic crystal fiber. Optics letters [Internet]. 2007 May 15;32(10):1323–5. Available from: http://www.ncbi.nlm.nih.gov/pubmed/17440575

14. Saha K, Venkataraman V, Londero P, Gaeta A. Enhanced two-photon absorption in a hollow-core photonic-band-gap fiber. Physical Review A [Internet]. 2011 Mar [cited 2012 Apr 6];83(3):1–5. Available from: http://link.aps.org/doi/10.1103/PhysRevA.83.033833

15. Venkataraman V, Londero P, Bhagwat AR, Slepkov AD, Gaeta AL. All-optical modulation of four-wave mixing in an Rb-filled photonic bandgap fiber.

Optics letters [Internet]. 2010 Jul 1;35(13):2287–9. Available from: http://www.ncbi.nlm.nih.gov/pubmed/20596222

16. Perrella C, Light PS, Anstie JD, Baynes FN, Benabid F, Luiten a. N. Two-color rubidium fiber frequency standard. Optics Letters [Internet]. 2013 Jun 11;38(12):2122. Available from: http://www.opticsinfobase.org/abstract.cfm?URI=ol-38-12-2122

17. Henningsen J, Hald J, Peterson JC. Saturated absorption in acetylene and hydrogen cyanide in hollow-core photonic bandgap fibers. Optics express [Internet]. 2005 Dec 26;13(26):10475–82. Available from: http://www.ncbi.nlm.nih.gov/pubmed/19503263

18. Hald J, Petersen J, Henningsen J. Saturated Optical Absorption by Slow Molecules in Hollow-Core Photonic Band-Gap Fibers. Physical Review Letters [Internet]. 2007 May [cited 2013 Jun 9];98(21):213902. Available from: http://link.aps.org/doi/10.1103/PhysRevLett.98.213902

19. Školnik G, Vujičić N, Ban T. Optical pumping of the Zeeman components in the rubidium vapor. Optics Communications [Internet]. 2009 Apr [cited 2013 Mar 22];282(7):1326–34. Available from: http://linkinghub.elsevier.com/retrieve/pii/S0030401808012431

20. Vanier J, Levine M, Janssen D, Delaney M. Contrast and linewidth of the coherent population trapping transmission hyperfine resonance line in ^{87}Rb: Effect of optical pumping. Physical Review A [Internet]. 2003 Jun [cited 2013 Feb 13];67(6):065801. Available from: http://link.aps.org/doi/10.1103/PhysRevA.67.065801

21. Akulshin AM, Sautenkov VA, Velichansky VL, Zibrov AS. POWER BROADENING OF SATURATION A B S O R P T I O N R E S O N A N C E ON THE D2 LINE OF RUBIDIUM. Optics Communications. 1990;77(4):30–3.

22. Ducloy M. Nonlinear selective reflection from an atomic vapor at arbitary incidence abgle. Physical Review A. 1988;38(10):5197–205.

23. Schuller F, Nienhuis G, Ducloy M. Selective relfection from an atomic vapor in a pump probe scheme. Physical Review A. 1991;43(1).

24. Simoneau P, Le Boiteaux S, De Araujo CB, Bloch D, Rios Leite JR, Ducloy M. Doppler-free evanescent wave spectroscopy. Optics Communications. 1986;59(2):103–6.

25. Vuletic V, Sautenkov VA, Zimmermann C, Hansch TW. Optical pumping saturation effect in selective reflection. Optics Communications. 1994;108(May):77–83.

26. Wang P, Gallagher a., Cooper J. Selective reflection by Rb. Physical Review A [Internet]. 1997 Aug;56(2):1598–606. Available from: http://link.aps.org/doi/10.1103/PhysRevA.56.1598

27. Akulshin AM, Celikov AA, Sautenkov VA, Vartanian TA, Velichansky VL. Intensity and concentration in selective reflection dependence of Doppler-free resonance. Optics Communications. 1991;85:21–5.

28. Yavuz D. Refractive Index Enhancement in a Far-Off Resonant Atomic System. Physical Review Letters [Internet]. 2005 Nov [cited 2013 Jul 8];95(22):223601. Available from: http://link.aps.org/doi/10.1103/PhysRevLett.95.223601

29. Budker D, Fizyki I, Smoluchowskiego M, Jagiellon U, Weis A. Resonant nonlinear magneto-optical effects in atoms *. Reviews of Modern Physics. 2002;74(October).

30. Little B, Starling DJ, Howell JC, Cohen RD, Shwa D, Katz N. Rapidly reconfigurable optically induced photonic crystals in hot rubidium vapor. Physical Review A [Internet]. 2013 Apr [cited 2013 Jun 26];87(4):043815. Available from: http://link.aps.org/doi/10.1103/PhysRevA.87.043815

Chapter 9

Future Work

9.1 Future Work

The work of the present thesis is part of an overarching aim which consists of the development of a photonic platform based on HC-PCF for atom optics related applications. Whilst the results reported in this thesis represent necessary and important milestones towards achieving this aim, further future work is still required to fully capitalise on the salient feature of HC-PCF.

In chapter 3 and 4 the development of low loss PBG guiding and inhibited coupling (IC) Kagome HC-PCF's are reported. The fabrication of IC Kagome HC-PCF's is ongoing with the drive to fabricate extremely low loss (< 10 dB/km) fibre. Ongoing fibre fabrication is aimed at optimising the hypocycloidal core curvature to develop low loss IC Kagome fibre and to understand the IC guidance mechanism. Investigation is ongoing into the role of the photonic crystal cladding in the IC guidance mechanism. To do this several IC Kagome HC-PCF's are being fabricated with different numbers of cladding rings to observe the influence on the optical attenuation. Such a work would enhance our understanding of this type of fibre, and hence allows a better assessment of its potential performance in atom optics.

The development of alkene coatings by Budker and co-workers with 60 s long transverse spin relaxation times has potential application to compact alkali metal vapour packages because up to 1 million wall collisions are possible before dephasing. Such a coating when applied to a long length of HC-PCF could offer increased precision and sensitivity.

Additional coating developments are possible such as developing aluminosilicate sol-gel coatings for maintaining Rb vapour within the hollow core of a HC-PCF. These developments could include altering the constituents of the wet sol-gel or altering the ratios of aluminium to silica in the sol-gels. Multilayer coatings consisting of both aluminosilicate sol-gels and antirelaxation coatings such as PDMS could be developed to gain advantages of both coating materials properties. Development of aluminosilicate sol-gels has potential application in fabricating Rb vapour loaded photonic microcells (PMC) because of the extended Rb vapour lifetime within the hollow core. A further expected development is exploiting the long lifetime of Rb in ceramic coated HC-PCF to assemble the first Rb filled PMC.

Utilising the experimental results from chapter 5 on Kagome HC-PCF tapering and sleeve splicing the fabrication of an Rb vapour loaded photonic microcell (PMC) is within reach when combined with Helium splicing technique developed for low pressure acetylene PMC's. Optimisation of the tapering and sleeve splicing techniques for the particular fibre would be required but considering the proof of principle has been demonstrated this should not be difficult. If these techniques were combined with antirelaxation coated Kagome HC-PCF's or even possibly multilayer coating combining the advantages of sol-gel and PDMS, the fabrication of a PMC with highly desirable properties is now a real possibility.

Saturable absorption transparencies are investigated in Rb vapour loaded in HC-PCF's for the first time using a single circularly polarised beam. These saturable absorption features have potential application in frequency stabilisation of ECDL. When these saturable absorption features are exploited in an Rb vapour PMC format this system could be utilised as a compact frequency stabilisation system.